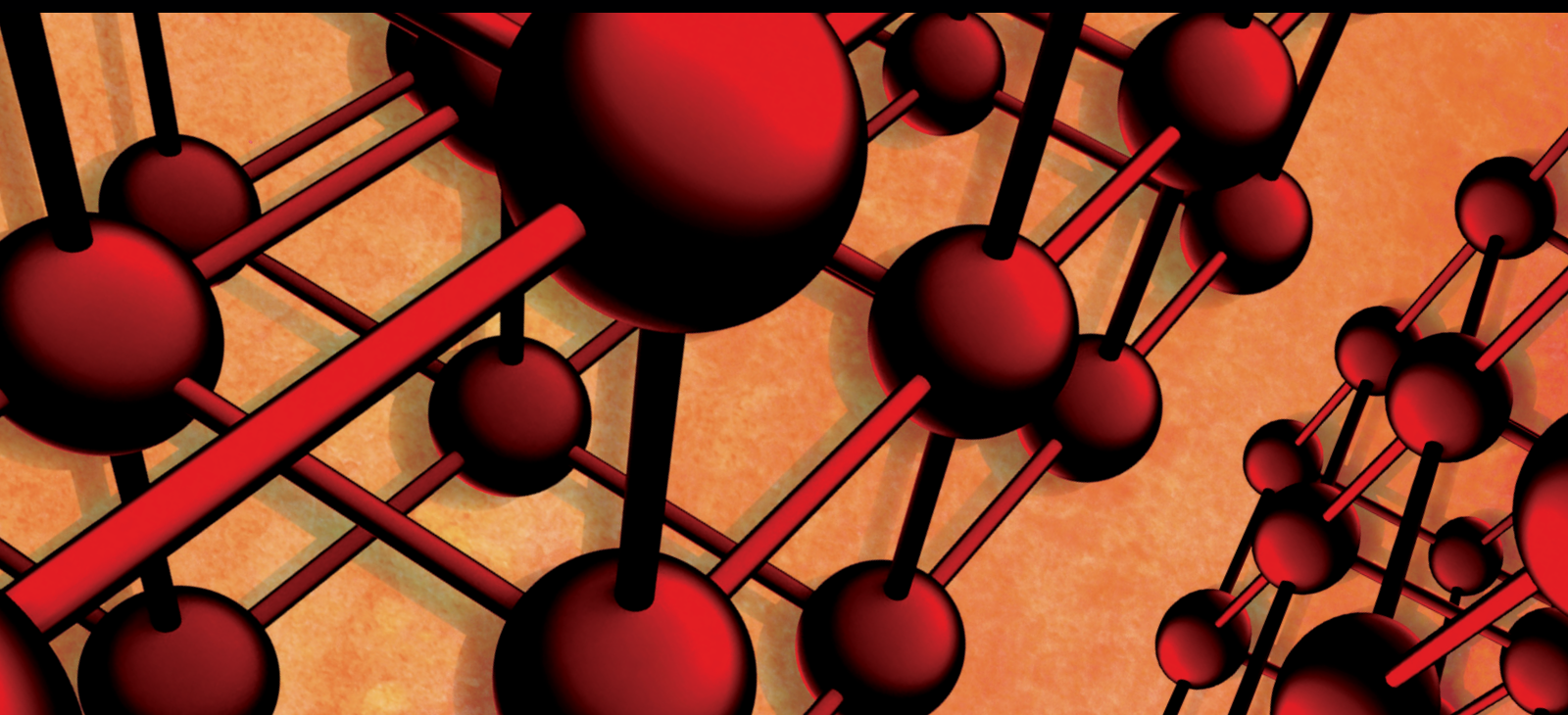


Nanostructured Materials: Formation, Characterization, and Properties—Latest Advances in 1D, 2D, and 3D Nanostructures

Guest Editors: Luís Cunha, Denis Chaumont, and Aldo Craievich





**Nanostructured Materials: Formation,
Characterization, and Properties—Latest
Advances in 1D, 2D, and 3D Nanostructures**

Advances in Materials Science and Engineering

**Nanostructured Materials: Formation,
Characterization, and Properties—Latest
Advances in 1D, 2D, and 3D Nanostructures**

Guest Editors: Luís Cunha, Denis Chaumont, and Aldo Craievich



Copyright © 2014 Hindawi Publishing Corporation. All rights reserved.

This is a special issue published in “Advances in Materials Science and Engineering.” All articles are open access articles distributed under the Creative Commons Attribution License, which permits unrestricted use, distribution, and reproduction in any medium, provided the original work is properly cited.

Editorial Board

K. G. Anthymidis, Greece
Robert S. Averbach, USA
Amit Bandyopadhyay, USA
Zoe Barber, UK
Yucel Birol, Turkey
Susmita Bose, USA
Steve Bull, UK
Peter Chang, Canada
Daolun Chen, Canada
Manish U. Chhowalla, USA
S. Chinnappanadar, India
Martin Crimp, USA
Jie Dai, Singapore
Chapal K. Das, India
João P. Davim, Portugal
Seshu B. Desu, USA
Yong Ding, USA
Sergi Gallego, Spain
John W. Gillespie, USA
Hiroki Habazaki, Japan
Richard Hennig, USA
Dachamir Hotza, Brazil
Chun-Hway Hsueh, Taiwan
Shyh-Chin Huang, Taiwan
Rui Huang, USA
Wei Huang, China
Jacques Huot, Canada
William A. Jesser, USA
Jaehwan Kim, Korea

Sridhar Komarneni, USA
Prashant Kumta, USA
Jui-Yang Lai, Taiwan
Pavel Lejcek, Czech Republic
Markku Leskela, Finland
Bin Li, China
Hai Lin, China
Yuanhua Lin, China
Zhimin Liu, China
Tao Liu, China
Jun Liu, China
Ying Liu, USA
Meilin Liu, Georgia
Yuan Liu, China
Gang Liu, China
Maria A. Loi, The Netherlands
Hai Lu, China
Peter Majewski, Australia
Shuichi Miyazaki, Japan
Paul Munroe, Australia
Ali Nazari, Iran
Luigi Nicolais, Italy
Tsutomu Ohzuku, Japan
Xiaoqing Pan, USA
Ganapathiraman Ramanath, USA
Raju V. Ramanujan, Singapore
Manijeh Razeghi, USA
Mohd Sapuan Salit, Malaysia
Jainagesh A. Sekhar, USA

Jiangbo Sha, China
Liyuan Sheng, China
You Song, China
Aloysius Soon, Korea
Charles C. Sorrell, Australia
Steven L. Suib, USA
Sam-Shajing Sun, USA
Weihua Tang, China
Achim Trampert, Germany
Vladimir Tsukruk, USA
Krystyn Van Vliet, USA
Rui Vilar, Portugal
Min Wang, China
Jörg M. K. Wiezorek, USA
Wei Wu, USA
Gongnan Xie, China
Aiguo Xu, China
Jianqiao Ye, UK
Yadong Yin, USA
Ming-Xing Zhang, Australia
Jian Zhang, Singapore
Kai Zhang, China
Kai Zhang, China
Rui Zhang, China
Tao Zhang, China
Bin Zhang, China
Jun Zhang, China
Yufeng Zhang, China
Jing Zhang, China

Contents

Nanostructured Materials: Formation, Characterization, and Properties Latest Advances in 1D, 2D, and 3D Nanostructures, Luís Cunha, Denis Chaumont, and Aldo Craievich
Volume 2014, Article ID 164174, 2 pages

Structural Characterization of Silica Particles Extracted from Grass *Stenotaphrum secundatum*: Biotransformation via Annelids, A. Espíndola-Gonzalez, R. Fuentes-Ramirez, A. L. Martínez-Hernández, V. M. Castaño, and C. Velasco-Santos
Volume 2014, Article ID 956945, 7 pages

Fabrication of SERS Active Surface on Polyimide Sample by Excimer Laser Irradiation, T. Csizmadia, B. Hopp, T. Smausz, Zs. Bengery, J. Kopniczky, I. Hanyecz, and G. Szabó
Volume 2014, Article ID 987286, 6 pages

Nanocrystalline Al Composites from Powder Milled under Ammonia Gas Flow, J. Cintas, E. S. Caballero, J. M. Montes, F. G. Cuevas, and C. Arevalo
Volume 2014, Article ID 617241, 8 pages

Size Controlled Synthesis of FeCo Alloy Nanoparticles and Study of the Particle Size and Distribution Effects on Magnetic Properties, A. Shokuhfar and S. S. S. Afghahi
Volume 2014, Article ID 295390, 10 pages

Synthesis of Dendritic Silver Nanoparticles and Their Applications as SERS Substrates, Jinshan Yu and Xingui Zhou
Volume 2013, Article ID 519294, 4 pages

Influence of Annealing Temperature on the Magnetic Properties of Rapidly Quenched $(\text{Nd,Pr})_2-(\text{Fe,Co,Ga,Ti,C})_{14}\text{B}/\alpha\text{-Fe}$ Nanocomposite Ribbons, Rahim Sabbaghizadeh, Mansor Hashim, Reza Gholamipour, Ghazaleh Bahmanrokh, and Mohd Shamsul Ezzad Shafie
Volume 2013, Article ID 620761, 5 pages

Editorial

Nanostructured Materials: Formation, Characterization, and Properties—Latest Advances in 1D, 2D, and 3D Nanostructures

Luís Cunha,¹ Denis Chaumont,² and Aldo Craievich³

¹ *Centro de Física, Universidade do Minho, Campus de Gualtar, 4710-057 Braga, Portugal*

² *Laboratoire ICB, Université de Bourgogne, 9 avenue Alain Savary, BP 47 870, 21 078 Dijon Cedex, France*

³ *Instituto de Física, Universidade de São Paulo, Rua do Matão Travessa R 187, 05508-900 São Paulo, SP, Brazil*

Correspondence should be addressed to Luís Cunha; lcunha@fisica.uminho.pt

Received 7 April 2014; Accepted 7 April 2014; Published 17 April 2014

Copyright © 2014 Luís Cunha et al. This is an open access article distributed under the Creative Commons Attribution License, which permits unrestricted use, distribution, and reproduction in any medium, provided the original work is properly cited.

“There’s plenty of room at the bottom,” said Richard P. Feynman, during a talk in December 29, 1959. These words are considered the beginning of the nanoera, despite a paper published by Radushkevich and Lukyanovich, in 1952, showing graphitic carbon fibres with 50 nanometers in diameter. In any case the door of the world of nanoscience and nanotechnology was opened. Feynman’s premonitory words became a reality and the nanoworld never stopped evolving. The research done in this field allows developing novel nanostructures, which sooner or later will have an impact on society and will promote the development of entrepreneurial activities for the use of advanced technologies.

The main focus of this special issue aims at contributing to the dissemination of new developments and original ideas related to the production, characterization, and applications of nanostructures to several fields such as nanomedicine, nanoelectronics, manipulation at nanoscale, optics, and photonics. The accepted articles cover different topics, namely, preparation of nanoparticles and nanostructures, surface plasmon resonance (SPR) effect, surface enhanced Raman scattering (SERS), preparation of SERS active surfaces, effect of annealing temperature on the magnetic properties of Nd-Fe-B nanocomposites, and biotransformation.

The article “*Nanocrystalline Al composites from powder milled under ammonia gas flow*” by J. Cintas et al. describes the synthesis of hard and thermally stable Al composites, prepared by powder milling Al in the presence of ammonia flow, followed by the sintering of milled powders. The Al grain growth is constrained to a maximum size of 45 nm.

“*Size controlled synthesis of FeCo alloy nanoparticles and study of the particle size and distribution effects on magnetic*

properties” is the title of the article by A. Shokuhfar and S. S. Afghahi, in which the authors describe the quaternary microemulsion system used to control the production of FeCo alloy nanoparticles and the effect of the processing parameters on their size and size distribution. The influence of the size of the particles on the magnetic properties was also investigated.

Magnetic properties were also the subject of the paper “*Influence of annealing temperature on the magnetic properties of rapidly quenched (Nd,Pr)₂-(Fe,Co,Ga,Ti,C)₁₄B/α-Fe nanocomposite ribbons*,” by R. Sabbaghizadeh et al. This study describes the production of nanocomposite ribbons, with grain size lower than 50 nm, by melt spinning and the optimized postannealing process that leads to the best magnetic properties.

Two articles dealt with the production of substrates for surface enhanced Raman scattering (SERS) analysis: “*Fabrication of SERS active surface on polyimide sample by excimer laser irradiation*” by T. Csizmadia et al. and “*Synthesis of dendritic silver nanoparticles and their applications as SERS substrates*” by J. Yu and X. Zhou.

T. Csizmadia et al. used an excimer laser to irradiate a polyimide foil, before coating it with Ag, by pulsed laser deposition, using different fluences. The study of the activity of the surface for SERS was done by using a rhodamine 6G aqueous solution.

A rhodamine 6G aqueous solution was also used by J. Yu and X. Zhou to study the possibility of using silver nanoparticles, with dendritic morphology, deposited onto a Ag crystal, for SERS. The silver nanoparticles, with sizes ranging from 20 to 30 nm, were prepared by electrodeposition.

Both articles conclude that the substrates exhibit meaningful results concerning their potential to be used for SERS.

A. Espíndola-Gonzalez et al. authored the article entitled “*Structural characterization of silica particles extracted from grass *Stenotaphrum secundatum*: biotransformation via annelids.*” This paper describes the characterization of silica particles extracted by biotransformation from St. Augustine grass. These particles were compared with silica particles extracted directly from the grass and significant differences in size and structure were detected.

In short, this issue contains original contributions to synthesis, characterization, and properties of nanoparticles and nanostructures. We expect that the readers working in the field of nanoscience and nanotechnology will find in the different articles new motivating ideas useful for their ongoing investigations.

*Luis Cunha
Denis Chaumont
Aldo Craievich*

Research Article

Structural Characterization of Silica Particles Extracted from Grass *Stenotaphrum secundatum*: Biotransformation via Annelids

A. Espíndola-Gonzalez,¹ R. Fuentes-Ramirez,¹ A. L. Martínez-Hernández,^{2,3}
V. M. Castaño,^{2,4} and C. Velasco-Santos^{2,3}

¹ Division de Ciencias Naturales y Exactas, Departamento de Ingeniería Química, Universidad de Guanajuato, Campus Noria Alta, Guanajuato, GTO 36050, Mexico

² Centro de Física Aplicada y Tecnología Avanzada, Universidad Nacional Autónoma de México, Boulevard Juriquilla No. 3001, Queretaro, QRO 76230, Mexico

³ Division de Estudios de Posgrado e Investigación, Instituto Tecnológico de Queretaro, Avenida Tecnológico S/N Esq. Gral. Mariano Escobedo, Col. Centro Histórico, Queretaro, QRO 76000, Mexico

⁴ CIATEQ, Av. El Retablo 150, Queretaro, QRO 76150, Mexico

Correspondence should be addressed to C. Velasco-Santos; cylaura@gmail.com

Received 16 October 2013; Revised 22 January 2014; Accepted 12 February 2014; Published 14 April 2014

Academic Editor: Aldo Craievich

Copyright © 2014 A. Espíndola-Gonzalez et al. This is an open access article distributed under the Creative Commons Attribution License, which permits unrestricted use, distribution, and reproduction in any medium, provided the original work is properly cited.

This study shows the structural characterization of silica particles extracted from *Stenotaphrum secundatum* (St. Augustine) grass using an annelid-based biotransformation process. This bioprocess starts when St. Augustine grass is turned into humus by vermicompost, and then goes through calcination and acid treatment to obtain silica particles. To determine the effect of the bioprocess, silica particles without biotransformation were extracted directly from the sample of grass. The characterization of the silica particles was performed using Infrared (FTIR) and Raman spectroscopy, Transmission Electron Microscopy (TEM), X-ray Diffraction (XRD), Dynamic Light Scattering (DLS), and Energy Dispersion Spectroscopy (EDS). Both types of particles showed differences in morphology and size. The particles without biotransformation were essentially amorphous while those obtained via annelids showed specific crystalline phases. The biological relationship between the metabolisms of worms and microorganisms and the organic-mineral matter causes changes to the particles' properties. The results of this study are important because they will allow synthesis of silica in cheaper and more ecofriendly ways.

1. Introduction

Of all plants, the grasses are the most important to man. All our breadstuffs, corn, wheat, oats, rye, barley, and rice, are grasses. The food, agricultural, and forestry industries produce large volumes of waste annually worldwide as by-products of use of these grasses, causing a serious disposal problem; however, they constitute a renewable resource from which many useful materials can be derived. In leaves of grasses, silica can constitute 2–5% dry matter, 10–20 times higher than levels found typically in dicotyledonous plants [1]. Silica is stored primarily as opaline phytoliths in the

epidermis [2]. Although all plants rooting in soil contain some Si in their tissues [3], the content differs greatly between plant species because of differences in Si uptake by the roots. Uptake and translocation occur as monosilicic acid and the deposition form is amorphous silica gel $\text{SiO}_2 \cdot n\text{H}_2\text{O}$ [4]. Accumulation of such high levels of a single mineral element within grasses family suggests that it has a functional significance. Progress in understanding the uptake and accumulation of Si in plants has been led extensively by some authors [5–8]. The opal-like phytoliths (hydrated amorphous silica) occur in the tissue of grasses in a three-dimensional distribution in such a way as to suggest that

silica is being excluded from the cells and deposited as silica gel in the spaces between cells. The silica is transported as $\text{Si}(\text{OH})_4$ and then concentrated and gelled as water evaporates from the leaves. Pores in the gel measure between 1 and 10 nm in diameter and are full of water, making silica completely amorphous [9]. Precipitation and polymerization of the silica, aided by evaporation and water metabolism in the plant's body, lead to the formation of intra- as well as extracellular silica bodies. Intracellularly, silica accumulates in both the cytoplasm and the vacuoles of the plant cells and can be deposited in roots, stem, and leaves. Earlier, our group reported the synthesis of nanoparticles of silica oxide from rice husk, sugar cane bagasse, and coffee husk, by employing vermicompost with annelids (*Eisenia foetida*) [10]. The characterization of these particles can contribute to the understanding of the natural mechanism of transformation from the amorphous form to nanocrystals oxides in intestines of the worms. This bioprocess can be applied in the use of waste grass to produce specific nanocrystals with potential applications in materials science.

St. Augustine grass (*Stenotaphrum secundatum*) is native to the coastal regions of the Gulf of Mexico and the Mediterranean. This specimen is widely used as a turf grass in warm, humid, tropical, and subtropical climates where its broad leaf blades produce a tight canopy from rapidly elongating stolons, resulting in a coarse-textured turf [11]. Adaptive and morphological variations in St. Augustine grass are associated with chromosome differences. The most conspicuous differences among ploidy levels are that diploids are lower growing and have narrower, translucent, bright green leaf blades while polyploids have coarser, thicker leaf blades that are blue/green and less saturated in colour [12]. Although commonly found on siliceous and calcareous sands near the sea, St. Augustine grass also grows on a wide range of well to poorly drained soils, from sandy loams to light clays. Silicon accumulation in dry land Gramineae such as St. Augustine grass has been reported to be between 0.5 and 1.5%, while in dicotyledons (i.e., broadleaf plants) it is less than 0.2%. Indeed, the amounts of silicon that plants accumulate from the soil can be much higher than the amounts of any other essential macro- or micronutrients [13].

Vermicompost is the excreta of earthworms, which are capable of improving soil health and nutrient status. Vermiculture is a process by which all types of biodegradable waste, such as farm wastes, kitchen wastes, market wastes, biowastes of agrobased industries, and livestock wastes, are converted while passing through the worm gut to nutrient rich vermicompost. Vermi worms are used here as biological agents to consume those wastes and to deposit excreta in the process called vermicomposting [14]. Vermicomposting is a simple biotechnological process of composting, in which certain species of earthworms are used to enhance the process of waste conversion and produce a better product. Vermicomposting is a mesophilic process that utilizes microorganisms and earthworms that are active at 10°C to 32°C (not ambient temperature but the temperature within the pile of moist organic material). The process is faster than composting because the material passes through the earthworm gut and a significant but not fully understood transformation

takes place, whereby the resulting earthworm casting (worm manure) is rich in microbial activity. Earthworms have been long recognized by farmers as beneficial to soil [15] and, as one of the major soil macrofauna, constitute an important group of secondary decomposers. Earthworms are key biological agents in the degradation of organic wastes [16]. Each earthworm weighs about 0.5 to 0.6 g, eats waste equivalent to its body weight, and produces cast equivalent to about 50% of the waste it consumes in a day. These worm castings have been analysed for chemical and biological properties. The moisture content of castings ranges between 32% and 66% and the pH is around 7.0. The final product of vermicompost bioprocess is called *humus* and it could be considered a driving force in the varying nature of terrestrial ecosystems [17]. Humus differs from the nonhumic substances such as carbohydrates (a major fraction of soil carbon), fats, waxes, alkanes, peptides, amino acids, proteins, lipids, and organic acids by the fact that distinct chemical formulae can be written for these nonhumic substances. Most small molecules of nonhumic substances are rapidly degraded by microorganisms within the soil. In contrast, soil humus is slow to decompose (degrade) under natural soil conditions. In combination with soil minerals, soil humus can persist for several hundred years. Some of the most beneficial attributes of humus are associated with its ability to make small, inorganic particles adhere together as loose, friable aggregates. Earthworm activities determine the soils' characteristics and take an active part in energy and nutrient cycling through the selective activation of both mineralization and humification processes [18].

Apparently, in earthworms the mineralization is biologically induced, which is described as a mostly unintentional consequence of metabolic activities in the microbial organism. The nanoparticles produced in this process are an extracellular by-product of the microbial metabolism. The bacteria or other types of microbe secrete organic products attract ions or compounds in their vicinity, which subsequently result in concentration, alteration, immobilization, or depletion of these minerals. This means that the formation of elemental crystals is not directly controlled by the microbe. This can produce random crystallization or a lack of specific crystal morphologies [19]. Minerals formed in this manner also tend to be impure in the crystal lattice and full of inclusions of other minerals and compounds [20]. Some works about biotransformation and the biomineralization process where earthworms are involved have been reported [21, 22]. In the earthworms intestine there exist a wide range of microorganisms, including bacteria, algae, protozoa, actinomycetes, fungi, and even nematodes, which are found commonly throughout the length of the earthworms gut. The species of microbes in the gut are usually very similar to those in the surrounding soil or organic matter upon which the earthworms feed. Earthworms are dependent upon range of microorganisms in their nutrition and probably fungi are the most important microbes as food. It seems likely that protozoa are also important in their diet but that bacteria and actinomycetes are much less important [23]. Several studies have showed that under certain conditions of pressure and temperature the biomineralization (silicification) can be induced in presence of microorganisms

and demonstrated that a complex interplay exists between the precipitations of silica, texture, and structures formed [24].

This study shows the structural characterization of silica particles extracted from grass *Stenotaphrum secundatum* (St. Augustine) using an annelid-based biotransformation process. The aim was to investigate changes in the properties of these particles caused by the bioprocess, and we propose that these biostructures could be used for the synthesis of new materials in a cheap and ecofriendly manner.

2. Materials and Methods

The seed of St. Augustine grass (*Stenotaphrum secundatum*) (Walt.) Kuntze was obtained from a commercial source, planted in a garden, and grown for about 3 months. Once mowed, it was added to the vermicompost. The specimen of annelid used was *Eisenia foetida*. The environmental conditions ideal for the reproduction and control of these samples were set up: temperature at 20°C, moisture around 60–85%, aeration conditions, and darkness. The stabilization time was around 1 month and the humus obtained was dried at room temperature. Then, the humus was sieved to a size of approximately 0.5 mm. Next, the sample was calcinated for 19 h at a temperature of 500°C to eliminate the organic matter. Calcinations were carried out in a muffle Lindberg/Eurotherm model 847 with energy consumption of 0.17 kcal/h cm³, and then the samples were treated with nitric and hydrochloric acids (volume ratio 3:1). For each gram of sample calcinated, 4 mL of acid mix was added in order to eliminate impurities. Acid treatment was performed at 40°C for 4 h with constant stirring. Then, the sample was filtrated and washed with distilled water to neutralize it. Solids obtained were dried at room temperature. All reagents employed were provided by Sigma-Aldrich. Silica obtained from St. Augustine grass without the bioprocess was used as a reference. The extraction process to obtain silica without bioprocess is the same described previously using calcination and acid treatment.

Silica powders were characterized to 64 scans by employing a Fourier transform infrared spectrophotometer (FTIR) Bruker Vector 33 with a resolution of 4 cm⁻¹, using KBr powders. Raman spectroscopy was performed in a Raman Senterra Bruker machine with a 100x microscope objective, laser emitting, at 785 nm and resolution 0.1 cm⁻¹. Transmission Electron Microscopy (TEM) was performed using a JEOL TEM-1010 transmission electron microscope. Average particle size was determined by Dynamic Light Scattering (DLS) using a Brookhaven model B1200SM with laser He-Ne of 35 mW model 9167 EB-1 Melles-Griot. Elemental analysis was carried out using energy dispersion spectroscopy (EDS) mean software Oxford Inca X-Sight. EDS is adapted in equipment JEOL JSM-6060 LV Scanning Electron Microscope. X-ray Diffraction (XRD) was performed in a diffractometer Rigaku, Model MiniFlex, with a wavelength from 1.54 Å corresponding to ka copper radiations. Crystalline structures present in the samples were analysed with Materials Data Jade software of MDI Materials Data.

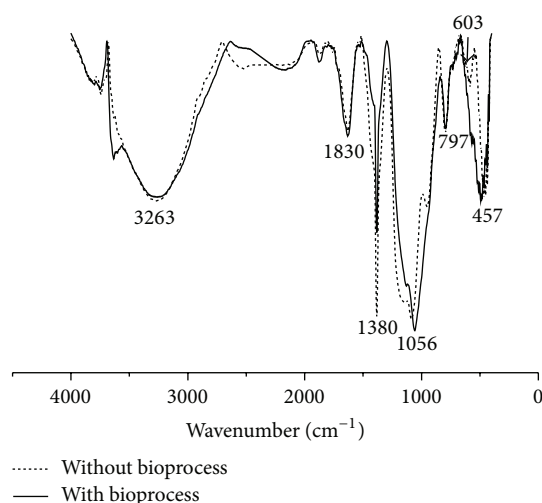


FIGURE 1: IR spectra of silica particles obtained for annelids bioprocess and without bioprocess.

3. Results and Discussion

3.1. Infrared Spectroscopy (FT-IR). Figure 1 presents FT-IR spectra of both samples of silica (with and without bioprocess). Every spectrum shows a wide peak at 3263 cm⁻¹ ascribable to the O–H stretching mode of water molecules as well as a peak assigned to the water hydroxyl deformation vibration at 1630 cm⁻¹—these bands correspond to adsorbed water that minerals contain physically [25, 26]. At 1379 cm⁻¹, there exists a band associated with the mineral phases of carbonates (i.e., calcite, dolomite, and aragonite); these compounds are common in soils and are generally produced by a biomineralization process. Although the carbonates can be thermally unstable, their stability increases with the type of cation associated and so can prevail even in the treatment conditions of the sample [27]. This band is less intense in the sample with bioprocess due in great part to the fact that this mineral source can be necessary in the metabolism of the earthworms. A band corresponding to Si–O asymmetrical stretching vibration was localized at 1056 cm⁻¹ [28], and this band is very similar in both samples with and without bioprocess. Another band localized at 797 cm⁻¹ (Si–O) is related to the presence of quartz in the sample [29]. In the region between 400 and 600 cm⁻¹, the sample with bioprocess shows a peak at 457 cm⁻¹ corresponding to Si–O–Si bending vibration [30]; without bioprocess the sample exhibits a peak in 603 cm⁻¹; this can be assigned to a compound silicate that contains magnesium [31]. In the bioprocess is a band not observed; however this can overlap with the band localized in 457 cm⁻¹. The results of FTIR show the existence of bands where silica prevails, but the differences in these bands (with and without bioprocess) can aid in explaining the mechanism of the bioprocess in the earthworms.

3.2. Raman Spectroscopy. The FT-Raman spectrum of the sample with and without bioprocess is shown in Figures 2(a) and 2(b). FT-Raman bands were well defined only in the

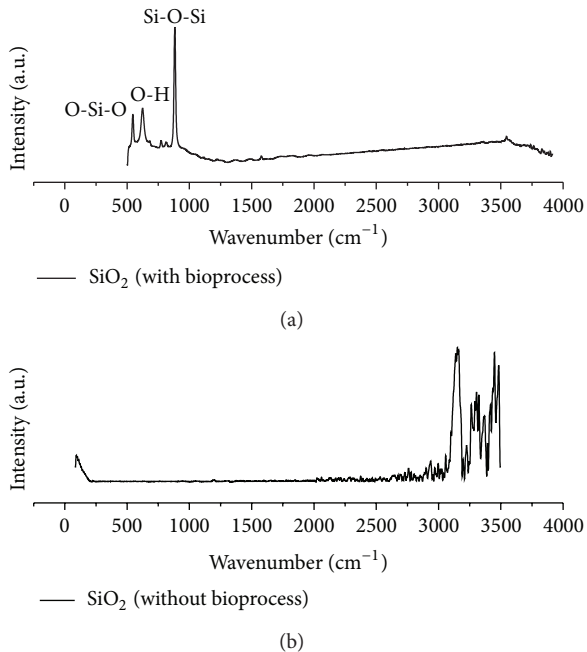


FIGURE 2: FT-Raman spectra of silica particles obtained for annelids bioprocess (a) and without bioprocess (b).

sample of silica with bioprocess (Figure 2(a)). These bands are localized at 122 cm^{-1} , 210 cm^{-1} , and 468 cm^{-1} . The first band at 122 cm^{-1} corresponds to an O–Si–O symmetric bend; the second band localized at 210 cm^{-1} is assigned to stretch vibration modes of O–H group, while the intense band localized at 468 cm^{-1} is associated with the Si–O–Si stretching vibration. This last band has a stronger intensity and belongs to the polymorph of silica α -quartz typically found at 465 cm^{-1} [32]. FT-Raman results confirm the presence of silica and suggest that in samples with bioprocess a crystalline arrangement is present in contrast with the samples without bioprocess, thus confirming that microorganisms contribute to the molecular ordering.

3.3. Transmission Electron Microscopy (TEM). TEM images of silica sample with bioprocess are shown in Figures 3(a)–3(c). In this case, the particles extracted using the annelid bioprocess have a morphology similar to spherical, they are grouped in clusters, and have a nanometric size. TEM images of silica sample without bioprocess are shown in Figures 3(d)–3(f). In this figure, particles were not identified nor had their morphology defined, but clusters and agglomerates were observed and their size apparently was bigger than particles without bioprocess. The results showed a difference in the morphology, dispersion, and size between the samples. Without the bioprocess, the particles have a tendency to be amorphous, while, with the bioprocess, these particles display more order and these differences are attributed to the vermicomposting bioprocess. Microorganisms play important role in this process due to the activity of classification and purification of the matter employed in their metabolic process.

3.4. X-Ray Diffraction (XRD). XRD diffractograms of the sample of silica with the bioprocess are given in Figure 4(a). Figure 4(a) shows characteristic peaks related to hexagonal quartz (Figure 4(a), peak 1)—this quartz has been identified earlier as belonging to a polymorph of silica. Also hexagonal tridymite (primitive) (Figure 4(a), peak 2) and triclinic albite (Figure 4(a), peak 3) polymorphs were identified. XRD diffractograms of the sample without the bioprocess are given in Figure 4(b). Figure 4(b) shows that the particles have a structure essentially amorphous and only two peaks related to hexagonal quartz polymorphs can be detected slightly (Figure 4(b), peaks 1). These results confirm that the bioprocess plays an important role in the transformation of the particles toward a crystalline structure. In this type of grass, polymorphs of silicates prevail, although, as can be observed in EDS, mineral elements exist that can produce other crystalline structures.

3.5. Dynamic Light Scattering (DLS). The mean diameter of particle estimated by DLS showed that with the bioprocess the particles achieved 530 nanometres while without the bioprocess the mean diameter was 1.6 micrometres. These results show that with the bioprocess the size of silica particles is smaller than the size of those without bioprocess. The mineral portion (phytoliths) in grass is generally microscopic; however, the metabolic activity of microorganisms inside the intestine of earthworms causes an important size reduction. This analysis shows that the size of particle can be affected by the trend of the samples to form agglomerates; this can be better observed in the sample without bioprocess.

3.6. Energy Dispersion Spectroscopy (EDS). Table 1 summarizes the results obtained using energy dispersion spectroscopy. A significant amount of silicon and oxygen weight percentage was observed in the samples: with bioprocess: 54.01% O and 30.69% Si and without bioprocess: 56.23% O and 35.44% Si. Table 1 shows other elements in lower proportion related to the biomineralization process and some were detected using the technique of X-ray Diffraction (Figure 4). Elements such as magnesium, aluminium, and iron increased their proportion when the bioprocess is used. The relationship of oxygen and silicon in the samples is similar, although the oxygen is slightly lower in the sample with the bioprocess due to this element being an important source in the metabolic process of earthworms and microorganisms. EDS showed the mineral elements in the samples with and without the bioprocess, and it is important to remark that elements such as sodium and calcium only are shown in the sample without the bioprocess, while in the bioprocess are elements that are an important source in the nutritional process of earthworms and can be used by the microorganisms.

4. Conclusions

The effect produced by the annelid bioprocess on the properties of silica particles obtained from St. Augustine grass was determined. The characterization of these particles was performed with FTIR, Raman spectroscopy, TEM, XDR,

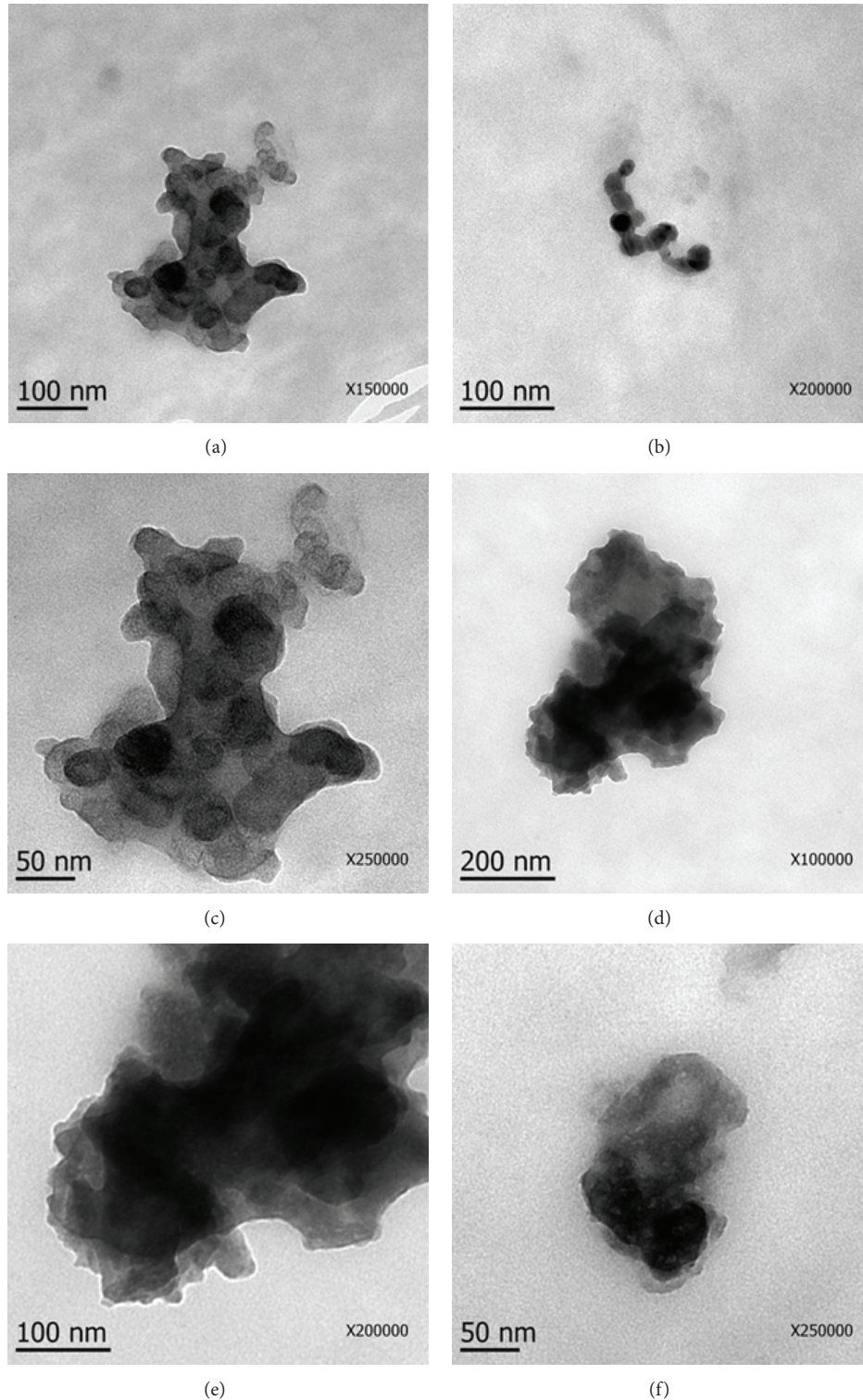


FIGURE 3: TEM images of silica particles obtained for annelids bioprocess (a–c) and without bioprocess (d–f).

DLS, and EDS. The particles obtained from the bioprocess contain mainly silica and OH groups and present a trend toward a spherical morphology; their size estimate by DLS was 530 nm, which is smaller than those particles without the bioprocess. The bioprocess produced structural order and

crystalline particles with prevailing α -quartz phase and other silicates such as tridymite and albite. The bioprocess shows others elements in minor proportion such as aluminium, magnesium, iron, and potassium. The characteristics of these types of particles obtained from the bioprocess using

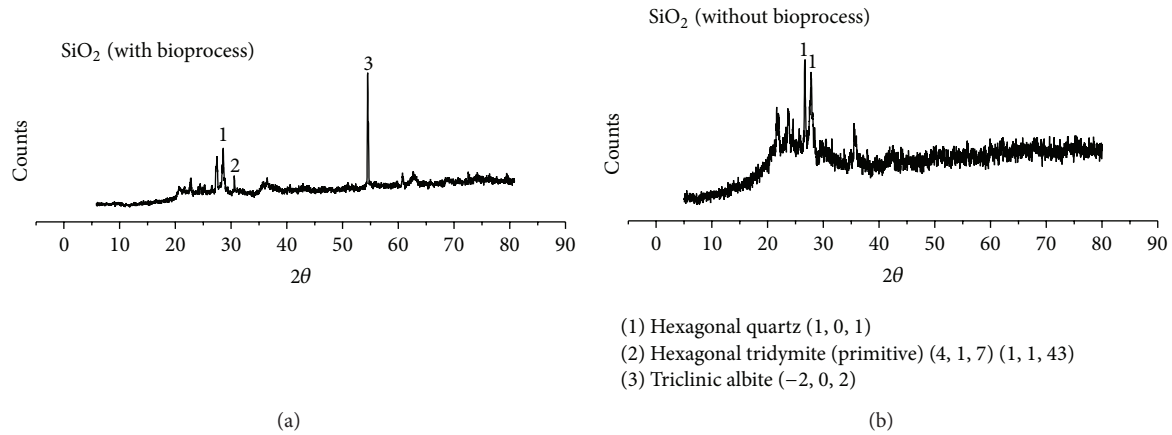


FIGURE 4: X-ray diffraction of silica particles obtained for annelids bioprocess (a) and without bioprocess (b).

TABLE 1: EDS to silica particles synthesized without bioprocess and with bioprocess.

Without bioprocess			With bioprocess		
Element	% atomic	% weight	Element	% atomic	% weight
O K	70.15	56.23	O K	68.25	54.01
Na K	0.49	0.56	Mg K	1.28	1.54
Mg K	0.44	0.54	Al K	6.13	8.18
Al K	1.06	1.43	Si K	22.09	30.69
Si K	25.19	35.44	K K	0.63	1.21
K K	1.12	2.19	Ti K	0.28	0.66
Ca K	0.81	1.62	Fe K	1.34	3.70
Ti K	0.28	0.68			
Fe K	0.47	1.31			
Total	100.00	100.00	Total	100.00	100.00

vermicompost and grass can contribute to explaining of the biological mechanism of vermicomposting specifically referred to as biomineralization. The results showed changes between the samples with and without the bioprocess. These changes are produced in the digestion process of earthworms together with the microorganisms involving separation, classification, purification, and transformation of the matter and therefore are named as biotransformation. This biological mechanism represents a novel alternative to create novel materials in a cheap and ecofriendly biostructure based manner.

Conflict of Interests

The authors declare that there is no conflict of interests regarding the publication of this paper.

Acknowledgments

The authors are grateful to Ms. Maria de Lourdes Palma for her assistance in TEM, to Dr. Genoveva Hernandez-Padron for her assistance in IR and Raman analysis, to Dr. Eric Rivera for his assistance in XRD, to Dr. Miriam Estevez Gonzalez for her assistance in DLS analysis, and also to M. T. Carrillo. Financial support from the National Council for Science and

Technology of Mexico (CONACYT) (PhD Scholarship to A. Espíndola-Gonzalez) is gratefully acknowledged.

References

- [1] F. P. Massey, A. R. Ennos, and S. E. Hartley, "Silica in grasses as a defence against insect herbivores: contrasting effects on folivores and a phloem feeder," *Journal of Animal Ecology*, vol. 75, no. 2, pp. 595–603, 2006.
- [2] P. B. Kaufman, P. Dayanandan, C. I. Franklin, and Y. Takeoka, "Structure and function of silica bodies in the epidermal system of grass shoots," *Annals of Botany*, vol. 55, no. 4, pp. 487–507, 1985.
- [3] F. J. Ma and N. Yamaji, "Silicon uptake and accumulation in higher plants," *Trends in Plant Science*, vol. 11, no. 8, pp. 392–397, 2006.
- [4] D. W. Parry, M. J. Hodson, and A. G. Sangster, "Some recent advances in studies of silicon in higher plants [and Discussion]," *Philosophical Transactions of the Royal Society B*, vol. 304, no. 1121, pp. 537–549, 1984.
- [5] F. M. Jian, K. Tamai, N. Yamaji et al., "A silicon transporter in rice," *Nature*, vol. 440, no. 7084, pp. 688–691, 2006.
- [6] F. J. Ma, "Role of silicon in enhancing the resistance of plants to biotic and abiotic stresses," *Soil Science and Plant Nutrition*, vol. 50, no. 1, pp. 11–18, 2004.

- [7] N. Yamaji, N. Mitatni, and F. M. Jian, "A transporter regulating silicon distribution in rice shoots," *Plant Cell*, vol. 20, no. 5, pp. 1381–1389, 2008.
- [8] J. F. Ma, N. Mitani, S. Nagao et al., "Characterization of the silicon uptake system and molecular mapping of the silicon transporter gene in rice," *Plant Physiology*, vol. 136, no. 2, pp. 3284–3289, 2004.
- [9] K. R. Iler, *The Chemistry of Silica: Solubility, Polymerization, Colloid and Surface Properties and Biochemistry of Silica*, John Wiley & Sons, Toronto, Canada, 1979.
- [10] A. Espindola-Gonzalez, A. L. Martinez-Hernandez, C. Angeles, V. M. Castano, and C. Velasco-Santos, "Novel crystalline SiO₂ nanoparticles via annelids bioprocessing of agro-industrial wastes," *Nanoscale Research Letters*, vol. 5, no. 9, pp. 1408–1417, 2010.
- [11] J. D. Sauer, "Revision of *Stenotaphrum* (Gramineae: paniceae) with attention to its historical geography," *Brittonia*, vol. 24, no. 2, pp. 202–222, 1972.
- [12] A. D. Genovesi, R. W. Jessup, M. C. Egelke, and B. L. Burson, "Interploid St. Augustinegrass [*Stenotaphrum secundatum* (Walt.) Kuntze] hybrids recovered by embryo rescue," *In Vitro Cellular & Developmental Biology—Plant*, vol. 45, no. 6, pp. 659–666, 2009.
- [13] L. E. Datnoff, M. O. Brecht, C. M. Stiles, and B. A. Rutherford, "The role of silicon in suppressing foliar diseases in warm season turf," *International Turfgrass Society Research Journal*, vol. 10, pp. 175–179, 2005.
- [14] S. Adhikary, "Vermicompost, the story of organic gold: a review," *Agricultural Sciences*, vol. 3, no. 7, pp. 905–917, 2012.
- [15] C. A. Edwards and J. R. Lofty, *Biology of Earthworms*, Bookworm Publishing Company, Beckville, Tex, USA, 1976.
- [16] E. Albanell, J. Plaixats, and T. Cabrero, "Chemical changes during vermicomposting (*Eisenia fetida*) of sheep manure mixed with cotton industrial wastes," *Biology and Fertility of Soils*, vol. 6, no. 3, pp. 266–269, 1988.
- [17] J.-F. Ponge, "Humus forms in terrestrial ecosystems: a framework to biodiversity," *Soil Biology and Biochemistry*, vol. 35, no. 7, pp. 935–945, 2003.
- [18] P. Lavelle, "Earthworm activities and the soil system," *Biology and Fertility of Soils*, vol. 6, no. 3, pp. 237–251, 1988.
- [19] P. P. Provencio and V. J. Polyak, "Iron oxide-rich filaments: possible fossil bacteria in Lechuguilla Cave, New Mexico," *Geomicrobiology Journal*, vol. 18, no. 3, pp. 297–309, 2001.
- [20] B. R. Frankel and A. D. Bazylinski, "Biologically induced mineralization by bacteria," *Reviews in Mineralogy and Geochemistry*, vol. 54, no. 1, pp. 95–114, 2003.
- [21] L. Gago-Duport, M. J. I. Briones, J. B. Rodríguez, and B. Covelo, "Amorphous calcium carbonate biomineralization in the earthworm's calciferous gland: pathways to the formation of crystalline phases," *Journal of Structural Biology*, vol. 162, no. 3, pp. 422–435, 2008.
- [22] J. Mendez, J. B. Rodríguez-González, R. Alvarez-Otero, I. M. J. Briones, and L. Gago-Duport, "Crystallization stages of the CaCO₃ deposits in the earthworm's calciferous gland," in *EMC 2008 14th European Microscopy Congress 1–5 September 2008, Aachen, Germany*, pp. 127–128, Springer, Berlin, Germany, 2008.
- [23] A. C. Edwards and E. K. Fletcher, "Interactions between earthworms and microorganisms in organic-matter breakdown," *Agriculture, Ecosystems & Environment*, vol. 24, no. 1–3, pp. 235–247, 1988.
- [24] M. G. Gad, T. K. Semple, and M. H. Lappin-Scott, *Micro-Organisms and Earth Systems*, Society for General Microbiology. Symposium 65, Cambridge University Press, Cambridge, UK, 2005.
- [25] J. W. Stucki, J. Wu, H. Gan, P. Komadel, and A. Banin, "Effects of iron oxidation state and organic cations on dioctahedral smectite hydration," *Clays and Clay Minerals*, vol. 48, no. 2, pp. 290–298, 2000.
- [26] Y. Kitagawa, "Determination of allophane and amorphous inorganic matter in clay fraction of soils I. Allophane and allophane-halloysite mixture," *Soil Science and Plant Nutrition*, vol. 22, no. 2, pp. 137–147, 1976.
- [27] M. R. Hazen, T. R. Downs, P. A. Jones, and L. Kah, "Carbon mineralogy and crystal chemistry," *Reviews in Mineralogy and Geochemistry*, vol. 75, no. 1, pp. 7–46, 2013.
- [28] A. L. Radu, G. I. Truica, R. Penu, V. Moroeanu, and S. C. Litescu, "Use of the Fourier transform infrared spectroscopy in characterization of specific samples," *UPB Scientific Bulletin B: Chemical and Materials Science*, vol. 74, no. 4, pp. 137–148, 2012.
- [29] C. Ascaso, L. G. Sancho, and C. Rodriguez-Pascual, "The weathering action of saxicolous lichens in maritime Antarctica," *Polar Biology*, vol. 11, no. 1, pp. 33–39, 1990.
- [30] M. B. Caruta, *Nanomaterials Researchs*, Nova Science Publisher, New York, Ny, USA, 2006.
- [31] B. J. Saikia, G. Parthasarathy, and N. C. Sarmah, "Spectroscopic Characterization of Olivine [(Fe,Mg)₂SiO₄] in Mahadevpur H4/5 ordinary chondrite," *Journal of American Science*, vol. 5, pp. 71–78, 2009.
- [32] G. Jovanovski, P. Makreski, B. Kaitner, and B. Boev, "Silicate minerals from Macedonia. Complementary use of vibrational spectroscopy and X-ray powder diffraction for identification and detection purposes," *Croatica Chemica Acta*, vol. 82, no. 2, pp. 363–386, 2009.

Research Article

Fabrication of SERS Active Surface on Polyimide Sample by Excimer Laser Irradiation

T. Csizmadia,¹ B. Hopp,¹ T. Smausz,² Zs. Bengery,¹ J. Kopniczky,¹
I. Hanyecz,¹ and G. Szabó^{1,2}

¹ Department of Optics and Quantum Electronics, University of Szeged, Dóm tér 9 Szeged 6720, Hungary

² MTA-SZTE Research Group on Photoacoustic Spectroscopy, University of Szeged, Dóm tér 9 Szeged 6720, Hungary

Correspondence should be addressed to T. Csizmadia; csizmadia87@gmail.com

Received 16 October 2013; Accepted 31 January 2014; Published 2 March 2014

Academic Editor: Denis Chaumont

Copyright © 2014 T. Csizmadia et al. This is an open access article distributed under the Creative Commons Attribution License, which permits unrestricted use, distribution, and reproduction in any medium, provided the original work is properly cited.

A possible application of excimer laser irradiation for the preparation of surface enhanced Raman spectroscopy (SERS) substrate is demonstrated. A polyimide foil of 125 μm thickness was irradiated by 240 pulses of focused ArF excimer laser beam ($\lambda = 193$ nm, FWHM = 20 ns). The applied fluence was varied between 40 and 80 mJ/cm^2 . After laser processing, the sample was coated with 40 nm silver by PLD in order to create a conducting layer required for the SERS application. The SERS activity of the samples was tested by Raman microscopy. The Raman spectra of Rhodamine 6G aqueous solution ($c = 10^{-3}$ mol/dm^3) were collected from the patterned and metalized areas. For areas prepared at 40–60 mJ/cm^2 laser fluences, the measured Raman intensities have shown a linear dependence on the applied laser fluence, while above 60 mJ/cm^2 saturation was observed. The morphology of the SERS active surface areas was investigated by scanning electron microscopy. Finite element modeling was performed in order to simulate the laser-absorption induced heating of the polyimide foil. The simulation resulted in the temporal and spatial distribution of the estimated temperature in the irradiated polyimide sample, which are important for understanding the structure formation process.

1. Introduction

Raman spectroscopy (RS) is one of the most common spectroscopic methods for studying the vibrational and rotational energy levels of an analyte [1]. Compared to other spectroscopic techniques, RS is fast and nondestructive and needs practically no sample preparation and its microscope/imaging version has very good lateral resolution (about 1–2 μm). However, since only a very small fraction of the incident photons are Raman scattered (in general, the intensity of the Raman signal is orders of magnitude weaker than the elastic scattering intensity) [2], the range of detectable molecules and concentrations is significantly reduced. For that reason, enhancing the Raman signal produced by molecules was always in the focus of attention.

A significant increase of the Raman signal can be achieved when the target molecules are adsorbed on adequately structured conducting surfaces. According to theory [3], surface enhanced Raman scattering (SERS) can be attributed to the laser-induced excitation of surface plasmons, resulting in the

increase of the local electric field above the surface. The Raman intensities strongly depend on the magnitude of the developed electric near field, and thereby high enhancement can occur in the measured signal (up to 10^{10} in certain cases) [4].

One of the most widely used SERS active substrates is metal colloids (especially aggregated colloids) produced by chemical methods [5–8]. Another study aimed at the production of appropriate composite arrangement, where silver colloids were prepared by adding silver nitrate to the aqueous solution of excess sodium borohydride, the reducing agent. The silver colloids were then deposited on smooth silver, copper, and nickel plates. The composite structure was obtained by inserting a monolayer or submonolayer of organic molecules between two of these silver-colloid-covered metal substrates in a sandwich arrangement. On this way the analyte molecules are adsorbed onto the metal plates as ligands and are also in close contact with the silver nanoparticles, which ensure the enhancement for the Raman spectra of the adsorbates [9].

In another experiment, pulsed laser ablation (PLA) was used to fabricate silver chloride (AgCl) nanocubes directly from a bulk target of silver in sodium chloride (NaCl) solution. The size of the particles was optimized and the surface properties of the cubes were investigated for their SERS activity for Rhodamine 6G (R6G). The results indicated that the AgCl nanocubes obtained using PLA could largely enhance the Raman signal of R6G molecules, which makes them a useful substrate for practical SERS measurements [10].

In our previous study, the applicability of the laser-induced backside dry etching (LIBDE) technique was demonstrated to form such nanostructures on the surface of a fused silica plate, which are able to produce the SERS effect, when they are subsequently coated with a conducting layer. This method proved to be a relatively cheap and promising technique in the production of SERS substrates without the necessity of specific toolkits; however, the reproducibility of the most suitable surface structures and the size of the nanostructured area on the surface need to be improved for practical use [11].

In this paper the preparation of nanostructures by excimer laser irradiation of polyimide foil is presented and the suitability of the produced morphologies in creating the surface enhanced Raman scattering effect is demonstrated. Our motivation was to produce a relatively large and homogeneous surface with remarkable SERS activity and good reproducibility by the use of a simple laser-based micromachining technique and cheap substrate material.

2. Experiments

Kapton HN polyimide foil of 125 μm thickness was irradiated by 240 pulses of focused ArF excimer laser beam ($\lambda = 193 \text{ nm}$, FWHM = 20 ns). The penetration depth at this laser wavelength is as low as 23 nm due to the high absorption coefficient of polyimide ($\alpha = 43 \mu\text{m}^{-1}$ @ 193 nm) [12]. The illuminated area was 7.07 mm^2 and the applied fluence was varied between 40 and 80 mJ/cm^2 , which was verified by an out-coupled reference beam during the irradiations. After each series of pulses, the sample was moved by an x - y translator, in order to ensure an intact surface area for the next series. Due to the laser treatment, the irradiated surface darkened, which was more discernible in the lower part of the applied fluence range. Previously, Ball et al. observed the decrease in the reflectivity of polyimide due to the formation of carbon clusters on the excimer laser illuminated polymer surface [13, 14].

Although former experiments showed that the electrical conductivity of the polyimide surface increases significantly in response to the excimer laser irradiation [13–15], our attempts to use these solely laser treated surfaces as SERS substrates were unsuccessful. In order to insure the sufficient conducting surface for SERS, the laser patterned surfaces were coated with a thin layer of silver produced by pulsed laser deposition (PLD). The PLD process was carried out in a vacuum chamber at a pressure of approximately $4.5 \cdot 10^{-3} \text{ Pa}$, by using the same ArF excimer laser applied for surface structuring. In this case the laser beam was focused onto a silver target at an incident angle of 45° , which generated a spot

size of 4.24 mm^2 and an average fluence of 570 mJ/cm^2 . The target sample was shot by 15 000 laser pulses and the ejected silver clouds were deposited onto the polyimide surface placed 3 cm directly in front of the silver target. The thickness of the produced silver film was 40 nm on the average, which was measured by a Dektak 8 surface profiler after the PLD process.

3. Results and Discussion

After the deposition of the thin conducting metal layer, SERS activity of the laser-irradiated and silver covered polyimide surface areas was tested by a Thermo Scientific DXR Raman microscope, operated at laser wavelength of 780 nm and laser power of 5 mW using a 10x objective and a 50 μm slit. $10^{-3} \text{ mol}/\text{dm}^3$ aqueous solution of Rhodamine 6G (R6G) dye was used as test sample. The polyimide foil was fixed on the bottom of a Petri dish and the dye solution was streamed to the dish until it just covered the sample. The thickness of the R6G solution above the sample was few hundreds of micrometers, which was high enough to consider the concentration of R6G to be constant during the Raman measurements, which took a few minutes. Optical microscope images taken from the excimer laser treated sample exhibited circular spots of about 3 mm in diameter, corresponding to the irradiated areas. Since the irradiation experiments were carried out around the ablation and carbonization threshold fluence values, the laser-induced changes were very sensitive for the inhomogeneities of the excimer laser beam intensity. This could be seen in the morphological inhomogeneities of the resulting spots as well. In each laser spot three specific (bright, gray, and dark) terrains could be distinguished. The Raman exciting laser beam was focused in a few μm sized spot onto the studied surface of a given laser treated area, and at least four Raman spectra were recorded on every specific terrain type. The characteristic Raman shift peaks of polyimide did not appear in the Raman spectra during SERS investigations, since the transmittance of the applied silver film was less than 4% [16], which means that only a very small portion of the intensity of the Raman laser light reached the surface of the polyimide sample and an even smaller amount of the scattered light left it, which resulted in the disappearance of the characteristic polyimide peaks observed during reference measurements on the uncoated samples. The characteristic Raman shift peaks of the R6G at 611, 773, 1362, and 1510 cm^{-1} [17] were identified in every recorded spectrum. On the bright and dark terrains, there was no significant SERS enhancement; nevertheless on the gray shaded places strong increases were observed in the intensity of the characteristic peaks with about 13% standard deviations.

Figure 1 shows the dependence of the measured Raman intensities on the applied excimer laser fluence in case of the SERS active terrains of the irradiated spots at the four wavenumbers of the selected peaks in the R6G spectrum. It can be seen that a higher patterning fluence results in higher Raman intensities in the investigated range. Between 40 and 60 mJ/cm^2 , the tendency of the measured Raman intensity

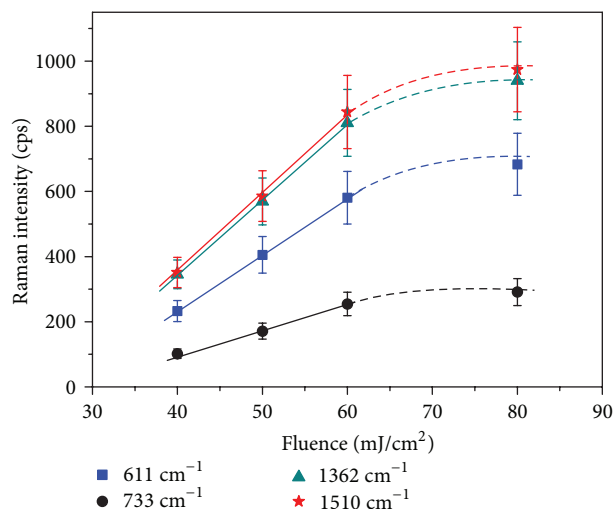


FIGURE 1: The average Raman intensity set against the applied patterning laser fluence in case of the most SERS active terrains of the irradiated spots at the typical peaks of the R6G Raman spectrum.

curves can be fairly approximated with a linear function, while, above 60 mJ/cm^2 , saturation can be observed.

The morphology of the sample surface was investigated by a Hitachi S4700 scanning electron microscope (SEM) in order to study the nanometer-sized structures, which can be relevant in causing the SERS effect. In order to prevent the investigated surface from charging or electron beam induced modification, a relatively low, 1 kV accelerating voltage and $4 \mu\text{A}$ emission current were used without the application of any additional conductive coating (in addition to the PLD deposited silver thin film), which would have covered the existing nanostructures.

Figure 2 shows the low magnification images of the silver coated surface areas of polyimide irradiated at different fluences. Three characteristic terrains can be distinguished macroscopically in almost each etched hole: dark, gray, and bright terrains, which are marked with green (1), blue (2), and red (3) fills and outlines, respectively, in Figure 2. These separated terrain types are equivalent to those, which were identified previously on the optical microscope image of the Raman system. For all fluences, the gray part (marked with green and (1) in Figure 2)—where significant Raman enhancements could be observed—covers at least half of the total irradiated area. This means that the ratio of this SERS useful area compared to the total irradiated area is at least twice more than it was for the etched holes prepared by LIBDE in our former experiments [11].

Figure 3 represents high magnification SEM images of the SERS active surfaces, where conical-like structures with variable size can be noticed typically. The average size of the cones increased with increasing fluence, and also the conical shapes were more defined as it was also revealed previously by Hopp et al. [18]. Between the conical structures, the surface is densely covered by irregular debris for all irradiation fluences (Figure 4). It is discernible from Figure 4 that at higher

fluences the surface coverage by debris-like structures is higher, and a more expressed fine structure can be seen overall. Considering the small standard deviations experienced in the SERS enhancements at various places of the gray terrain, it is likely that rather these finely structured terrains having extensive coverage on the irradiated surface are responsible for the generation of the SERS effect than the sparsely located conical structures.

Energy dispersive X-ray spectroscopy (EDX) measurements revealed that the proportion of carbon atoms increased inside the laser processed terrains: 5.5% increment was found in the gray terrains and 9.1% in the dark ones on the average. This indicates that the generated surface structures may not only consist of pure polyimide, but carbon clusters and polyimide fragments as well, which was proved by Chtaib et al. in earlier XPS measurements on ArF excimer laser irradiated polyimide [19]. It is known that in case of polyimide at temperatures higher than 793 K a chemical decomposition occurs instead of melting or evaporation [20]. Our observations imply that high temperature induced surface patterning of polyimide is a criterion for its SERS activity, which needs sufficiently high temperature provided by the absorption of the applied laser energy. In order to model this process, the spatial and temporal temperature distribution in the irradiated polyimide foil was calculated by finite element modeling, using the Comsol Multiphysics package. The absorbed laser energy in the polyimide was considered to be a heat source, which has a Gaussian temporal profile and an exponential spatial (depth) profile according to the Beer-Lambert absorption law. The results showed that the temperature of the irradiated foil exceeds the decomposition temperature of the polyimide down to 140 nm depth after one laser pulse of 40 mJ/cm^2 fluence, which explains the chemical modifications on the irradiated surface observed by EDX. Furthermore, ablation occurs in the whole applied fluence range, since the applied fluence was above the ablation threshold fluence ($\sim 25 \text{ mJ/cm}^2$ for polyimide at 193 nm [21]). The ablation process is important regarding the mechanism of the surface structure formation. It has been observed earlier that direct etching that is ablation of polyimide can result in microstructures having well-defined shapes [18, 22, 23], which are conical in case of our experimental conditions [18]. However, our results indicate that in the SERS point of view not the conical microstructures are responsible for activating the SERS effect, but the ablated polyimide micro- and nanofragments, which are backscattered from the plume and redeposited onto the irradiated polymer surface, have a substantial role. This effect is similar to the inverse PLD, discovered by Égerházi et al. [24]. Not only the fine structure but also the quantity of the ablated and redeposited material is a significant parameter concerning the SERS activity of the surface. In order to find out the role of these we measured the etch depths of the ablated holes by a Dektak 8 surface profiler. Knowing the irradiated area and the depths of the etched holes, we could give an upper estimation for the ablated volume of the ablated material as a function of the applied laser fluence (Figure 5). The calculated volume of the removed material during excimer laser ablation and the measured Raman intensity shows similar tendencies as

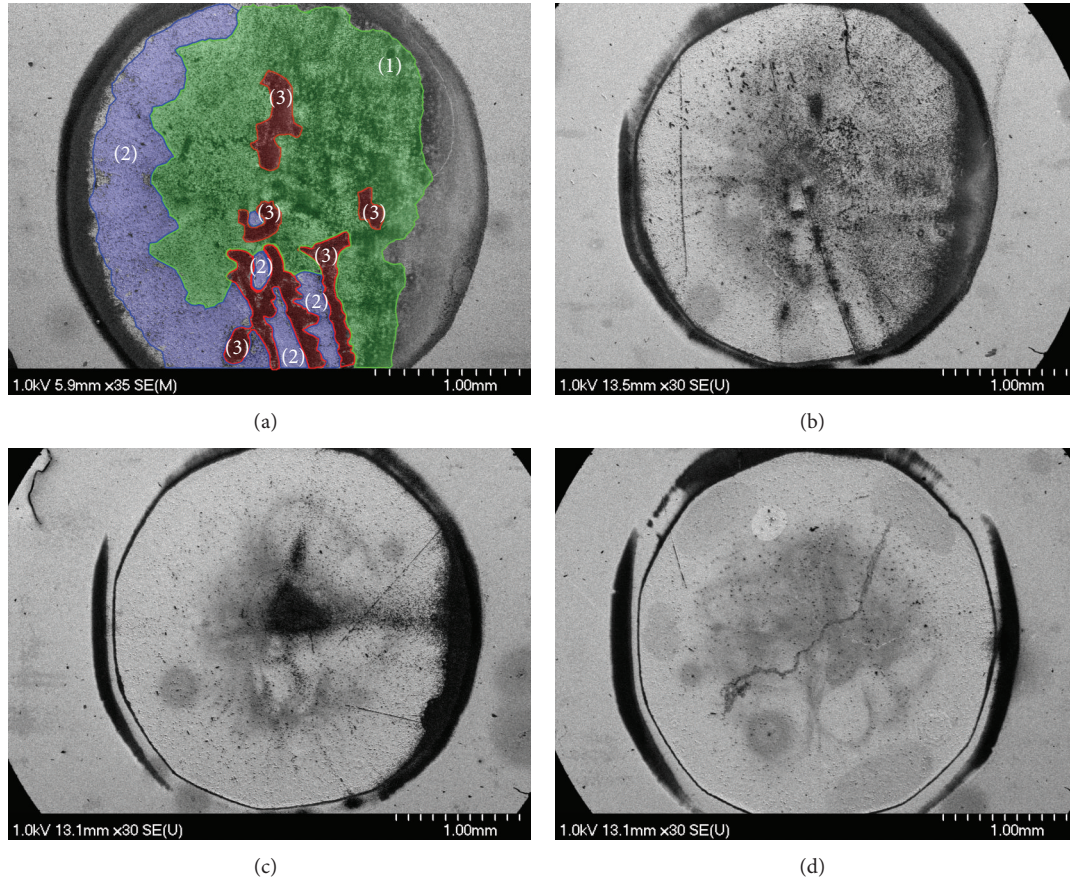


FIGURE 2: Low magnification SEM pictures on the laser treated spots produced by different excimer laser fluences: 40 (a); 50 (b); 60 (c); and 80 mJ/cm² (d). The marked numbered areas indicate the three distinguishable terrain types.

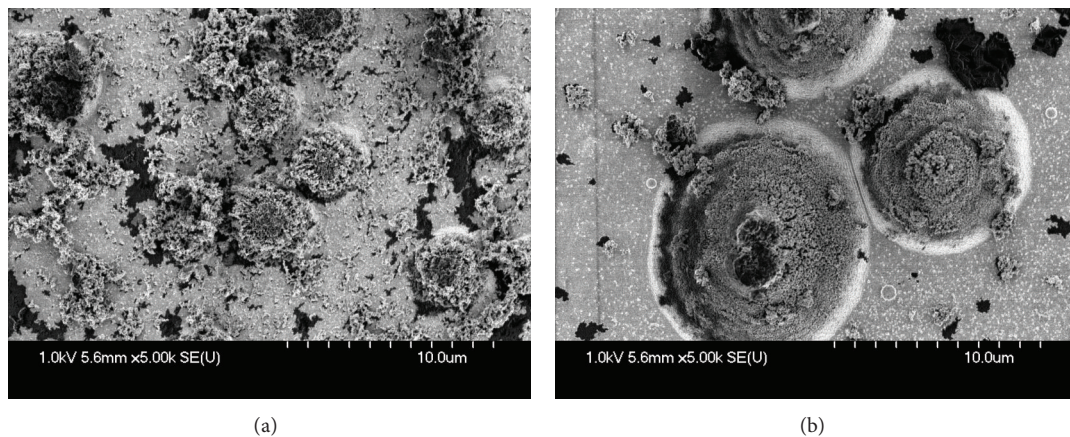


FIGURE 3: High magnification (5 000x) SEM images on the SERS active surfaces prepared at 40 (a) and 80 (b) mJ/cm² fluences.

functions of fluence (Figure 1) indicating that there might be a correlation between these two separate processes.

Regarding the mechanism of the SERS activity of the system, it is known that silver layers having approximately 40 nm thickness support plasmon resonances [25]. Besides

that, it is plausible that the enhancement of the Rhodamine 6G peaks on nanostructured silver surface may not only result from an enhancement in the electric field provided by the surface, but the interaction of chemisorbed R6G molecules with ballistic electrons that are generated through plasmon

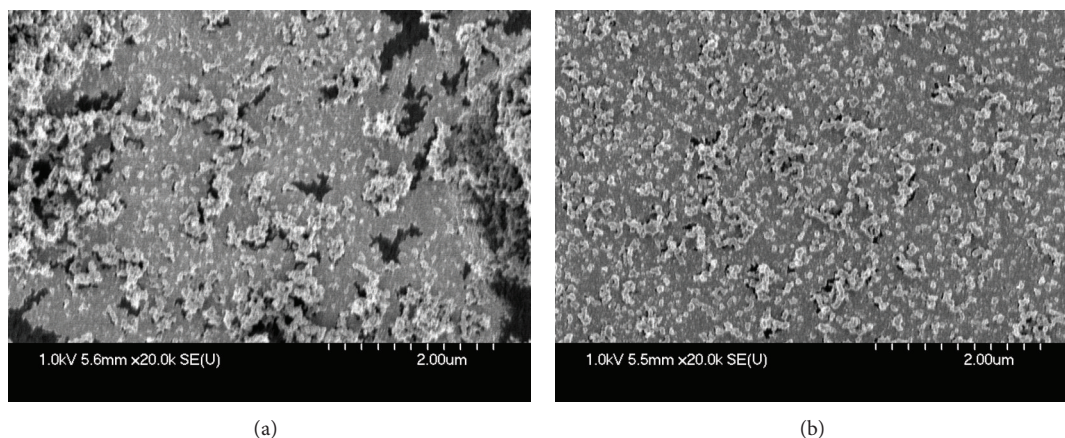


FIGURE 4: 20 000x magnification images on the fine structures of two SERS active surface areas fabricated at 40 (a) and 80 (b) mJ/cm^2 fluences.

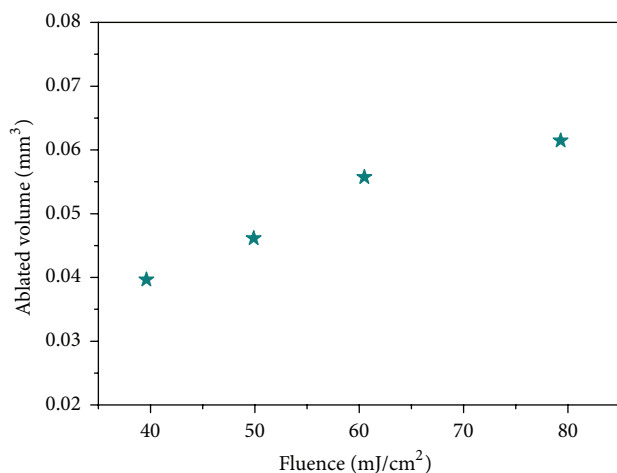


FIGURE 5: The dependence of the etch depth on the applied laser fluence during polyimide ablation.

excitation. A detailed discussion of such mechanism was presented by Michaels et al. regarding single molecule SERS of Rhodamine 6G in the presence of silver nanoparticles [26].

4. Conclusions

The preparation of micro- and nanostructures by excimer laser irradiation of polyimide was presented for the purpose of manufacturing a substrate for surface enhanced Raman scattering applications. In order to reach the necessary conductivity of the surface for SERS, the laser treated polyimide foil was covered by a thin layer of silver by PLD. Three types of typical structures could be discerned in each irradiated spot: dark, gray, and bright terrains regarding the optical microscopic investigations and low-magnification SEM images. Considerable SERS intensity enhancement was observed on the gray parts of the irradiated areas compared to the unirradiated and also metal coated surface areas. We found that the SERS activity of the irradiated areas prepared at higher laser fluences was higher. By taking a closer look at the

gray parts of the irradiated spots by SEM and recording EDX spectra at the same places, we observed that besides conical microstructures the surface morphology is finely structured, and indications for chemical decomposition (carbonization) can be observed. Our model calculations for spatial and temporal temperature distribution in the irradiated polyimide foil have proved that the required conditions are fulfilled not only for chemical decomposition but also for ablation. Therefore we presume that redeposition of micro- and nanofragments backscattered from the plume during the ablation process resulted in the observed fine structure of the SERS active areas.

As a conclusion, the applied polyimide is a cheap material for SERS substrate purposes, while nanosecond excimer laser irradiation is a fast production method without the need of any specific toolkits excepting the irradiating laser source. Regarding the structured surface of the created substrate, the size of the SERS active area covered at least half of the total irradiated area in case of every fluence values, which is more than 7 times larger in absolute value than the most enhancing area in our former experiments, where the SERS substrate was prepared by LIBDE, which is a slightly complicated method for material fabrication [11]. In addition, considering the 13% standard deviation in the measured Raman intensities of the characteristic peaks of the R6G, the reproducibility of the produced structures was good.

Conflict of Interests

The authors declare that there is no conflict of interests regarding the publication of this paper.

Acknowledgments

This work was partially supported by the European Union and cofinanced by the European Social Fund through projects Impulse Lasers for Use in Materials Science and Biophotonics (Grant no. TÁMOP-4.2.2.A-11/1/KONV-2012-0060) and Supercomputer, the National Virtual Lab (TÁMOP-4.2.2.C-11/1/KONV-2012-0010) and was realized in the frames of

National Excellence Program-Elaborating and Operating an Inland Student and Researcher Personal Support System Convergence program (TÁMOP 4.2.4. A/2-11-1-2012-0001).

References

- [1] E. Smith and G. Dent, *Modern Raman Spectroscopy—A Practical Approach*, John Wiley & Sons, Hoboken, NJ, USA, 2005.
- [2] D. W. Hahn, “Raman Scattering Theory,” 2014, <http://plaza.ufl.edu/dwhahn/Raman%20Scattering%20Theory.pdf>.
- [3] M. Moskovits, “Surface-enhanced Raman spectroscopy: a brief retrospective,” *Journal of Raman Spectroscopy*, vol. 36, no. 6-7, pp. 485–496, 2005.
- [4] P. G. Etchegoin and E. C. le Ru, *Basic Electromagnetic Theory of SERS, Surface Enhanced Raman Spectroscopy: Analytical, Biophysical and Life Science Applications*, Wiley-VCH, Weinheim, Germany, 2011.
- [5] A. Débarre, R. Jaffiol, C. Julien, P. Tchénié, and M. Mostafavi, “Raman scattering from single Ag aggregates in presence of EDTA,” *Chemical Physics Letters*, vol. 386, no. 4–6, pp. 244–247, 2004.
- [6] M. Z. Si, Y. P. Kang, and Z. G. Zhang, “Surface-enhanced Raman scattering (SERS) spectra of Methyl Orange in Ag colloids prepared by electrolysis method,” *Applied Surface Science*, vol. 255, no. 11, pp. 6007–6010, 2009.
- [7] J. G. S. Lopes and P. S. Santos, “The SERS spectrum of 1,2-diaminoanthraquinone studied on silver colloid,” *Journal of Molecular Structure*, vol. 744–747, pp. 75–78, 2005.
- [8] M. Muniz-Miranda, N. Neto, and G. Sbrana, “Surface studies by SERS and SEM techniques on filters coated with colloidal silver,” *Journal of Molecular Structure*, vol. 410–411, pp. 205–208, 1997.
- [9] M. Muniz-Miranda, B. Pergolese, A. Bigotto, A. Giusti, and M. Innocenti, “A Raman and AFM investigation on metal surfaces SERS-activated by silver colloidal nanoparticles,” *Materials Science and Engineering C*, vol. 27, no. 5–8, pp. 1295–1299, 2007.
- [10] C. Dong, Z. Yan, J. Kokx, D. B. Chrisey, and C. Z. Dinu, “Antibacterial and surface-enhanced Raman scattering (SERS) activities of AgCl cubes synthesized by pulsed laser ablation in liquid,” *Applied Surface Science*, vol. 258, pp. 9218–9222, 2012.
- [11] T. Csizmadia, B. Hopp, T. Smausz et al., “Possible application of laser-induced backside dry etching technique for fabrication of SERS substrate surfaces,” *Applied Surface Science*, vol. 278, pp. 234–240, 2013.
- [12] H. R. Philipp, H. S. Cole, Y. S. Liu, and T. A. Sitnik, “Optical absorption of some polymers in the region 240–170 nm,” *Applied Physics Letters*, vol. 48, no. 2, pp. 192–194, 1986.
- [13] Z. Ball, B. Hopp, M. Csete et al., “Transient optical properties of excimer-laser-irradiated polyimide—I. Refractive index,” *Applied Physics A*, vol. 61, no. 5, pp. 547–551, 1995.
- [14] Z. Ball, B. Hopp, M. Csete et al., “Transient optical properties of excimer-laser-irradiated polyimide—II. Carbon-cluster scattering,” *Applied Physics A*, vol. 61, no. 6, pp. 575–578, 1995.
- [15] B. Hopp, Z. Szilassi, K. Révész, Z. Kocsis, and I. Mudra, “Excimer laser induced conductivity on silver salt filled polyimide films,” *Applied Surface Science*, vol. 109–110, pp. 212–217, 1997.
- [16] <http://refractiveindex.info>, 2014.
- [17] X. Hou, X. Zhang, S. Chen, H. Kang, and W. Tan, “Facile synthesis of Ni/Au, Ni/Ag hybrid magnetic nanoparticles: new active substrates for surface enhanced Raman scattering,” *Colloids and Surfaces A*, vol. 403, pp. 148–154, 2012.
- [18] B. Hopp, Zs. Bor, E. Homolya, and E. Mihalik, “Conical structures produced by excimer laser irradiation of polymers,” in *GR-I International Conference on New Laser Technologies and Applications*, vol. 3423 of *Proceedings of the SPIE*, pp. 389–393, 1997.
- [19] M. Chtaib, E. M. Roberfroid, Y. Novis, J.-J. Pireaux, and R. Caudano, “Polyimide surface degradation: x-ray photoelectron spectroscopic study under UV-pulsed laser irradiation,” *Metalization of Polymers*, vol. 11, pp. 161–169, 1990.
- [20] Dupont Kapton Polyimide Film General Specifications, Bulletin GS-96-7, 2014, http://www2.dupont.com/Kapton/en_US/assets/downloads/pdf/Gen.Specs.pdf.
- [21] M. Kahrizi, “Laser ablation for polymer waveguide fabrication,” in *Micromachining Techniques for Fabrication of Micro and Nano Structures*, S. Zakariyah, Ed., InTech, Rijeka, Hungary, 2012.
- [22] H. Y. Zheng, T. T. Tan, and W. Zhou, “Studies of KrF laser-induced long periodic structures on polyimide,” *Optics and Lasers in Engineering*, vol. 47, no. 1, pp. 180–185, 2009.
- [23] B. T. Least and D. A. Willis, “Modification of polyimide wetting properties by laser ablated conical microstructures,” *Applied Surface Science*, vol. 273, pp. 1–11, 2013.
- [24] L. Égerházi, Zs. Geretovszky, T. Csákó, and T. Szörényi, “Atomic force microscopic characterization of films grown by inverse pulsed laser deposition,” *Applied Surface Science*, vol. 252, pp. 4661–4666, 2006.
- [25] S. K. Cushing, L. A. Hornak, J. Lankford, Y. Liu, and N. Wu, “Origin of localized surface plasmon resonances in thin silver film over nanosphere patterns,” *Applied Physics A*, vol. 103, no. 4, pp. 955–958, 2011.
- [26] A. M. Michaels, M. Nirmal, and L. E. Brus, “Surface enhanced Raman spectroscopy of individual rhodamine 6G molecules on large Ag nanocrystals,” *Journal of the American Chemical Society*, vol. 121, no. 43, pp. 9932–9939, 1999.

Research Article

Nanocrystalline Al Composites from Powder Milled under Ammonia Gas Flow

J. Cintas,¹ E. S. Caballero,¹ J. M. Montes,¹ F. G. Cuevas,² and C. Arevalo¹

¹ *Metallurgy and Materials Engineering Group, Escuela Técnica Superior de Ingeniería, University of Seville, Camino de los Descubrimientos s/n, 41092 Sevilla, Spain*

² *Department of Chemistry and Materials Science, Escuela Técnica Superior de Ingeniería, University of Huelva, Campus La Rábida, Carretera Palos s/n, Palos de la Frontera, 21819 Huelva, Spain*

Correspondence should be addressed to J. Cintas; jcintas@us.es

Received 22 October 2013; Revised 14 January 2014; Accepted 15 January 2014; Published 27 February 2014

Academic Editor: Denis Chaumont

Copyright © 2014 J. Cintas et al. This is an open access article distributed under the Creative Commons Attribution License, which permits unrestricted use, distribution, and reproduction in any medium, provided the original work is properly cited.

The production of high hardness and thermally stable nanocrystalline aluminium composites is described. Al powder was milled at room temperature in an ammonia flow for a period of less than 5 h. NH_3 dissociation during milling provokes the absorption, at a high rate, of nitrogen into aluminium, hardening it by forming a solid solution. Controlled amounts of AlN and $\text{Al}_5\text{O}_6\text{N}$ are formed during the subsequent sintering of milled powders for consolidation. The pinning action of these abundant dispersoids highly restrains aluminium grain growth during heating. The mean size of the Al grains remains below 45 nm and even after the milled powder is sintered at 650°C for 1 h.

1. Introduction

Nanostructured materials are promising materials that offer new opportunities for substantially improving the standard of living. Over the last years, nanostructured materials research has grown significantly [1–3]. Grain size reduction to the nanometre scale allows for improvements in mechanical properties, as has been shown by several researchers [4–8]. Currently, the most common processing methods for the production of nanocrystalline materials include inert gas condensation, chemical reaction methods, electrodeposition, severe plastic deformation, and mechanical milling [9, 10]. The latter, also called high-energy milling or mechanical alloying, is considered one of the main techniques in this regard [11, 12].

Al powder has traditionally been reinforced with a variety of micron-size directly added ceramic particles, such as alumina, silicon carbide, titanium carbide, and others [13–15]. Recently, Al-matrix composites reinforced with sub-micrometric (0.1–1 μm) and nanometric (<0.1 μm) particles have been widely studied [16, 17]. However, one of the main challenges towards achieving a homogeneous distribution of

a nanometric ceramic phase in a metal matrix is avoiding agglomeration of the reinforcement particles [18].

It has been found that the reinforcement of aluminium powders is more homogeneous when these dispersoids are formed through direct reaction of the aluminium with its environment, rather than by simply mixing aluminium with ceramic composites [19–22]. Aluminium easily reacts with elements such as C, O, N, and H, which leads to difficulties in its traditional processing, but this reactivity can be positively used through mechanical alloying to form, after thermal treatments, several phases finely dispersed in the matrix. These phases, such as aluminium oxide (Al_2O_3), carbide (Al_4C_3), nitride (AlN), oxynitrides, and oxycarbonitrides [19], perform as reinforcing instead of embrittling agents. In the presence of hydrogen, aluminium forms hydrides, which are brittle, but they are easily removed by heating, forming hydrogen, which is evacuated during sintering [23, 24].

On the other hand, aluminium nitride possesses excellent conductivity, low thermal expansion, high hardness, and good oxidation resistance at elevated temperatures [25]. These characteristics suggest that AlN may be an acceptable reinforcement not only for mechanical applications but also

for physical aims such as electronic applications, when the composite/substrate junction must have no significant distortions with thermal changes [26]. Several preparation methods of Al/AlN composite materials have been reported. Most of them are based on pressure or pressureless metal infiltration, spray deposition and hot pressing, squeeze casting, and mechanical alloying [27–31].

This paper describes a new and simple method to obtain aluminium-based nanostructured components reinforced by self-forming nanometric AlN. These reinforcements are formed through the mechanosynthesis of Al powders in an ammonia gas flow at room temperature for relatively short milling times (5 h), followed by a conventional powder metallurgy consolidation process.

2. Materials and Methods

The starting material was atomised elemental aluminium powder (ECKA AS 61, Eckart-Werke, Germany), with a purity higher than 99.7% and a mean particle size of 80.5 μm . Aluminium powder was milled in a high-energy attritor ball-mill (Union Process, USA). The water-cooled stainless steel vessel used has a 1400 cm^3 capacity. A 3 wt.% micropowder organic wax (etilen bis-stearamide) was used to control the welding and fracture processes of Al powder during milling. The mill charge contained 72 g of powder and 3600 g of balls (charge ratio in wt. %: 50 : 1). The milling processes were performed in an ammonia (NH_3) flow of 1 cm^3/s with a purity higher than 99.96%.

In order to study the evolution of the morphology and microstructure of the powders, milling was performed from 1 to 5 h with rotor speeds of 300 and 500 rpm. For comparison, a milling process in vacuum (5 Pa) at 500 rpm for 5 h was also performed. The powder particle sizes were measured by laser diffraction (Malvern, Mastersizer 2000), whereas the morphology was studied by a scanning electron microscope (SEM, Philips XL-30) equipped with an energy dispersive microanalysis system. To measure the powder compressibility, a universal testing machine (Instron, 5505) with a load cell of 100 kN was used.

The milled powders were consolidated by cold uniaxial pressing (1300 MPa) and vacuum (5 Pa) sintering (650°C for 1 h). X-ray diffraction measurements (XRD, Bruker D8 Advance, using $\text{CuK}\alpha$ radiation) and transmission electron microscopy (TEM, Phillips CM 200) of milled and sintered powders were used to identify, quantify, and measure the crystallite and grain size of the phases formed. Vickers hardness (Struers Duramin A300) of sintered compacts was evaluated using a load of 1 kg, whereas relative density was determined both by Archimedes' principle and by mass and dimensions measurement.

3. Results and Discussion

3.1. Granulometry. Figure 1 displays the granulometric distribution of the as-received aluminium (AR Al) and the mechanically alloyed powders, at 300 and 500 rpm, in an ammonia gas flow (MA A 300 and MA A 500, resp.).

The curve of the MA A 500 powders (Figure 1(b)) shows that, contrary to that expected for a ductile powder such as aluminium, the particle size decreases from its initial value (powder milled for 1 h, MA A 500-1). This is due to the rapid dissociation and adsorption of components of the ammonia from the beginning of the mechanical alloying process, strengthening the aluminium by solid solution. This strengthening associated with high-energy milling is responsible for the rapid particle size decrease. On the other hand, lack of symmetry is observed in the curves of the 3- and 5-h milled powders (MA A 500-3 and MA A 500-5). This could be related to the small particle size of these powders, which significantly promotes powder agglomeration.

In contrast, the lower energy of the process when milling at 300 rpm causes a slower particle size evolution (Figure 1(a)). The powder requires more time to harden, homogenise, and decrease in size. Therefore, the MA A 300 powders have a larger mean particle size (Figure 1(c)) and a broader particle size distribution as compared to the MA A 500 powders for the same milling time. Furthermore, the lower milling energy and the consequent increase of the particle welding processes are also responsible for the higher particle size observed after 1 h (MA A 300-1) as compared with the AR Al (Figure 1(c)).

3.2. Morphology. Figure 2 shows the sequence of SEM micrographs of MA A 300 powders as a function of milling time. For this rotor speed, powder morphological changes occur following the usual evolution [32]; after 1 h of milling, the powder particles have a flake shape (Figure 2(a)); after 2 h, they begin to weld to each other (Figure 2(b)); and after 3 h, they tend toward an elongated multilayer structure (Figure 2(c)), which is revealed when sections of powders are studied. With increasing milling time, it was found that the elongated multilayer particles evolve to equiaxed particles, markedly decreasing their size (Figure 2(d)).

In contrast, this morphological evolution is faster for samples obtained by milling at 500 rpm. As shown in Figure 3, the particles have a flake shape after 1 h of milling (Figure 3(a)) and acquire an equiaxial morphology after only 2 h (Figure 3(b)). By increasing the milling time, the particle size is further reduced, while its geometry tends to be more rounded (Figures 3(c) and 3(d)). It can be observed that the powder tends to agglomerate, causing the aforementioned lack of symmetry of the granulometric curves of powders milled for 3 h and 5 h (MA A 500-3 and MA A 500-5).

3.3. Compressibility Test. Due to the small size of the as-milled powder particles, it was not possible to measure their microhardness. Nevertheless, a compressibility test (measuring the relative green density versus the applied compaction pressure) is an indirect method for determining the inherent hardness of powder particles [19]. This curve is very useful for determining, during the powder consolidation process, the adequate compaction pressure, that is, the desired green density. Compressibility curves of the milled powders are shown in Figure 4. Curves for the AR Al and vacuum-milled

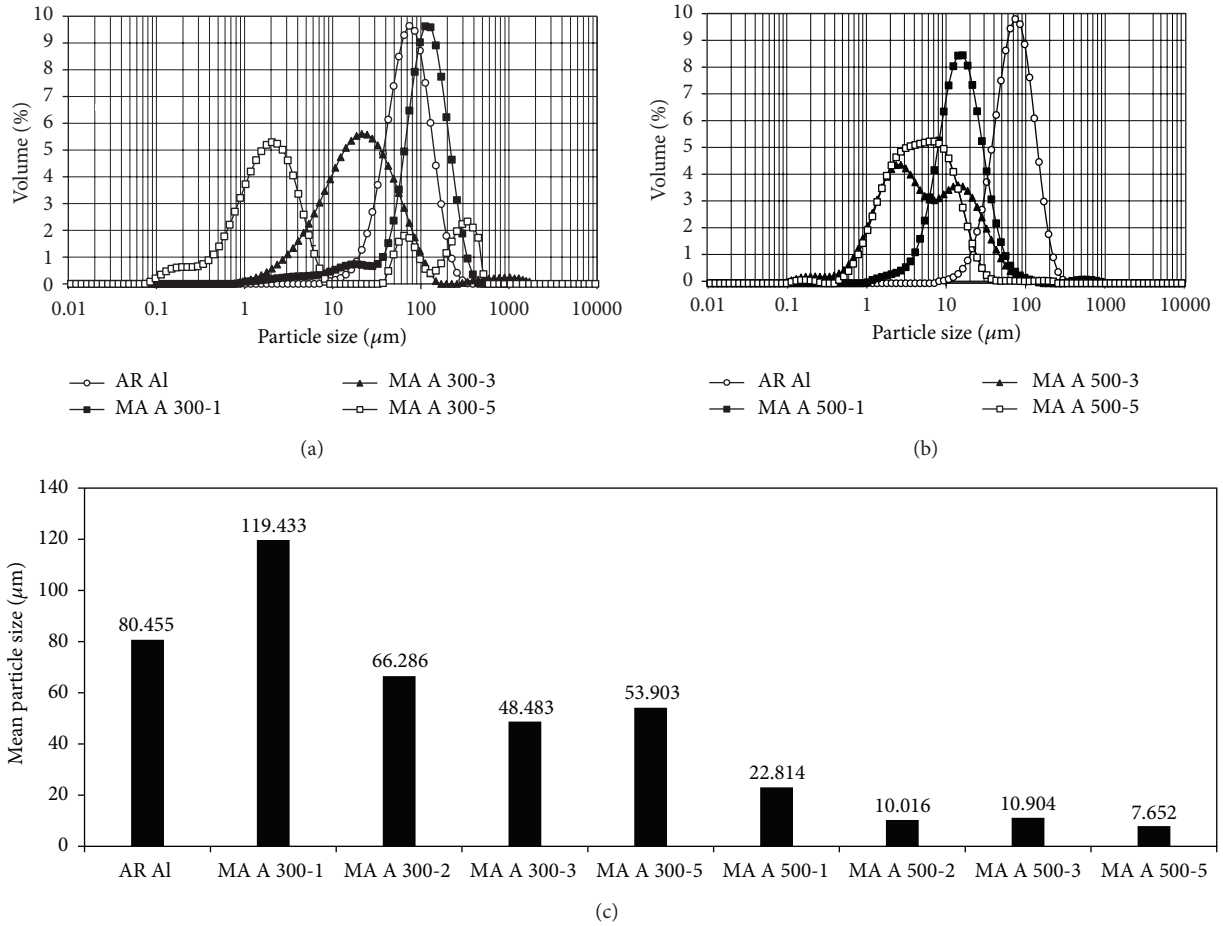


FIGURE 1: Granulometric curve of AR Al and powders milled in NH_3 flow at (a) 300 rpm and (b) 500 rpm for 1, 3, and 5 h and (c) mean particle size (D4,3) of these powders.

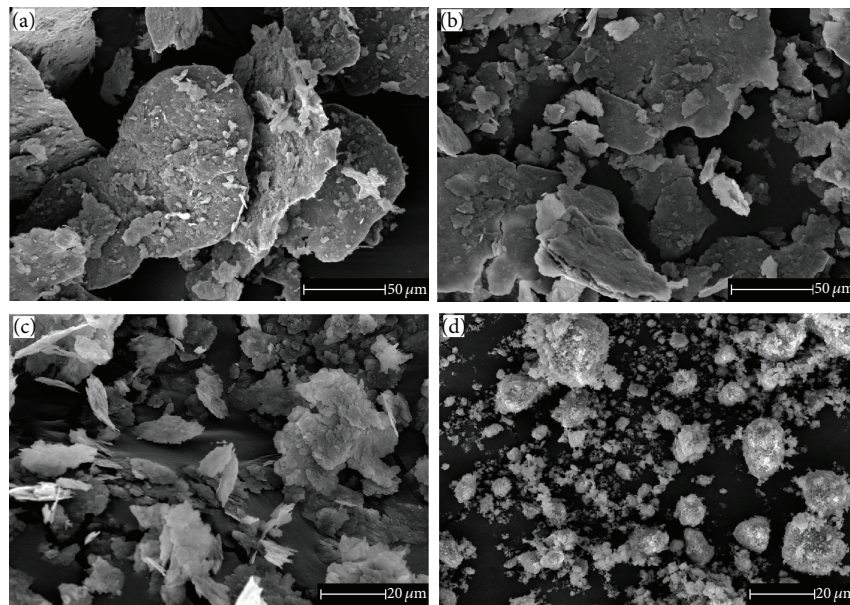


FIGURE 2: Morphological evolution of the milled powder in ammonia flow at 300 rpm for (a) 1 h, (b) 2 h, (c) 3 h, and (d) 5 h. Note the different magnification used.

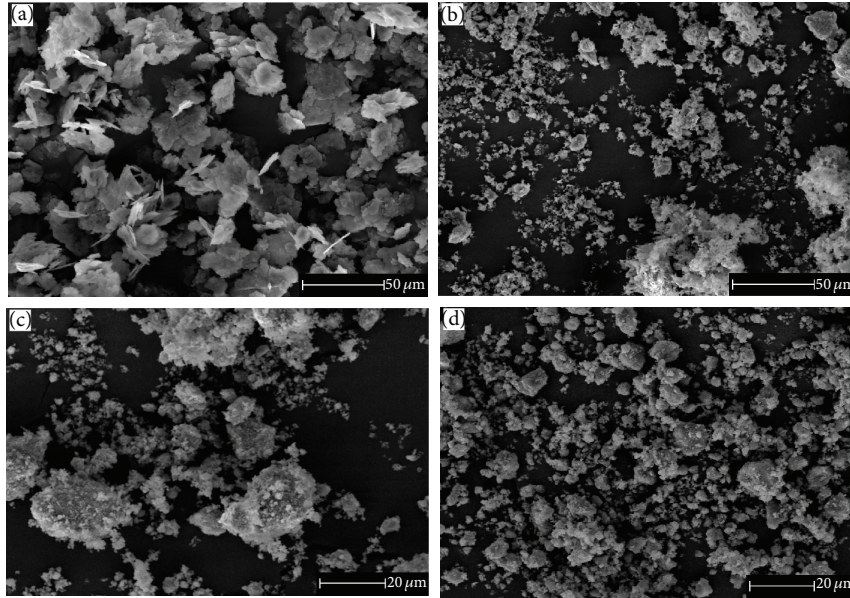


FIGURE 3: Morphologic evolution of powder milled in NH_3 flow at 500 rpm for (a) 1 h, (b) 2 h, (c) 3 h, and (d) 5 h. Note the different magnification used.

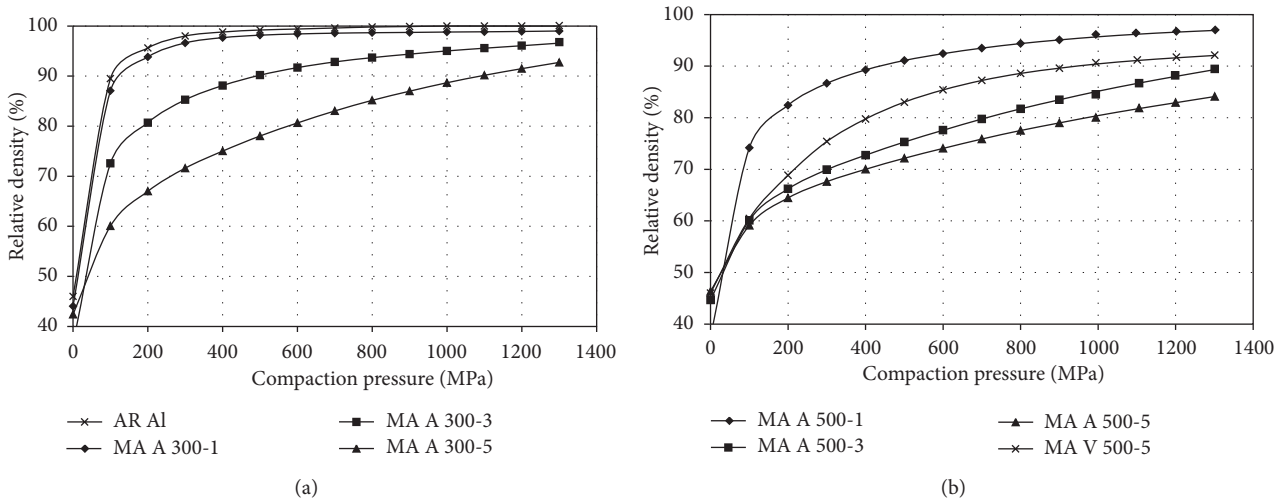


FIGURE 4: Compressibility curves of (a) AR Al and powders milled in ammonia at 300 rpm for 1, 3, and 5 h and (b) powders milled at 500 rpm in vacuum for 5 h and in ammonia for 1, 3, and 5 h.

powder at 500 rpm for 5 h (MA V 500-5) are also included for comparison.

The powder milled in ammonia at 300 rpm for 1 h (MA A 300-1) and pressed at 500 MPa has a relative density higher than 98% (Figure 4(a)), whereas the relative density of powder milled under the same conditions but for 5 h (MA A 300-5) is slightly higher than 78%. In contrast, the AR Al powder reaches a relative density close to 100% for the same compaction pressure. This shows that, even when using a rotor speed of only 300 rpm, the strain hardening effect is quite fast with respect to milling time.

At a pressure of 500 MPa, the powders milled at 500 rpm for 1 and 5 h (MA A 500-1 and MA A 500-5) reach relative densities above 90 and 70%, respectively (Figure 4(b)). These values are slightly lower in comparison with the powders milled at 300 rpm, because, as expected, the hardening effect increases with rotor speed. However, this increase is not only due to the milling energy. In ammonia flow milling, solid solution hardening has an additional effect on the strain hardening. This assertion can be verified by comparing (Figure 4(b)) the compressibility curves of MA A 500-5 and powder milled in vacuum at the same rotor speed for the same

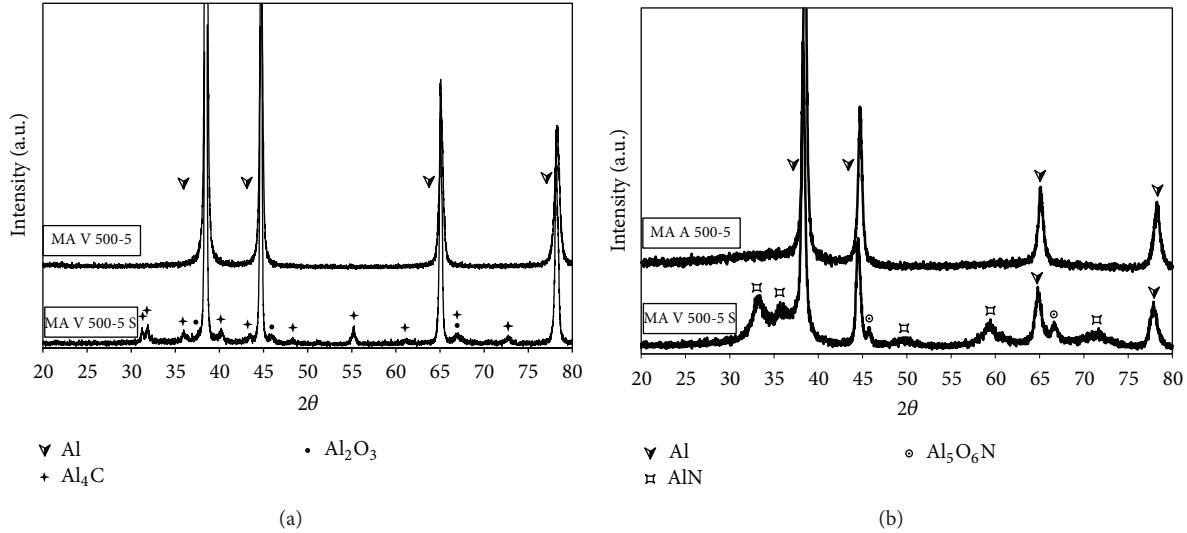


FIGURE 5: X-ray diffraction of as-milled and as-sintered Al powders milled for 5 h (a) in vacuum and (b) in ammonia gas flow.

TABLE 1: Phases present vol.% in sintered Al powders milled in an ammonia gas flow at 500 rpm for 1, 3, and 5 h (MA A 500-1 S, MA A 500-3 S, and MA A 500-5 S).

Phase	Material		
	MA A 500-1 S	MA A 500-3 S	MA A 500-5 S
Aluminium (Al)	78.45	46.41	28.87
Aluminium nitride (AlN)	6.22	20.25	49.58
Aluminium oxynitride (Al_5O_6N)	15.33	33.33	21.55

duration (MA V 500-5). Logically, the friction force caused by interlock behaviour between irregular-shape particles could increase the hardening effect.

3.4. Microstructure. The powders milled in vacuum at 500 rpm for 5 h before and after sintering (MA V 500-5 and MA V 500-5 S, resp.) were analysed by XRD to determine and quantify the phases formed (Figure 5(a)). The XRD patterns of the as-milled powders show only Al peaks. In contrast, in the sintered compact pattern, the presence of aluminium carbide (Al_4C_3) and small oxide ($\delta-Al_2O_3$) peaks is detected. The carbides form come from the etilen bis-stearamide wax ($H_{35}C_{17}CONHC_2H_4NHCOC_{17}H_{35}$) used as process controlling agent during milling, whereas the oxides mainly come from the powder particle surface.

The XRD patterns were fitted via Rietveld refinement [33], and the methods of Williamson-Hall [34] and Langford [35] were applied to calculate the crystallite size and to quantify the phases formed. These methods gave an as-milled Al crystallite size of 38 ± 1 nm, whereas after sintering, the crystallite size increased to 700 ± 9 nm. This grain growth during heating is exclusively controlled by the pinning effect of Al_4C_3 and Al_2O_3 , which were present at 8.98 and 0.61 vol.%, respectively.

Similar to the vacuum-milled powders, only Al peaks were observed in the XRD pattern (Figure 5(b)) of the powders milled, also for 5 h, in an ammonia flow (MA A 500-5), with a crystallite size of 16 ± 0.5 nm. However, the situation is

very different after sintering; nitrogen, in solid solution after milling, creates nanocrystalline aluminium nitride (AlN) and aluminium oxynitride (Al_5O_6N) (12 ± 0.5 and 4 ± 0.2 nm, resp., also calculated by XRD) during powder heating (Figure 5(b)). Thus, the proposed mechanosynthesis process can produce NH_3 dissociation at room temperature, whereas under normal conditions (without milling), this occurrence only happens at temperatures of approximately $550^\circ C$. This could be an advantage over other methods for preparing Al/AlN composites, which usually include complicated steps or are performed at very low or high temperatures [36–39]. As expected, the quantity of aluminium nitride and oxynitride depends on the milling time, as shown in the quantification results of Table 1. It is notable that, after 3 h and 5 h of milling at 500 rpm, 20.25 and 49.58 vol.% of AlN were, respectively, obtained, showing that the formation of AlN with this method is very effective, even for short milling times.

Even more interesting is the effect that these nanocrystalline dispersoids have on Al grain growth. After sintering, the Al crystallite size of powders milled 5 h in vacuum increased to 700 ± 9 nm, as measured on the XRD pattern, while it increased only to 45 ± 1 nm for powders milled in an ammonia gas flow for the same duration.

In order to check these sizes, consolidated compacts have been studied by TEM. Figure 6(a) shows a bright field image of a sintered compact prepared from 5 h vacuum-milled powders. Results by image analysis on micrographs of these

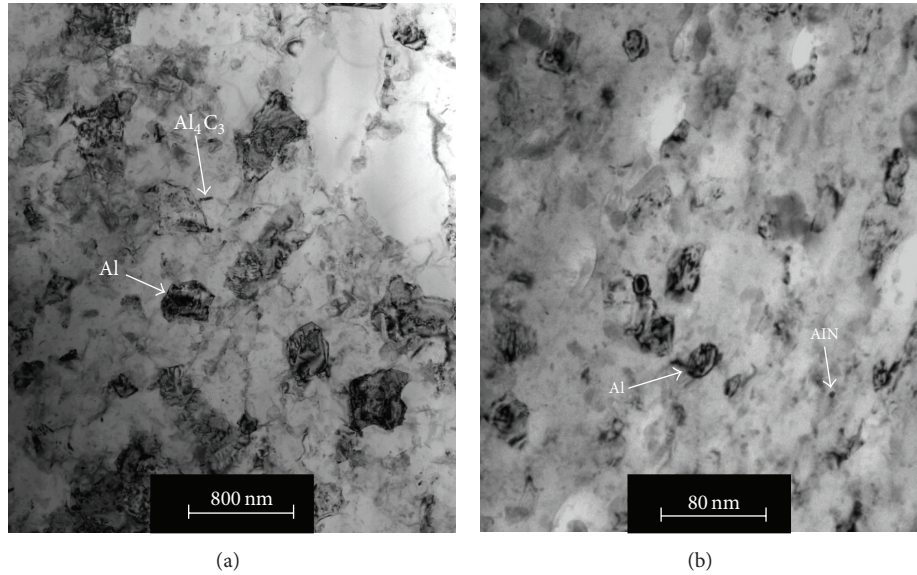


FIGURE 6: Bright-field TEM images of sintered compacts showing different phases formed in (a) MA V 500-5 S and (b) MA A 500-5 S.

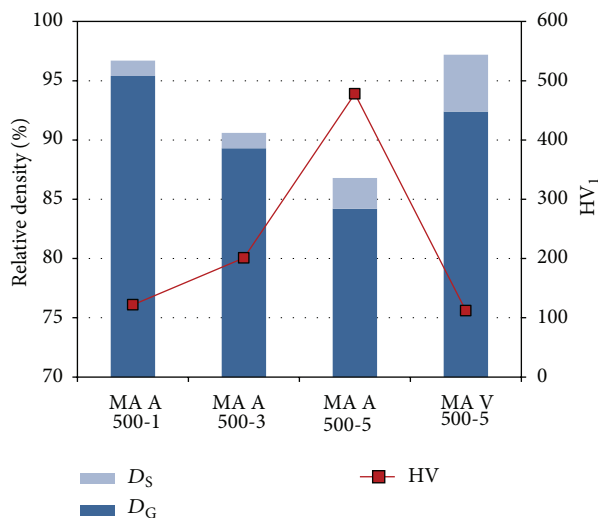


FIGURE 7: Green (D_G) and sintered (D_S) relative density and Vickers hardness of sintered compacts from powders milled at 500 rpm in vacuum for 5 h and in an ammonia flow for 1, 3, and 5 h.

specimens give an Al mean grain size of 709 ± 20 nm, resulting in 15 times that of Al grains in specimens prepared from powder milled under ammonia flow for 5 h (Figure 6(b)), which resulted to be only 43 ± 9 nm as obtained by image analysis from TEM images.

The aforementioned remarkable amount of dispersoids, together with the small Al grain size, surely increases the hardness of compacts processed from powders milled in an ammonia flow. However, this expected hardness could be reduced due to the difficulty in consolidating such hard powders.

Figure 7 shows the green (D_G) and sintered (D_S) relative densities of compacts prepared from powders milled in

an ammonia flow at 500 rpm. The values of MA V 500-5 are also included for comparison. The low hardness of the MA A 500-1 powders makes it possible to reach high green densities (95.4%); however, the flake shape and relatively large size of the particles make the sintering process difficult, increasing the density by only 1.3%. An increase in the milling time to 3 or 5 h makes the powders harder, avoiding high green densities after the pressing stage. Despite the high specific area of both powders, due to their small size, their low green density seems to be the reason, together with the lower sinterability of the refractory phases (now in a higher amount), that the sinterability level of these samples is constrained (Figure 7). Improvements in the relative densities of the final products are currently under study in the authors' laboratory, using additives such as copper to promote liquid phase sintering.

The nanosized Al grains and the presence of hard phases dispersed in the compacts prepared from ammonia-milled powders make their hardness be, despite their relatively elevated porosities, higher than those achieved in compacts prepared from vacuum-milled powders (Figure 7). It is remarkable that hardness of $478 HV_1$ was achieved in sintered compacts of powders milled for 5 h in NH_3 .

4. Conclusions

Aluminium powder was attrition-milled in an ammonia flow of $1 \text{ cm}^3/\text{s}$ for 1 to 5 h, with rotor speeds of 300 and 500 rpm. The following conclusions are drawn.

- (1) A simple method at room temperature has been developed to produce bulk aluminium-based nanocomposites reinforced with in situ generated aluminium nitride and oxynitride nanodispersoids.
- (2) During milling, the ammonia is decomposed, and high quantities of nitrogen are incorporated into the

Al powder, hardening it by solid solution. Thus, it is possible to obtain small and hard equiaxial particles after only 2 h of milling.

- (3) The milled powders, both in vacuum or in NH_3 gas flow, only show the presence of aluminium with a crystallite size of approximately 38 ± 1 and 16 ± 0.5 nm, respectively. After heating, aluminium nitride (AlN) and oxynitride ($\text{Al}_5\text{O}_6\text{N}$) are formed in the ammonia-flow-milled powders, whereas in the vacuum-milled powders, only aluminium oxide (Al_2O_3) and carbide (Al_4C_3) appear.
- (4) The ammonia-flow-milled powders have a high quantity of AlN (up to 49.58 vol.%) and $\text{Al}_5\text{O}_6\text{N}$ nanometric dispersoids, with crystallite sizes below 12 ± 0.5 nm. Thus, these phases highly restrict aluminium grain growth during sintering, keeping it below 45 ± 1 nm (MA A 500-5 S).
- (5) The final compacts produced with these ammonia-flow-milled powders exhibit high hardness (up to 478 HV_1), despite their low relative density values.

Conflict of Interests

The authors declare that there is no conflict of interests regarding the publication of this paper.

Acknowledgments

Financial support of the Ministerio de Ciencia e Innovación, Spain, through the research Projects DPI2012-37948-C02-01 and DPI2009-08291 is gratefully acknowledged. The authors also wish to thank the technicians J. Pinto, M. Madrid and M. Sánchez (University of Seville, Spain) for the experimental assistance.

References

- [1] C. Joachim, "To be nano or not to be nano?" *Nature Materials*, vol. 4, pp. 107–109, 2005.
- [2] T. G. Langdon, "The impact of bulk nanostructured materials in modern research," *Reviews on advanced materials science*, vol. 25, no. 1, pp. 11–15, 2010.
- [3] R. Z. Valiev, M. J. Zehetbauer, Y. Estrin et al., "The innovation potential of bulk nanostructured materials," *Advanced Engineering Materials*, vol. 9, no. 7, pp. 527–533, 2007.
- [4] H. Gleiter, "Nanocrystalline materials," *Progress in Materials Science*, vol. 33, no. 4, pp. 223–315, 1989.
- [5] R. Valiev, "Nanostructuring of metals by severe plastic deformation for advanced properties," *Nature Materials*, vol. 3, pp. 511–516, 2004.
- [6] W. H. Hunt Jr., "Nanomaterials: nomenclature, novelty, and necessity," *JOM*, vol. 56, no. 10, pp. 13–18, 2004.
- [7] H. Gleiter, "Nanostructured materials: state of the art and perspectives," *Nanostructured Materials*, vol. 6, no. 1–4, pp. 3–14, 1995.
- [8] A. P. Newbery, B. Ahn, T. D. Topping, P. S. Pao, S. R. Nutt, and E. J. Lavernia, "Large UFG Al alloy plates from cryomilling," *Journal of Materials Processing Technology*, vol. 203, no. 1–3, pp. 37–45, 2008.
- [9] A. S. Khan, B. Farrokh, and L. Takacs, "Effect of grain refinement on mechanical properties of ball-milled bulk aluminum," *Materials Science and Engineering A*, vol. 489, no. 1–2, pp. 77–84, 2008.
- [10] C. C. Koch, "Structural nanocrystalline materials: an overview," *Journal of Materials Science*, vol. 42, no. 5, pp. 1403–1414, 2007.
- [11] C. Suryanarayana, "The structure and properties of nanocrystalline materials: issues and concerns," *JOM*, vol. 54, no. 9, pp. 24–27, 2002.
- [12] D. L. Zhang, "Processing of advanced materials using high-energy mechanical milling," *Progress in Materials Science*, vol. 49, no. 3–4, pp. 537–560, 2004.
- [13] Z. R. Hesabi, S. Kamrani, A. Simchi, and S. M. S. Reihani, "Effect of nanoscaled reinforcement particles on the structural evolution of aluminium powder during mechanical milling," *Powder Metallurgy*, vol. 52, no. 2, pp. 151–157, 2009.
- [14] J. Ye, B. Q. Han, Z. Lee, B. Ahn, S. R. Nutt, and J. M. Schoenung, "A tri-modal aluminum based composite with super-high strength," *Scripta Materialia*, vol. 53, no. 5, pp. 481–486, 2005.
- [15] H. Mohseni, S. Keirs, S. L. I. Chan, and M. Ferry, "High temperature stability of fine grained 7075Al alloy containing nanosized SiC particles," *Materials Science and Technology*, vol. 26, no. 5, pp. 597–603, 2010.
- [16] Z. Z. Chen and K. Tokaji, "Effects of particle size on fatigue crack initiation and small crack growth in SiC particulate-reinforced aluminium alloy composites," *Materials Letters*, vol. 58, no. 17–18, pp. 2314–2321, 2004.
- [17] C. F. Chen, P. W. Kao, L. Chang, and N. J. Ho, "Mechanical properties of nanometric Al_2O_3 particulate-reinforced Al– $\text{Al}_{11}\text{Ce}_3$ composites produced by friction stir processing," *Materials Transactions*, vol. 51, pp. 933–938, 2010.
- [18] B. Prabhu, C. Suryanarayana, L. An, and R. Vaidyanathan, "Synthesis and characterization of high volume fraction Al– Al_2O_3 nanocomposite powders by high-energy milling," *Materials Science and Engineering A*, vol. 425, no. 1–2, pp. 192–200, 2006.
- [19] J. Cintas, F. G. Cuevas, J. M. Montes, and E. J. Herrera, "High-strength PM aluminium by milling in ammonia gas and sintering," *Scripta Materialia*, vol. 53, no. 10, pp. 1165–1170, 2005.
- [20] J. Cintas, F. G. Cuevas, J. M. Montes, and E. J. Herrera, "Microstructural control of sintered mechanically alloyed Al–1%Ni material," *Scripta Materialia*, vol. 52, no. 5, pp. 341–345, 2005.
- [21] F. G. Cuevas, J. Cintas, J. M. Montes, and J. M. Gallardo, "Al–Ti powder produced through mechanical alloying for different times," *Journal of Materials Science*, vol. 41, no. 24, pp. 8339–8346, 2006.
- [22] J. Cintas, F. G. Cuevas, J. M. Montes, E. S. Caballero, and E. J. Herrera, "Strengthening of ultrafine PM aluminium using nano-sized oxycarbonitride dispersoids," *Materials Science and Engineering A*, vol. 528, no. 28, pp. 8286–8291, 2011.
- [23] J. Cintas, J. M. Montes, F. G. Cuevas, and E. J. Herrera, "Heat-resistant bulk nanostructured P/M aluminium," *Journal of Alloys and Compounds*, vol. 458, no. 1–2, pp. 282–285, 2008.
- [24] J. Cintas, J. A. Rodríguez, J. M. Gallardo, and E. J. Herrera, "The impact of bulk nanostructured materials in modern research," *Revista de Metalurgia*, vol. 37, no. 2, pp. 370–375, 2001.

- [25] P. G. Zhang, K. Y. Wang, and S. M. Guo, "Large-scale synthesis of AlN nanofibers by direct nitridation of aluminum," *Ceramics International*, vol. 36, no. 7, pp. 2209–2213, 2010.
- [26] Z. Liu, B. Wu, and M. Gu, "An investigation of micro-galvanic corrosion in Al/AlN_p composites," *Materials Chemistry and Physics*, vol. 102, no. 1, pp. 43–46, 2007.
- [27] H. Yu, H. Chen, R. Ma, and G. Min, "Fabrication of AlN-TiC/Al composites by gas injection processing," *Rare Metals*, vol. 25, no. 6, pp. 659–664, 2006.
- [28] S. W. Lai and D. D. L. Chung, "Fabrication of particulate aluminium-matrix composites by liquid metal infiltration," *Journal of Materials Science*, vol. 29, no. 12, pp. 3128–3150, 1994.
- [29] A. Inoue, K. Nosaki, B. G. Kim, T. Yamaguchi, and T. Masumoto, "Mechanical strength of ultra-fine Al-AlN composites produced by a combined method of plasma-alloy reaction, spray deposition and hot pressing," *Journal of Materials Science*, vol. 28, no. 16, pp. 4398–4404, 1993.
- [30] D. F. Lii, J. L. Huang, and S. T. Chang, "The mechanical properties of AlN/Al composites manufactured by squeeze casting," *Journal of the European Ceramic Society*, vol. 22, no. 2, pp. 253–261, 2002.
- [31] H. Abdoli, E. Salahi, H. Farnoush, and K. Pourazrang, "Evolution during synthesis of Al-AlN-nanostructured composite powder by mechanical alloying," *Journal of Alloys and Compounds*, vol. 461, no. 1-2, pp. 166–172, 2008.
- [32] J. Cintas, J. M. Montes, F. G. Cuevas, and J. M. Gallardo, "Influence of PCA content on mechanical properties of sintered MA aluminium," *Materials Science Forum*, vol. 514-516, no. 2, pp. 1279–1283, 2006.
- [33] R. A. Young, Ed., *The Rietveld Method*, Oxford University Press, New York, NY, USA, 2000.
- [34] G. K. Williamson and W. H. Hall, "An abnormal after-effect in metals," *Acta Metallurgica*, vol. 1, no. 1, pp. 2–31, 1953.
- [35] J. I. Langford, "A rapid method for analysing the breadths of diffraction and spectral lines using the Voigt function," *Journal of Applied Crystallography*, vol. 11, pp. 10–14, 1978.
- [36] Y. Q. Liu, H. T. Cong, W. Wang, C. H. Sun, and H. M. Cheng, "AlN nanoparticle-reinforced nanocrystalline Al matrix composites: fabrication and mechanical properties," *Materials Science and Engineering A*, vol. 505, pp. 151–156, 2009.
- [37] Y. Li, Y. H. Zhao, V. Ortalan et al., "Investigation of aluminum-based nanocomposites with ultra-high strength," *Materials Science and Engineering A*, vol. 527, no. 1-2, pp. 305–316, 2009.
- [38] K. B. Lee, H. S. Sim, and H. Kwon, "Fabrication of Al/AlN composites by in situ reaction," *Journal of Materials Science*, vol. 41, no. 19, pp. 6347–6352, 2006.
- [39] J. Shengli, L. Yawei, L. Jing et al., "Microstructure and phase composition of AlN/Al composite fabricated by directed melt nitridation," *Key Engineering Materials*, vol. 368-372, no. 2, pp. 977–979, 2008.

Research Article

Size Controlled Synthesis of FeCo Alloy Nanoparticles and Study of the Particle Size and Distribution Effects on Magnetic Properties

A. Shokuhfar¹ and S. S. S. Afghahi^{1,2}

¹ Advanced Materials and Nanotechnology Research Laboratory, Faculty of Materials Science and Engineering, K.N. Toosi University of Technology, P.O. Box: 19395-1999 Tehran, Iran

² Nanotechnology Research Center, Imam Hossein University, 1581618711 Tehran, Iran

Correspondence should be addressed to S. S. S. Afghahi; salmanafghahi@gmail.com

Received 8 October 2013; Revised 30 December 2013; Accepted 6 January 2014; Published 24 February 2014

Academic Editor: Luís Cunha

Copyright © 2014 A. Shokuhfar and S. S. S. Afghahi. This is an open access article distributed under the Creative Commons Attribution License, which permits unrestricted use, distribution, and reproduction in any medium, provided the original work is properly cited.

In this research the size controlled synthesis of FeCo nanoparticles was done using a quaternary microemulsion system. X-ray diffraction and high resolution transmission electron microscopy of as-synthesized nanoparticles confirm the formation of FeCo alloy nanoparticles. The effects of two process parameters, namely, water to surfactant molar ratio and molar concentration of metal salts, on the size and size distribution of nanoparticles were discussed by the aid of transmission electron microscopy. The size dependency of magnetic properties was also investigated using a room temperature vibrating sample magnetometer. The superparamagnetic-ferromagnetic and single domain-multidomain transition sizes were determined. Then the specific absorption rates at transition sizes were calculated and the best sample for magnetic hyperthermia treatment was introduced.

1. Introduction

Magnetic nanoparticles are a topic of growing interest because of their versatile applications such as ultrahigh density data storage, drug delivery, magnetic separation and MRI contrast enhancement [1–13]. Among those, magnetic hyperthermia is a novel therapeutic method in which the magnetic nanoparticles are subjected to an alternating magnetic field to generate a specific amount of heat. The generated heat will then raise the temperature of the tumor to about 42°C at which certain mechanisms of cell damage are activated [14]. The heat producing mechanisms under A.C. magnetic fields are (1) hysteresis, (2) the Neel or Brownian relaxation, (3) viscous losses [15].

The generated heat is quantitatively described by the specific absorption rate (SAR) of nanoparticles which is related to specific loss per cycle of hysteresis loop (A) by the equation $SAR = A \times f$ where f is the frequency of applied field.

Up to now several models have been proposed to predict the behavior of magnetic nanoparticles under alternating magnetic fields [16]. For superparamagnetic nanoparticles the equilibrium functions are used. The Langevin function $L(\xi) = \coth(\xi) - 1/\xi$ which is valid at zero anisotropy is an example of equilibrium functions where $\xi = (\mu_0 M_s V H_{\max}) / (k_B T)$ in which $\mu_0 H_{\max}$ is the external applied field, M_s is the spontaneous magnetization of the nanoparticle, V is the volume of nanoparticle, k_B is the Boltzmann constant, and T is the temperature. Linear response theory is valid for nanoparticles at superparamagnetic transition size. Based on this theory the area of the hysteresis loop is calculated by [16]

$$A = \frac{\pi \mu_0^2 H_{\max}^2 M_s^2 V}{3 k_B T} \frac{\omega \tau_R}{(1 + \omega^2 \tau_R^2)}, \quad (1)$$

where M_s is the saturation magnetization, $\omega = 2\pi f$, $\tau_R = \tau_N = \tau_0 \exp(K_{\text{eff}} V / (k_B T))$ is the relaxation time of

magnetization equal to the Neel relaxation time (τ_N), and τ_0 is the intrawell relaxation time. The Stoner-Wohlfarth model predicts the magnetic response for single domain ferromagnetic nanoparticles. This model neglects thermal activation and assumes a square hysteresis loop which is relevant for $T = 0$ or $f \rightarrow \infty$. For magnetic nanoparticles with their easy axes randomly oriented in space the hysteresis area is calculated by [16]:

$$A = 2\mu_0 H_c M_s = 1.92 K_{\text{eff}}, \quad (2)$$

where $\mu_0 H_c$ is the coercive field and K_{eff} is the effective uniaxial anisotropy of the nanoparticle. The key factor to obtain the maximum SAR in the conventional clinical hyperthermia treatments ($f = 100$ kHz, $\mu_0 H_{\text{max}} = 20$ mT, and $T = 300$ K) is the anisotropy of nanoparticles.

Calculations of SAR as a function of anisotropy in the above-mentioned size regimes reveal that the maximal SAR would be obtained at single domain-multidomain transition size. So producing nanoparticles in this range for use in hyperthermia treatment is of high value from technical and clinical aspects.

FeCo alloy has the highest saturation magnetization among all binary magnetic alloys [1]. Several methods have been used to synthesize FeCo alloy nanoparticles which include arc discharge [2], polyol [3–7], hydrothermal [8], reaction under autogenic pressure at elevated temperature (RAPET) [9], thermal decomposition [10], wet chemical [11, 12], and coprecipitation [13, 17, 18]. The morphology and size distribution of as-synthesized nanoparticles are not well controlled in most of these processes. To obtain the best properties for magnetic hyperthermia treatments the size distribution is an effective parameter. Researches show the loss of SAR due to nanoparticle size distributions. So employing a method capable of producing monodisperse nanoparticles is of high value.

Microemulsion technique is a method capable of controlling the shape, size, and size distribution of nanoparticles [19]. In this process nanoparticles precipitate inside micelles. The micelle is in the form of sphere of oil in water (normal micelle) or water in oil (reverse micelle) which is surrounded by a layer of surfactant molecules [20]. The technique could be used to synthesize mineral [21] or organic compounds [22].

There are few works on the synthesis of FeCo alloy nanoparticles. The novel quaternary system of water/cetyltrimethylammonium bromide (CTAB)/1-butanol/isooctane was employed for synthesis of FeCo alloy nanoparticles which has not been used before. Unlike other synthetic methods the proposed route is capable of controlling the size of nanoparticles in the range of 1–10 nm. This is achieved by controlling the water to surfactant molar ratio (R) and molar concentration of metal salts. This capability is of vital importance for investigating the heating effect of magnetic nanoparticles under A.C. magnetic fields.

In the present research, the shape and size controlled synthesis of iron cobalt alloy nanoparticles was carried out in the reverse micelles of water in isooctane and the magnetic properties of as-synthesized nanoparticles were

studied to investigate their potential usefulness in magnetic hyperthermia treatment.

2. Materials and Methods

Iron (III) chloride hexahydrate ($\text{FeCl}_3 \cdot 6\text{H}_2\text{O}$ (%99+)), isooctane, 1-butanol, sodium borohydride (NaBH_4 (%99+)), and cetyltrimethylammonium bromide (CTAB) were purchased from MERCK chemicals and used as received with no further purification. Cobalt acetate tetrahydrate ($\text{Co}(\text{CH}_3\text{COO})_2 \cdot 4\text{H}_2\text{O}$ (%99+)) was supplied by MP Bio-medicals. High purity nitrogen gas (%99.99+) was used to provide an oxygen-free environment during the synthesis procedure.

The key to formation of a microemulsion is the formation of a transparent and thermodynamically stable solution which forms at certain ratios of aqueous phase/surfactant/oil phase. Microemulsion 1 (ME1) and microemulsion 2 (ME2) were prepared on the basis of quaternary phase diagram of water/CTAB/1-butanol/isooctane which is described elsewhere [23].

$\text{Fe}_{0.65}\text{Co}_{0.35}$ alloy nanoparticles were prepared by mixing equal volumes of ME1 and ME2 containing metal salts and precipitating agent, respectively. The $[\text{NaBH}_4]/[\text{metal salts}]$ molar ratio was kept at 2 to ensure that all of precursors are reduced to zerovalent metal. First ME1 was transferred into a three-necked round bottom flask and then ME2 was added using a dropping funnel to vigorous stirring ME1 under N_2 atmosphere. Black precipitates of FeCo alloy nanoparticles appeared immediately after mixing of the two microemulsions.

After 10 minutes of reaction the solution was centrifuged and washed with chloroform, ethanol, and acetone several times to remove all residual elements. Some of as-synthesized powders were annealed in a tube furnace at 350°C and 550°C for 20 minutes under H_2 atmosphere.

Characterization of samples was done using X-ray diffraction (XRD) (PANalytical X'Pert Pro MPD with $\text{Cu } k_{\alpha}$ -radiation), scanning transmission electron microscope (STEM) (ZEISS EM10-C at 100 KV), and high resolution transmission electron microscope (HRTEM) (JEOL JEM-2100 at 200 KV). Elemental analysis was done using an energy dispersive X-ray spectroscopy (EDS) detector attached to the HRTEM. The magnetic properties of samples were analyzed using a room temperature (300 K) vibrating sample magnetometer. The samples and process conditions are summarized in Table 1.

3. Results and Discussion

3.1. Microstructural Characterization. Figure 1 shows XRD patterns for as-synthesized W3 and annealed samples. As seen from Figure 1(a) there is no major peak. Nanoparticle approximate size could be derived from the Scherrer formula ($d = 0.94\lambda/(\beta \cos \theta)$) based on the $\text{Cu } k_{\alpha}$ radiation and the FWHM of the peak. But for very small sizes (<5 nm) by considering the drastic peak widening and intensity decreasing there would not be any distinguishable peak. Also

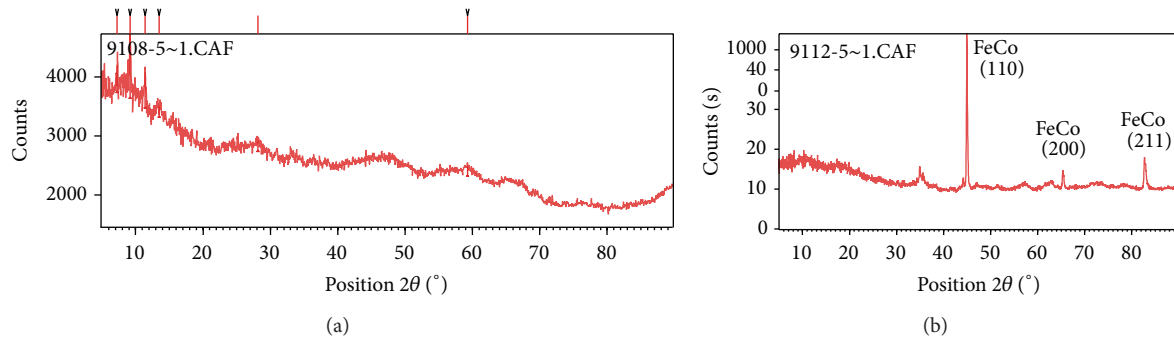


FIGURE 1: XRD patterns of W3 sample in (a) as synthesized state and (b) annealed at 550°C for 20 minutes.

TABLE 1: Samples and process conditions.

Sample	Water/surfactant molar ratio (R)	Molar concentration of metal salts
W1	6	1M
W2	8	1M
W3	12	1M
W4	37	1M
M1	12	0.5 M
M2	12	1.5 M
M3	12	2 M

the bad crystallinity of nanoparticles (Figure 2(b)) as a result of fast borohydride reduction fortifies this problem.

Figure 1(b) shows the diffraction pattern of W3 sample after annealing at 550°C for 20 minutes under H_2 atmosphere. XRD patterns reveal the formation of α -bcc structured FeCo alloy (at $2\theta = 44.83^\circ$, 65.32° and 84°). These values agree with JCPDS file for FeCo. Also a small quantity of $CoFe_2O_4$ (at $2\theta = 35.4^\circ$, 62.4°) is observed due to partial oxidation of the sample by exposing to air after annealing procedure. It has been found that FeCo is a substitutional alloy with a bcc structure from pure Fe to about 80 at. % Co and fcc for 90 at. % Co [18]. This agrees well with our result.

Figure 2 shows conventional (Figure 2(a)) and high resolution (Figure 2(b)) TEM images of W3 sample. Electron diffraction pattern (inset of Figure 2(a)) and HRTEM image also confirm the formation of bcc structured iron cobalt alloy. EDS analysis shows Fe and Co peaks in which the Fe peak is sharper than that of Co indicating higher content of Fe. Cl peak is from the residual chloroform which was used to wash as-synthesized nanoparticles. Also an oxygen peak is observed due to the partial oxidation of FeCo.

Figure 3 shows the effect of water to surfactant molar ratio (R) on the morphology, size and size distribution of as-synthesized nanoparticles. The mean size, and size distribution of each specimen were determined by inspecting about 50 TEM micrographs. It is evident that all samples have spherical shape due to the nature of the used surfactant and cosurfactant. Cetyltrimethylammonium bromide (CTAB) which has been used by Schulman for the first time (Hoar and Schulman, 1943) has a hydrophilic head

and a lipophilic tail which makes it soluble in both polar and nonpolar solvents. In this quaternary system the polar cosurfactant (1-butanol) makes ion-dipole interaction with the surfactant and forms spherical aggregates in which the polar (ionic) ends of the surfactant molecules are oriented towards the center. We observed that without the addition of 1-butanol the transparent microemulsion would not form. In fact the role of 1-butanol is to act as an electronegative spacer which minimizes the repulsive forces between polar heads of CTAB molecules and lets them be aggregated in the form of spherical micelles.

3.2. Effect of Water to Surfactant Molar Ratio. Figure 3 indicates the increasing of the mean size of nanoparticles with R . As the R value decreases, the relative amount of water reduces and a smaller micelle would be obtained. Therefore the limiting stability of nanoreactors increases leading to smaller nanoparticles. Also it was observed that the spherical shape of nanoparticles would not be affected by changing the R value unlike surfactants like polyvinylpyrrolidone (PVP) [24].

The W series of samples evidences very narrow (about 3 nm) size distribution which is related to the nature of the surfactant. In fact the surfactant has a double influence on the particle formation process: (1) particle stabilization and (2) growth control. The R value affects the former by determining the micellar core size, but the latter is influenced by the nature of the surfactant. The growth mechanism in microemulsions is based on intermicellar exchange [25]. A rigid surfactant surface layer tends to resist opening, thus the reaction is slowed down and simultaneous nucleation and growth occur. This in turn results in the formation of large nanoparticles with broad size distribution. But CTAB provides a very flexible film [25] which facilitates the coalescence exchange between micellar cores. The high exchange rate leads to a uniform nucleation and growth resulting in a narrow size distribution. As noted by Carrey et al., a broad size distribution decreases the maximum achievable SAR [16]. Therefore for as-synthesized FeCo nanoparticles the negative effect of a broad size distribution is not expected.

3.3. Effect of Molar Concentration of Metal Precursors. Figure 4 demonstrates the effect of molar concentration of

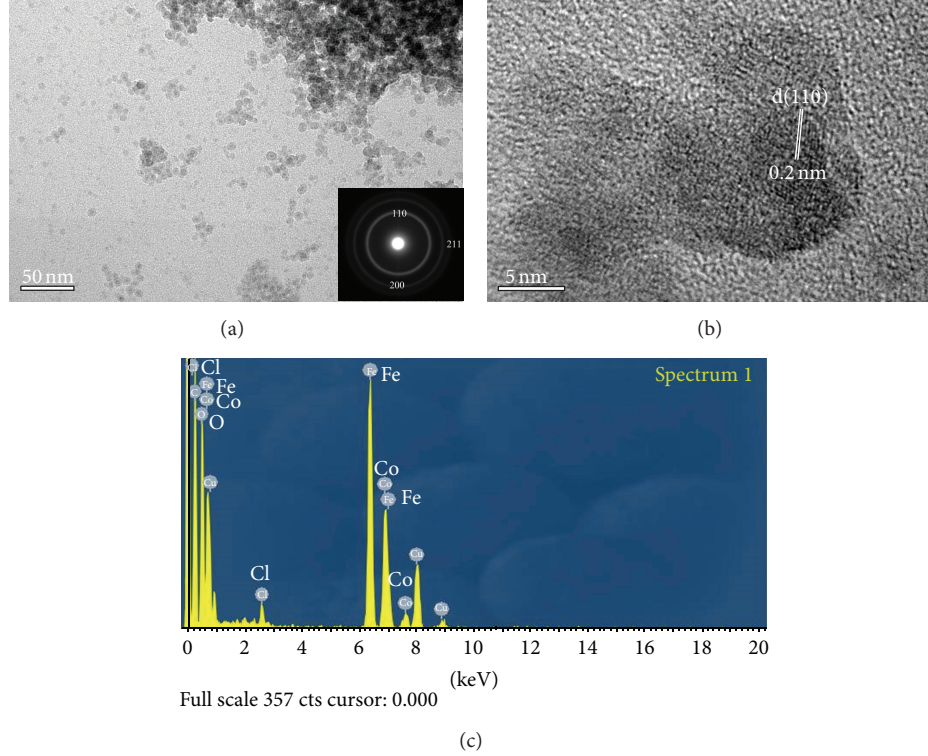


FIGURE 2: (a) TEM micrograph of W3 sample (inset: selected area diffraction pattern). (b) High resolution TEM image of W3 sample. (c) EDS spectra of W3 sample showing Fe, Co, Cl, and O peaks.

metal salts on the size and size distribution of nanoparticles. It is evident that increasing the molar concentration of metal precursors inversely affects the nanoparticle size. Since the borohydride reduction of metal precursors is almost instantaneous, a huge number of nuclei will form at the first stage of process followed by the nanoparticle growth via intermicellar exchange. Since at high concentrations of metal salts the supersaturation factor $\lambda(t)$ is higher, according to the Adamson equation for homogeneous nucleation, the nucleation rate is higher [26]:

$$k_n(i, t) = \begin{cases} 0, & i < n^*, \\ ik_0 \exp\left(\frac{-16\pi\sigma^2 v_m^2}{3(k_b T)^2 (\ln \lambda(t))^2}\right), & i \geq n^*, \end{cases} \quad (3)$$

where σ is the interfacial tension between solid nucleus and surrounding drop liquid, v_m is the volume of one precipitate molecule, λ is the supersaturation ratio of liquid product molecules, and n^* is the critical number of liquid product molecules in a nucleus. Thus at higher concentrations of metal precursors the number of stable nuclei is higher and consequently the number of remaining product molecules is smaller. Therefore the growth of nanoparticles which proceeds by the addition of product molecules is slowed down and the terminal nanoparticle size reduces. Similarly at lower concentrations of metal precursors the number of formed nuclei is lower providing more product molecules to contribute in the growth stage leading to larger terminal nanoparticles.

3.4. Magnetic Studies. Magnetization curves for W and M series of samples are outlined in Figures 5(a) and 5(b). M_s and H_c values are seen to be size dependent. As for W1 sample with mean size of 2 nm, the M_s equals 8 (emu/g). For W2, W3, and W4 (with mean sizes of 2.5 nm, 4 nm, and 9 nm) the M_s values reach 22, 36 and 65 (emu/g) respectively. This is also observed for M1, M2, and M3 with sizes of 6 nm, 3 nm, and 1.5 nm, and corresponding M_s of 49, 23, and 6 (emu/g). Also as expected some of the particles (W1, W2, M1, and M2) show superparamagnetic behavior with zero coercivity. In ferromagnetic metals like Fe, Co, and Ni the exchange interaction is positive, favoring the parallel alignment of spins. But when the particle size decreases, the majority of atoms and consequently spins are located at the nanoparticle surface. Regardless of the lower spin density at the surface, the structural changes at the surface should be considered. It is proved that the average lattice parameter in nanoparticles is less than their corresponding bulk materials mainly due to the bond length reduction [27].

This bond length contraction induces the overlapping of atomic orbitals, which reduces the atomic dipole moment. Also due to the lower coordination number for surface atoms the exchange coupling between dipoles is less than internal atoms and therefore the magnetic moments tend to fluctuate. The sum of these effects disorder spins at the surface to form a magnetic dead layer. The effect of this layer is reducing the total magnetic moment of nanoparticle [28]. This event is important mainly at sizes below 5 nm in which about %50 of total atoms are located at the surface. By increasing the

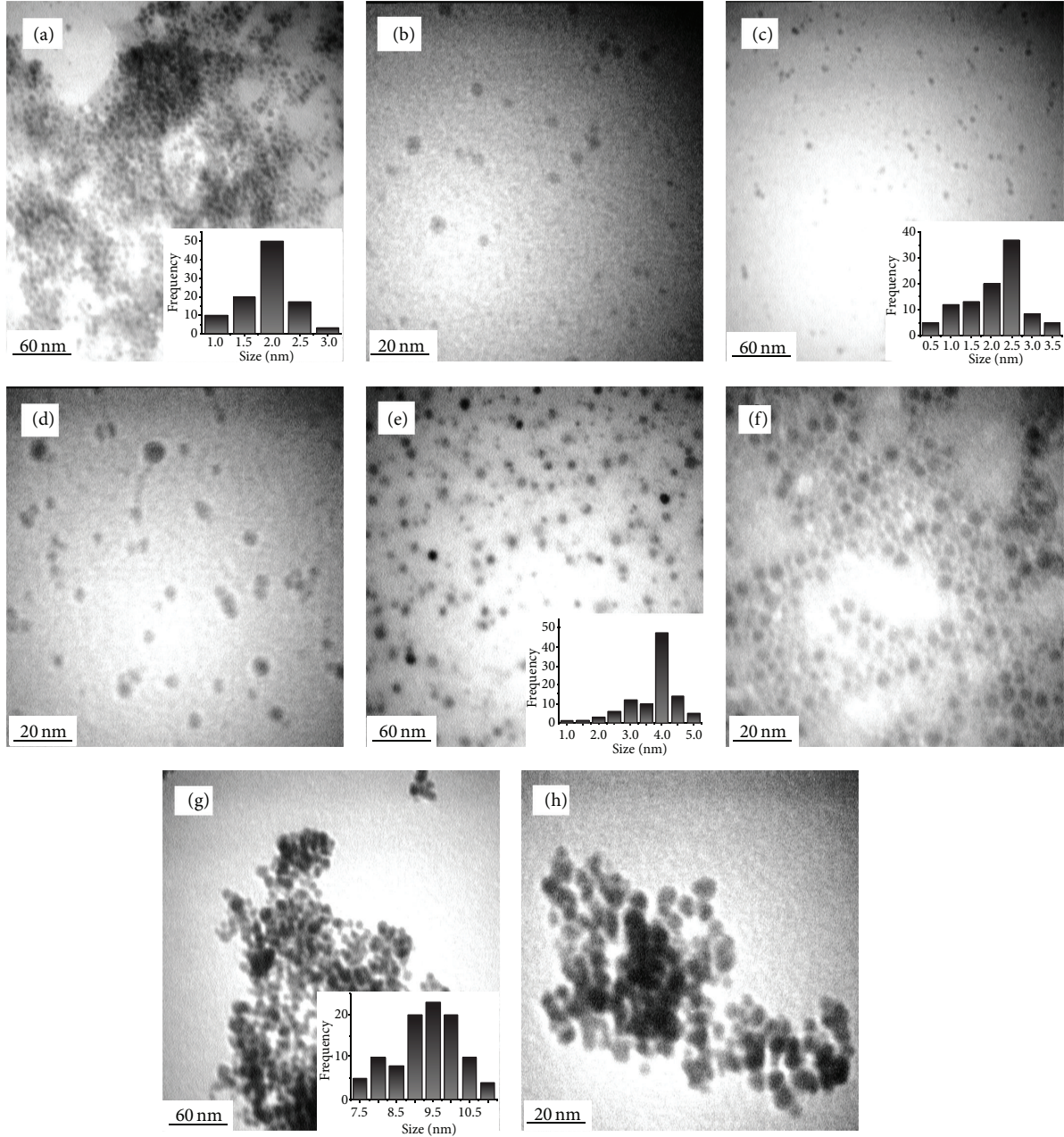


FIGURE 3: TEM micrographs of as-synthesized nanoparticles and corresponding size distributions: (a) W1, (b) W1 at higher magnification, (c) W2, (d) W2 at higher magnification, (e) W3, (f) W3 at higher magnification, (g) W4, and (h) W4 at higher magnification.

nanoparticle size the thickness of this dead layer reduces and the magnetization of nanoparticle increases [28].

It is also seen from Figures 5(a) and 5(b) that the coercivity is size dependent. In fact by increasing the nanoparticles size the coercivity increases such that for W4 sample the high coercive field of 100 Oe is achieved. The reduced coercive force in terms of nanoparticle size at constant temperature is described as

$$h_c = 1 - \left(\frac{V_p}{V}\right)^{1/2} = 1 - \left(\frac{D_p}{D}\right)^{3/2}, \quad (4)$$

where h_c is the reduced coercive field ($H_c/H_{c,(T=0)}$), D is the nanoparticle size, and D_p is the critical nanoparticle size in which the anisotropy energy (KV) dominates the thermal energy (k_bT) and the magnetic properties change from superparamagnetic to ferromagnetic.

The critical size D_p depends on the composition of nanoparticles as for iron oxide nanoparticles and it has the value of 12 nm [29] or for $\text{Fe}_{74.5-x}\text{Cu}_x\text{Nb}_3\text{Si}_{22.5-y}\text{B}_y$ alloy nanoparticles D_p is dependent on x and y and changes from 10 nm for 1 at % Cu and 9 at % B to 15 nm for 1 at % Cu and 6 at % B [30]. When $D \leq D_p$, the coercive field is zero and further increasing in nanoparticle size beyond D_p increases the coercivity. It is why for both W and M series of samples

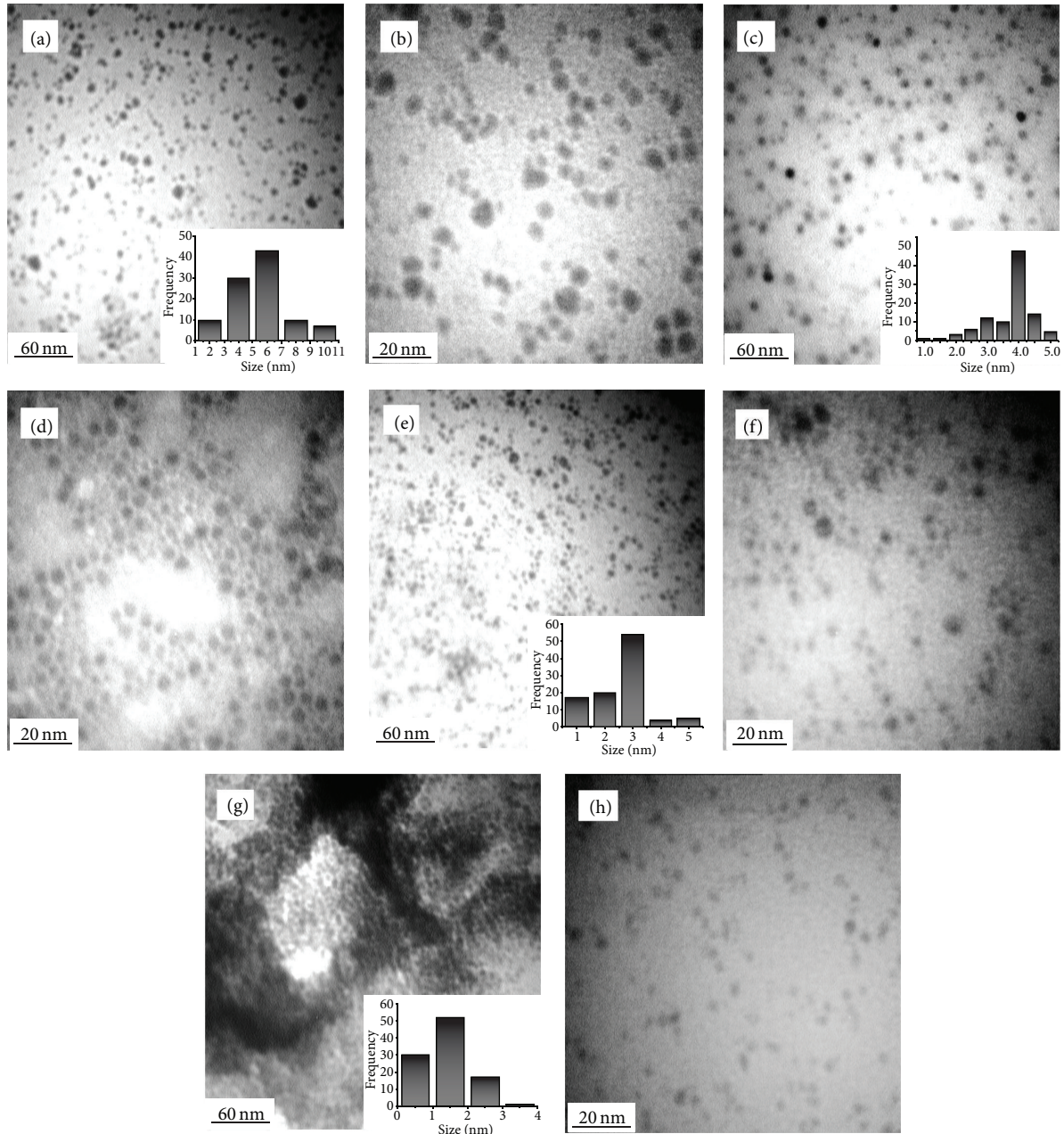


FIGURE 4: TEM micrographs of as-synthesized nanoparticles and corresponding size distributions: (a) M1, (b) M1 at higher magnification, (c) W3, (d) W3 at higher magnification, (e) M2, (f) M2 at higher magnification, (g) M3, and (h) M3 at higher magnification.

the coercivity increases with size. Only an exception is observed in the case of M3 specimen in which regardless of its greater size the coercivity is less than W3 sample. The reason could be the partial oxidation of M3 sample, but more investigations are needed.

Figure 6 shows TEM images and corresponding hysteresis curves for W3 annealed samples. It is seen from Figures 6(a) and 6(b) that the nanoparticles have grown up by fusion-fission to a mean size of 60 and 25 nm, respectively. As expected, by increasing the size of nanoparticles the corresponding saturation magnetizations have been increased

(to 128 emu/g and 78 emu/g) but are still smaller than the bulk value (240 emu/g).

Figure 7 shows the coercivity as a function of particle size. It is seen that the coercivity has been decreased from 100 Oe for as-synthesized W3 to 60 and 40 Oe for annealed samples. The reason lies in the mechanism of magnetization. In multidomain particles magnetization reversal takes place by the motion of domain walls, but in single domain particles the magnetization reversal occurs by coherent reversal of the magnetic moment which requires the anisotropy energy to be dominated. Since the anisotropy energy is much higher

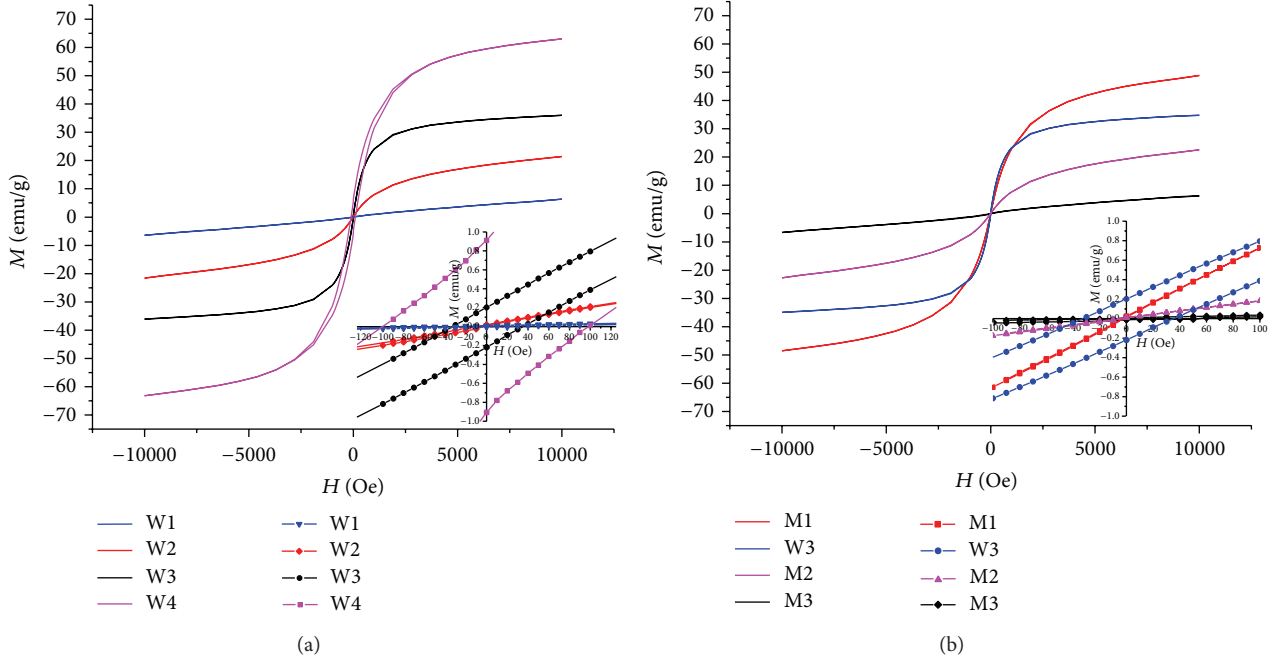


FIGURE 5: Magnetization curves for as-synthesized nanoparticles showing the effect of (a) water to surfactant molar ratio (R) (b) concentration of metal salts.

than domain wall energy, the coercivity increases by the transition from multi-domain to single domain size regime. But with further decreasing the size, the coercivity diminishes as the result of decreasing the anisotropy energy (KV) such that below $D = 4$ nm the coercivity reaches zero exhibiting superparamagnetic behavior. Therefore D_p for as-synthesized FeCo nanoparticles is about 4 nm. So it is inferred that the transition from superparamagnetic to ferromagnetic is at 4 nm and the transition between single domain-multi domain size regimes is at 9 nm.

3.5. Calculation of SAR. Some researches on the inductive magnetic properties of nanoparticles represent the superparamagnetic-ferromagnetic transition to have maximum SAR [15] and some other works show that the maximum SAR is achieved at single domain-multi domain boundary [16]. For single domain-multi domain transition size the Stoner-Wohlfarth model is used to estimate the magnetic response. Therefore for W4 sample on the basis of (5) for random orientation nanoparticles we have

$$2\mu_0 H_{c,(T=0\text{K})} M_s = 1.92 K_{\text{eff}}, \quad (5)$$

where $H_{c,(T=0\text{K})}$ is the coercive field at $T = 0$ K which could be calculated from $H_{c,(T=300\text{K})}$ using the following equation [16]:

$$\frac{H_{c,(T=0\text{K})}}{H_{c,(T=300\text{K})}} = \frac{1 - \left(\frac{k_B T_1}{K_{\text{eff}} V} \right) \left(\ln \left(\frac{1}{f \tau_0} \right) \right)^{3/4}}{1 - \left(\frac{k_B T_2}{K_{\text{eff}} V} \right) \left(\ln \left(\frac{1}{f \tau_0} \right) \right)^{3/4}}, \quad (6)$$

where k_B is the Boltzmann constant, V is the volume of nanoparticle, f is the measurement frequency 5.5×10^{-4} (Hz), $\tau_0 = 10^{-10}$ (s), $T_1 = 0$ K, and $T_2 = 300$ K. By

solving the system of (5) and (6) simultaneously, the effective anisotropy would be calculated as $K_{\text{eff}} = 3.8 \times 10^4$ (J/m³) and $\mu_0 H_{c,(T=0\text{K})} \approx 145$ mT. Then the coercive field at $T = 300$ K and the frequency of hyperthermia treatment $f = 100$ kHz could be calculated from (7) [16]:

$$\mu_0 H_{c,(T_1,f)} = 0.48 \mu_0 H_k \left[1 - \left(\frac{k_B T_1}{K_{\text{eff}} V} \left(\ln \frac{1}{f \tau_0} \right) \right)^{3/4} \right]. \quad (7)$$

Lacroix et al. [31] have shown that the results from the Stoner-Wohlfarth model for random orientation FeCo nanoparticles are coherent with experimental results from calorimetry. According to equation $\mu_0 H_{c,(T=0\text{K})} = 0.48 \mu_0 H_k$ at $T = 0$ K and (7) at $T = 300$ K and $f = 100$ KHz for the Stoner-Wohlfarth nanoparticles ($A \cong 2\mu_0 H_c M_s$) it could be calculated that $A \cong 8.47$ (mJ/g) and SAR = 847 (W/g).

For the above calculations to be valid the condition $\mu_0 H_{\text{max}} \geq \mu_0 H_{c,(T=300\text{K},f=100\text{KHz})} \approx 70$ mT should be satisfied such that in each reversal of the applied field the full area of the hysteresis loop could be placed within the limits of the applied alternating field.

The obtained value of SAR is comparable to the highest value of 1700 (W/g) reported by Mehdaoui et al. for iron based nanoparticles [32] and larger than values of 450 (W/g) and 198 (W/g) for magnetite nanoparticles reported by Bakoglidis et al. [29] and Wang et al. [33], respectively. It should be noted that a broad range of SAR was calculated by Carrey et al. [16] depending on the anisotropy of the nanoparticles ranging from 1 to 2000 (W/g).

For superparamagnetic-ferromagnetic transition the LRT approximation should be applied. For the sake of simplicity it is assumed that $K_{\text{eff}} = 3.8 \times 10^4$ (J/m³). Considering $\tau_R = \tau_N = \tau_0 \exp(K_{\text{eff}} V / (k_B T))$ the relaxation time could be obtained as

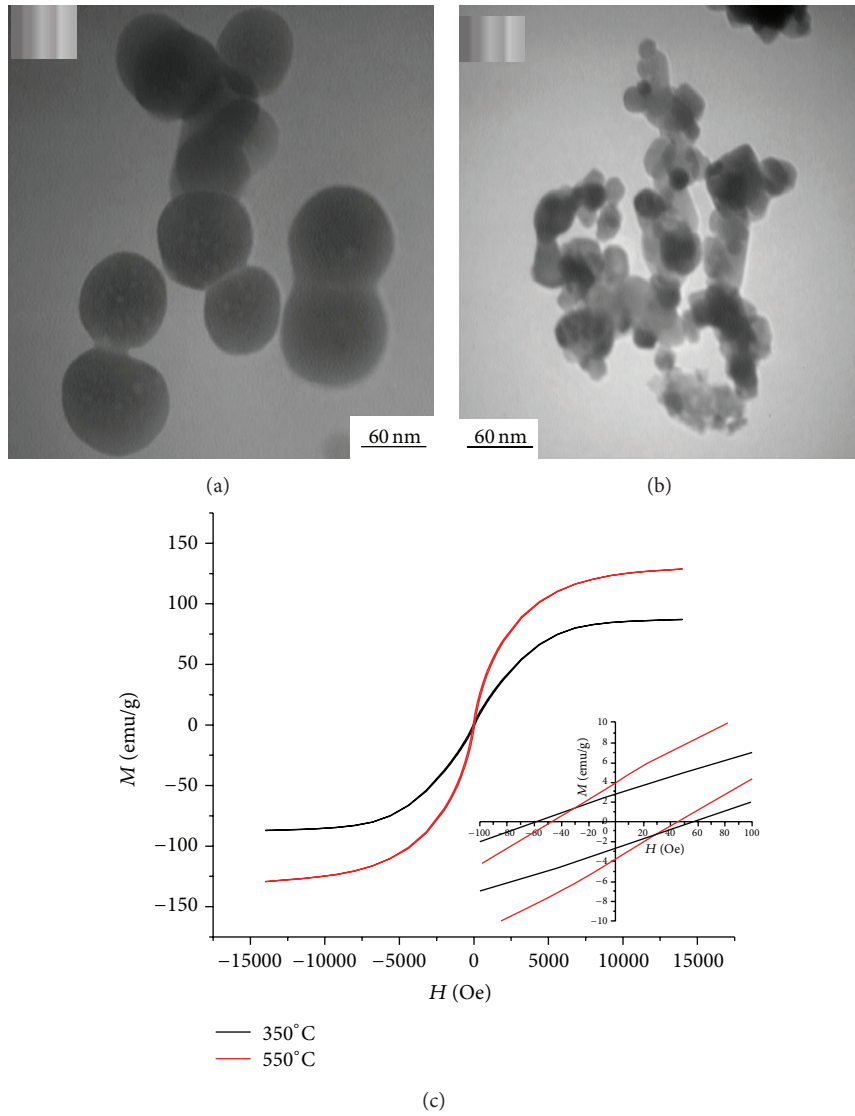


FIGURE 6: TEM images of W3 sample annealed for 20 minutes at (a) 550°C and (b) 350°C. (c) Hysteresis curves for annealed samples.

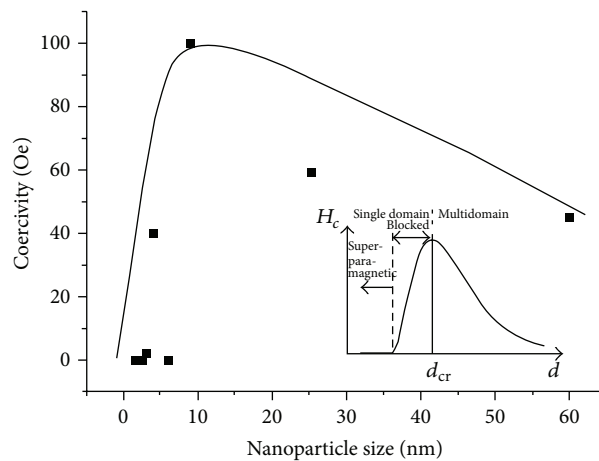


FIGURE 7: Coercivity as a function of particle size (continuous line is the trend, inset: [1]).

$\tau_R = 1.171 \times 10^{-9}$ (s). Finally from (1), the area of the dynamic hysteresis loop would be $A = 2.62 \times 10^{-8}$ (mJ/g) with the corresponding SAR = 0.262×10^{-2} (W/g). This is a rough estimation for W3 sample because the anisotropy field was assumed to be equal to that of W4 sample. But qualitatively it could be deduced that for W4 sample in the single domain-multi domain boundary the SAR is much higher (about 10^5 times) than W3 sample at ferromagnetic-superparamagnetic transition. Indeed the reason lies in the loss mechanism: hysteresis loss versus the Neel-Brown relaxation. The former is described by the Stoner-Wohlfarth models which assume null thermal activation and predict a square hysteresis area (W4 sample), but the latter assumes thermal equilibrium and a linear response of magnetic system to applied magnetic field (W3 sample).

Theoretically it is expected that the higher the frequency of the applied field the higher the losses. But experimental results indicate that by increasing the frequency of the applied field the generated heat reaches a frequency independent maximum. This could be due to nanoparticle interaction which makes hysteresis area independent of frequency [31]. In fact the above calculations are based on the hypothesis that the nanoparticles do not have considerable interactions with each other. In order to take the interactions into account, Monte-Carlo simulations should be used. But there is a severe problem in matching the time in simulations with the real time and to the best of the authors' knowledge there is no theoretical expression for this problem [31].

Another important point to be highlighted is that the above calculations neglect the Brownian relaxations (physical motion of nanoparticles under the influence of the magnetic field) in colloidal solution. By considering the effect of this type of relaxation some of the applied field will be dissipated due to the physical rotation of nanoparticles to align them along the applied field and the generated heat will be different from the above values.

Based on the large obtained theoretical SAR it could be inferred that W4 sample (with mean size of 9 nm) has a great advantage to be used in magnetic hyperthermia treatment. But to assay these theoretical results which are based on the simple SW model, real experiments will be the subject of the future work to measure the values of A and SAR comparing them with these theoretical results.

4. Conclusions

Size controlled synthesis of FeCo nanoparticles was done using microemulsion method. The main parameters which determine the particle size are water to surfactant molar ratio (R) and molar concentration of metal salts. By increasing the former the size of micelles increases leading to larger terminal nanoparticles and by raising the latter the number of formed nuclei increases leading to smaller terminal nanoparticles.

Size dependency of magnetic properties including M_s and H_c was investigated. The observed increase of M_s with size is due to the disappearance of the magnetic dead layer in larger nanoparticles. But the observed change in coercivity is due to the transition between various size regimes

and consequently the magnetization reversal mechanisms. Based on the variations of coercivity the superparamagnetic-ferromagnetic and single domain-multi domain transition sizes were determined.

Then the magnetic losses were calculated at transition points based on the Stoner-Wohlfarth and LRT models. For W4 sample which is at the single domain-multi domain ferromagnetic transition point the anisotropy field, $H_{c,(T=0\text{ K})}$, and SAR were calculated using the Stoner-Wohlfarth model. The results are comparable to the highest reported in the literature. It should be noted that the results are applicable only when $x_0 H_{\max} \geq x_0 H_{c,(T=300\text{ K}, f=100\text{ KHz})} \approx 70\text{ mT}$.

But for W3 sample at superparamagnetic-single domain ferromagnetic transition the approximate SAR was obtained very lower than that of W4 sample. Based on the large obtained theoretical SAR it could be concluded that W4 sample (with mean size of 9 nm) has a high potential to be used in magnetic hyperthermia treatment. Future experiments such as calorimetry could assay the theoretical results of the present research.

Conflict of Interests

The authors declare that there is no conflict of interests regarding the publication of this paper.

References

- [1] S. P. Gubin, Y. A. Koksharov, G. B. Khomutov, and G. Y. Yurkov, "Magnetic nanoparticles: preparation, structure and properties," *Russian Chemical Reviews*, vol. 74, no. 6, pp. 489–520, 2005.
- [2] K. Zábanský, B. David, N. Pizúrová, O. Schneeweiss, R. Zbořil, and M. Mašláň, "Preparation and properties of FeCo nanoparticles," in *Mossbauer Spectroscopy in Materials Science*, vol. 1258 of *AIP Conference Proceedings*, pp. 102–107, 2010.
- [3] D. Kodama, K. Shinoda, K. Sato, Y. Sato, B. Jeyadevan, and K. Tohji, "Synthesis of size-controlled Fe-Co alloy nanoparticles by modified polyol process," *Journal of Magnetism and Magnetic Materials*, vol. 310, no. 2, pp. 2396–2398, 2007.
- [4] M. Abbas, M. NazrullIslam, B. P. Rao, T. Ogawa, M. Takahashi, and C. G. Kim, "One-pot synthesis of high magnetization air-stable FeCo nanoparticles by modified polyol method," *Materials Letters*, vol. 91, pp. 326–329, 2013.
- [5] U. Cho, K. Wang, G. W. Kim, and B. H. Koo, "Effects of Ag seed on synthesis of FeCo nano-particles prepared via the polyol method," *Journal of Materials Science and Technology*, vol. 26, no. 7, pp. 660–664, 2010.
- [6] G. Suresh, P. Saravanan, and D. R. Babu, "One-pot synthesis of Fe-Co nanospheres by modified polyol process and their structural, magnetic studies," *Journal of Physics*, vol. 292, no. 1, Article ID 012015, 2011.
- [7] Q. Nguyen, C. N. Chinnasamy, S. D. Yoon et al., "Functionalization of FeCo alloy nanoparticles with highly dielectric amorphous oxide coatings," *Journal of Applied Physics*, vol. 103, no. 7, Article ID 07D532, 2008.
- [8] S. J. Lee, J. H. Cho, C. Lee, J. Cho, Y. R. Kim, and J. K. Park, "Synthesis of highly magnetic graphite-encapsulated FeCo nanoparticles using a hydrothermal process," *Nanotechnology*, vol. 22, no. 37, Article ID 375603, 2011.

- [9] E. Holodshikov, I. Perelshtein, and A. Gedanken, "Synthesis of air stable FeCo/C alloy nanoparticles by decomposing a mixture of the corresponding metal-acetyl acetates under their autogenic pressure," *Inorganic Chemistry*, vol. 50, no. 4, pp. 1288–1294, 2011.
- [10] G. H. Lee, S. H. Huh, J. W. Jeong et al., "Structural and magnetic properties of bimetallic FeCo nanoclusters," *Journal of the Korean Physical Society*, vol. 42, no. 3, pp. 367–370, 2003.
- [11] Z. Guo, L. L. Henry, and E. J. Podlaha, "CoFe, Fe and Co nanoparticles displacement with Cu ions," *ECS Transactions*, vol. 3, no. 25, pp. 337–345, 2007.
- [12] X. W. Wei, G. X. Zhu, Y. J. Liu, Y. H. Ni, Y. Song, and Z. Xu, "Large-scale controlled synthesis of FeCo nanocubes and microcages by wet chemistry," *Chemistry of Materials*, vol. 20, no. 19, pp. 6248–6253, 2008.
- [13] S. J. Shin, Y. H. Kim, C. W. Kim, H. G. Cha, Y. J. Kim, and Y. S. Kang, "Preparation of magnetic FeCo nanoparticles by coprecipitation route," *Current Applied Physics*, vol. 7, no. 4, pp. 404–408, 2007.
- [14] C. S. S. R. Kumar and F. Mohammad, "Magnetic nanomaterials for hyperthermia-based therapy and controlled drug delivery," *Advanced Drug Delivery Reviews*, vol. 63, no. 9, pp. 789–808, 2011.
- [15] R. Hergt, S. Dutz, R. Müller, and M. Zeisberger, "Magnetic particle hyperthermia: nanoparticle magnetism and materials development for cancer therapy," *Journal of Physics Condensed Matter*, vol. 18, no. 38, pp. S2919–S2934, 2006.
- [16] J. Carrey, B. Mehdaoui, and M. Respaud, "Simple models for dynamic hysteresis loop calculations of magnetic single-domain nanoparticles: application to magnetic hyperthermia optimization," *Journal of Applied Physics*, vol. 109, no. 8, Article ID 083921, 2011.
- [17] M. Hesani, A. Yazdani, B. Abedi Ravan, and M. Ghazanfari, "The effect of particle size on the characteristics of FeCo nanoparticles," *Solid State Communications*, vol. 150, no. 13–14, pp. 594–597, 2010.
- [18] A. N. Popova, Y. A. Zaharov, and V. M. Pugachev, "Chemical synthesis, structure and magnetic properties of nanocrystalline Fe–Co alloys," *Materials Letters*, vol. 74, pp. 173–175, 2012.
- [19] C. Destrée and J. B. Nagy, "Mechanism of formation of inorganic and organic nanoparticles from microemulsions," *Advances in Colloid and Interface Science*, vol. 123–126, pp. 353–367, 2006.
- [20] M. A. López-Quintela, "Synthesis of nanomaterials in microemulsions: formation mechanisms and growth control," *Current Opinion in Colloid and Interface Science*, vol. 8, no. 2, pp. 137–144, 2003.
- [21] R. M. Espí, C. K. Weiss, and K. Landfester, "Inorganic nanoparticles prepared in miniemulsion," *Current Opinion in Colloid and Interface Science*, vol. 17, no. 4, pp. 212–224, 2012.
- [22] F. J. Schork, Y. Luo, W. Smulders, J. P. Russum, A. Butté, and K. Fontenot, "Miniemulsion polymerization," *Advances in Polymer Science*, vol. 175, pp. 129–255, 2005.
- [23] C. C. Wang, D. H. Chen, and T. C. Huang, "Synthesis of palladium nanoparticles in water-in-oil microemulsions," *Colloids and Surfaces A*, vol. 189, no. 1–3, pp. 145–154, 2001.
- [24] C. Y. Wang, W. Q. Jiqng, Y. Zhou, Y. N. Wang, and Z. Y. Chen, "Synthesis of α -Fe ultrafine particles in a saturated salt solution/isopropanol/PVP microemulsion and their structural characterization," *Materials Research Bulletin*, vol. 35, no. 1, pp. 53–58, 2000.
- [25] M. A. López-Quintela, C. Tojo, M. C. Blanco, L. G. Rio, and J. R. Leis, "Microemulsion dynamics and reactions in microemulsions," *Current Opinion in Colloid and Interface Science*, vol. 9, no. 3–4, pp. 264–278, 2004.
- [26] M. Ethayaraja and R. Bandyopadhyaya, "Population balance models and Monte Carlo simulation for nanoparticle formation in water-in-oil microemulsions: implications for CdS synthesis," *Journal of the American Chemical Society*, vol. 128, no. 51, pp. 17102–17113, 2006.
- [27] J. T. Miller, A. J. Kropf, Y. Zha et al., "The effect of gold particle size on Au–Au bond length and reactivity toward oxygen in supported catalysts," *Journal of Catalysis*, vol. 240, no. 2, pp. 222–234, 2006.
- [28] D. X. Chen, O. Pascu, A. Roig, and A. Sanchez, "Size analysis and magnetic structure of nickel nanoparticles," *Journal of Magnetism and Magnetic Materials*, vol. 322, no. 24, pp. 3834–3840, 2010.
- [29] K. D. Bakoglidis, K. Simeonidis, D. Sakellari, G. Stefanou, and M. Angelakeris, "Size-dependent mechanisms in AC magnetic hyperthermia response of iron-oxide nanoparticles," *IEEE Transactions on Magnetics*, vol. 48, no. 4, pp. 1320–1323, 2012.
- [30] G. Herzer, "Grain size dependence of coercivity and permeability in nanocrystalline ferromagnets," *IEEE Transactions on Magnetics*, vol. 26, no. 5, pp. 1397–1402, 1990.
- [31] L. M. Lacroix, R. B. Malaki, J. Carrey et al., "Magnetic hyperthermia in single-domain monodisperse FeCo nanoparticles: evidences for Stoner-Wohlfarth behavior and large losses," *Journal of Applied Physics*, vol. 105, no. 2, Article ID 023911, 2009.
- [32] B. Mehdaoui, A. Meffre, L. M. Lacroix et al., "Large specific absorption rates in the magnetic hyperthermia properties of metallic iron nanocubes," *Journal of Magnetism and Magnetic Materials*, vol. 322, no. 19, pp. L49–L52, 2010.
- [33] X. Wang, H. Gu, and Z. Yang, "The heating effect of magnetic fluids in an alternating magnetic field," *Journal of Magnetism and Magnetic Materials*, vol. 293, no. 1, pp. 334–340, 2005.

Research Article

Synthesis of Dendritic Silver Nanoparticles and Their Applications as SERS Substrates

Jinshan Yu and Xingui Zhou

Science and Technology on Advanced Ceramic Fibers and Composites Laboratory, College of Aerospace Science and Engineering, National University of Defense Technology, Changsha 410073, China

Correspondence should be addressed to Jinshan Yu; jjss_y@163.com

Received 2 September 2013; Revised 7 November 2013; Accepted 28 November 2013

Academic Editor: Luís Cunha

Copyright © 2013 J. Yu and X. Zhou. This is an open access article distributed under the Creative Commons Attribution License, which permits unrestricted use, distribution, and reproduction in any medium, provided the original work is properly cited.

The silver nanoparticles are synthesized by electrodeposition in ultradilute Ag^+ concentration electrolyte under high overpotential. The as prepared Ag nanoparticles, with the sizes ranging from 20 to 30 nm, are arrayed orderly and formed dendritic morphology. The formation of this special dendritic nanoparticle structure can be contributed to the relatively high growth rate and the preferential growth directions along $\langle 111 \rangle$ due to the high overpotential, as well as the relative small number of Ag^+ ions arriving at the Ag crystal surface per unit time due to the ultradilute Ag^+ concentration. Surface enhanced Raman scattering (SERS) experiments reveal that the as-prepared dendritic Ag nanoparticles possess high SERS properties and can be used as a candidate substrate for practical SERS applications to detect the Rhodamine 6G molecules.

1. Introduction

The surface enhanced Raman scattering (SERS) is a technique that can determine an enhanced Raman signal when a Raman active-molecule is close to an appropriate metallic substrate surface [1]. Recently this technique has been developed into a valuable tool for chemical and biological sensing due to its high level of sensitivity and high spectroscopic precision [2–4]. Raman signal amplification depends on electromagnetic and chemical enhancement which arises from the interaction between molecules and the active substrate of metal nanostructures [5, 6]. Previous studies have demonstrated that coinage metals, in particular, Ag, usually provide much stronger SERS enhancements than alkali metals or transition metals because the surface-plasmon resonance of these free-electron metals can be effectively excited by visible light [7–9]. Thus the nanostructured Ag are important candidates for practical SERS applications. Usually the unique physical and chemical properties of noble metal nanoparticles are highly dependent on their size, shape, and environment of the particles [10]. As a result, great attention has been directed toward the control of the noble metal nanoparticles size, size distribution, and their morphology. So far, many methods of preparing SERS-active Ag substrates have been extensively

explored in order to obtain substrates with high enhancement ability and stability [11–13]. Here we report the newly synthesized arrayed dendritic Ag nanoparticles through a simple electrodeposited method and their application as a SERS substrate.

2. Experimental Procedure

The dendritic Ag nanoparticles were synthesized by electrochemical deposition method at room temperature. A classical three-electrode setup (Iviumstat electrochemical analyzer, Ivium Technology) was used to carry out the electrochemical experiments. All chemicals were of reagent grade and were used without further purification. Highly diluted Ag_2SO_4 was used to guarantee the nanostructure of the as-deposited products and the pH value of the plating solution was adjusted by adding H_2SO_4 to keep a suitable electrical conductivity. ITO glass sheets were used as the working electrodes on which the nanostructured Ag was deposited. A silver-silver chloride electrode was chosen as the reference and a pure Pt sheet positioned parallel to the ITO glass was used as the counter electrode. A salt bridge was used between the cell and the reference electrode.

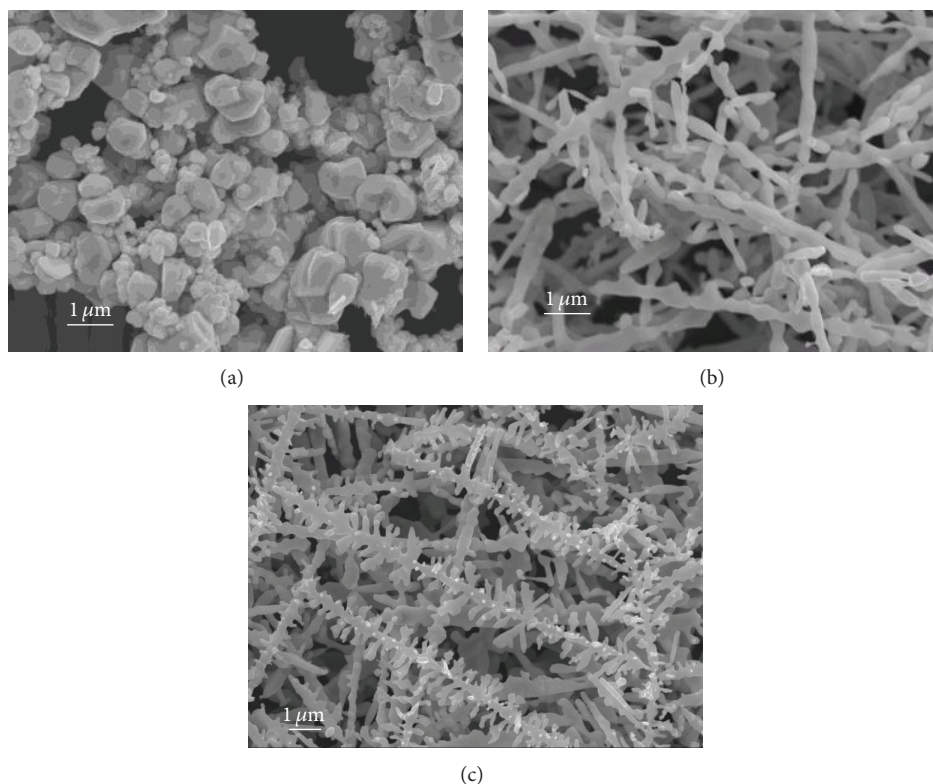


FIGURE 1: The SEM micrograph of Ag nanostructures deposited in 0.5 mM Ag_2SO_4 at different potentials: (a) 0 V, (b) -0.1 V, and (c) -0.25 V.

The microstructure of the as-prepared nanostructured Ag was inspected by a Hitachi S-4800 scanning electron microscope (SEM) equipped with an X-ray energy dispersive spectroscopy (EDX). Surface enhanced Raman scattering was measured from 400 to 1700 cm^{-1} at room temperature by a Bruker VERTEK 70 Raman spectrometer with a 514.5 nm Ar ion laser. The laser power focused on the sample is 50 mW and the acquisition time is 1 second. The Rhodamine 6G (R6G), which was used as probe molecule, was dissolved into pure water ($18.2\text{ M}\Omega$). Before SERS measurements, the ITO glasses deposited with the dendritic Ag nanoparticles were immersed in the solution for 2 h for sufficient molecule adsorption and then were dried in air for 4 hours.

3. Results and Discussion

As we had reported early, the noble metal nanostructures can be fabricated by electrodeposition method in a highly diluted solution with a special deposition mechanism [14]. The shape of the as-deposited nanostructured noble metals can be controlled by tuning the depositing potentials. In this study we firstly studied the electrodeposition of Ag nanostructures at different potentials in a mixed electrolyte composed of $0.5\text{ mM Ag}_2\text{SO}_4$ and $1\text{ M H}_2\text{SO}_4$ in nanopure deionized water. Figure 1 shows the morphology of Ag nanostructures deposited at different potentials. As shown in Figure 1(a), at deposition potentials of 0 V , the Ag particles are formed with the size of $\sim 1\text{ }\mu\text{m}$. With more negative potential (-0.1 V), the bamboo-like Ag rods with the diameter of $\sim 300\text{ nm}$ are

formed, as shown in Figure 1(b), which implies the preferred growth of the Ag crystals. At an overpotential of -0.25 V , dendritic Ag nanostructures with size scale of $\sim 200\text{ nm}$ are obtained, as shown in Figure 1(c).

Then the Ag nanostructures are electrochemically deposited in more dilute solution. The concentration of Ag_2SO_4 decreases to 0.2 mM . Figure 2 shows the SEM micrograph of Ag nanostructure electrochemically deposited at the overpotential of -0.25 V . The feather-like Ag dendritic nanostructure is obtained, as shown in Figure 2(a). The EDX result (Figure 2(b)) confirms that the as-obtained Ag nanostructure is only composed of Ag. High-magnification SEM micrograph (Figure 2(c)) shows that a single Ag dendrite consists of many subdendrites. Figure 2(d) shows an ultra-high-magnification SEM micrograph of the Ag sub-dendrite. It clearly shows that an Ag sub-dendrite is composed of Ag nanoparticles with the size of $\sim 30\text{ nm}$, which is arrayed into a dendritic morphology.

The formation of this special dendritic nanoparticle structure can be contributed to the electrochemical deposition mechanism in ultradilute solution. At the deposition potential of -0.25 V , the overpotential is much negative than the standard electrode potential of Ag ($+0.799\text{ V}$). At this deposition potential the Ag crystals should have a relatively high growth rate and the preferential growth direction along $\langle 111 \rangle$ [14]. However, the Ag^+ in electrolyte are very dilute; thus the number of Ag^+ ions arriving at the Ag crystal surface per unit time is small. The arrived Ag^+ have enough time to find the coordination sites to decrease the surface energy.

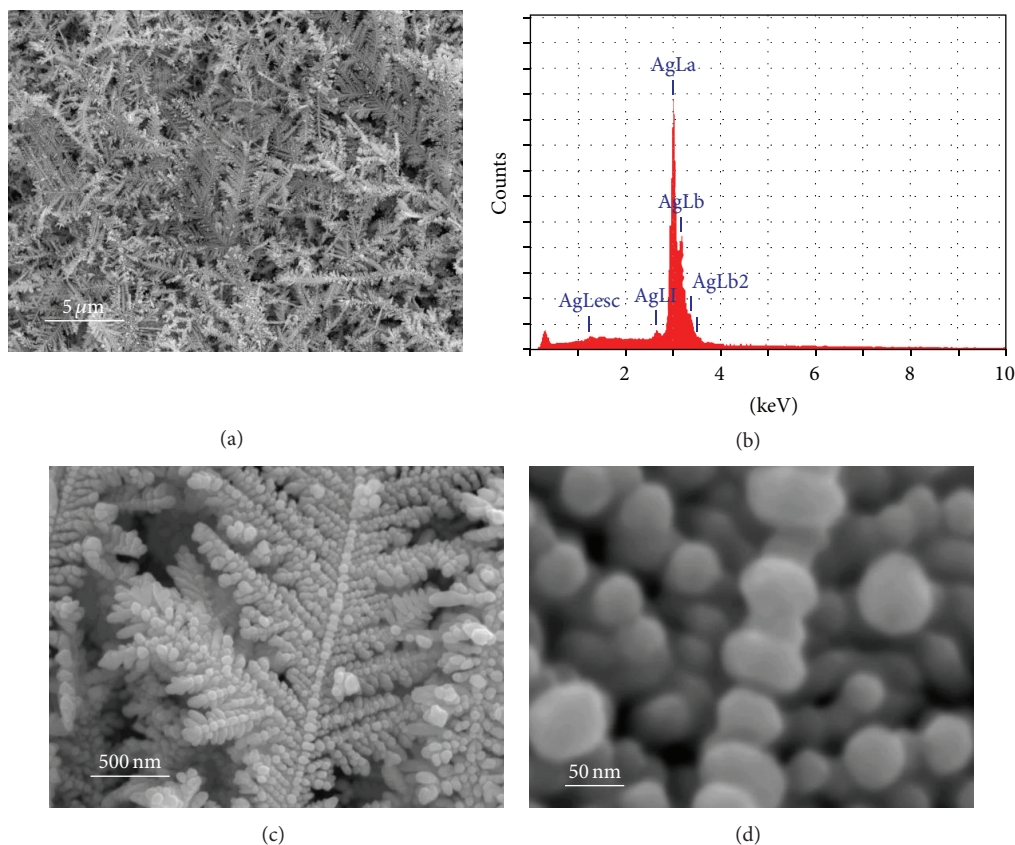


FIGURE 2: The SEM micrograph of Ag nanostructure electrochemically deposited in 0.2 mM Ag_2SO_4 with the overpotential of -0.25 V: (a) Low magnification, (b) EDX result, (c) high magnification, and (d) ultra-high magnification.

Thus the spherical Ag nanoparticles are formed. It can be concluded that the arrayed dendritic nanoparticle structure is formed due to the high overpotential and the ultradilute Ag^+ concentration.

Figure 3 shows the SERS spectrum of R6G molecules on dendritic Ag nanoparticles. The concentration of R6G solution is 10^{-10} M. It can be seen that the SERS intensity is relatively strong, which implies that these dendritic Ag nanoparticles have the potential to detect more dilute R6G solution. It is generally believed that SERS is a highly heterogeneous process due to local enhancements at certain “hot spots” coming from the nanostructure [15]. In this dendritic Ag nanoparticle, the positions of each Ag nanoparticle are ordered and relative fixed; therefore the aggregations of Ag nanoparticles cannot occur. These arrayed Ag nanoparticles act as the “hot spots,” trapping the analyte in those junctions, leading to a high SERS activity. It confirms that the as-prepared dendritic Ag nanoparticles can be used as a high performance substrate for practical SERS applications to detect the R6G molecules.

4. Conclusion

In summary, the silver nanoparticles are synthesized by electrodeposition in ultradilute Ag^+ concentration electrolyte

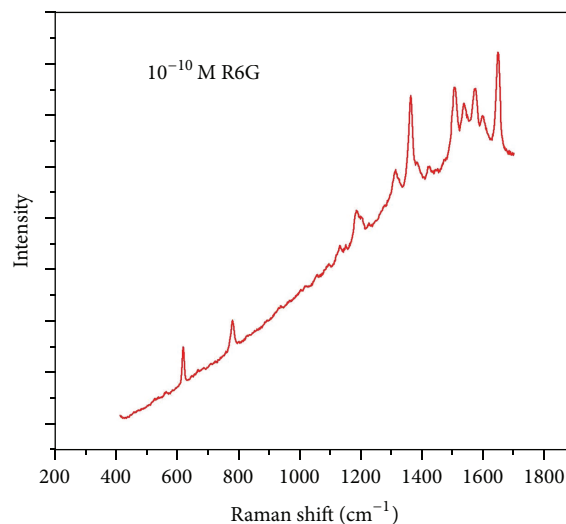


FIGURE 3: The SERS spectrum of R6G molecules on dendritic Ag nanoparticles.

under high overpotential. The as-prepared dendritic Ag nanoparticles possess high SERS properties and can be used as a candidate substrate for practical SERS applications to detect the Rhodamine 6G molecules.

Acknowledgments

This work was financially supported by the Fundamental Research Fund of National University of Defense Technology, the Research Fund of State Key Laboratory of CFC (Grant no. 9140C820301110C8201), and the National Natural Science Foundation of China (Grant no. 51372274).

Journal of the American Chemical Society, vol. 128, no. 7, pp. 2200–2201, 2006.

References

- [1] C. L. Haynes, A. D. McFarland, and R. P. van Duyne, "Surface-enhanced: Raman spectroscopy," *Analytical Chemistry*, vol. 77, no. 17, pp. 338–346, 2005.
- [2] K. Kneipp, R. F. Aroca, H. Kneipp, and E. Wenzel, *New Approaches in Biomedical Spectroscopy*, Oxford University Press, Oxford, UK, 2007.
- [3] F. C. Adam, K. Khashayar, T. Shi-Yang et al., "In situ SERS probing of nano-silver coated individual yeast cells," *Biosensors and Bioelectronics*, vol. 49, pp. 536–541, 2010.
- [4] W. Wu, M. Wu, Z. Sun et al., "Morphology controllable synthesis of silver nanoparticles: optical properties study and SERS application," *Journal of Alloys and Compounds*, vol. 579, pp. 117–123, 2013.
- [5] M. Moskovits, "Surface-enhanced spectroscopy," *Reviews of Modern Physics*, vol. 57, no. 3, pp. 783–825, 1985.
- [6] A. Campion and P. Kambhampati, "Surface-enhanced Raman scattering," *Chemical Society Reviews*, vol. 27, no. 4, pp. 241–250, 1998.
- [7] Z. Gan, A. Zhao, M. Zhang et al., "A facile strategy for obtaining fresh Ag as SERS active substrates," *Journal of Colloid and Interface Science*, vol. 366, no. 1, pp. 23–27, 2012.
- [8] Z. Q. Tian, B. Ren, and D. Y. Wu, "Surface-enhanced Raman scattering: from noble to transition metals and from rough surfaces to ordered nanostructures," *The Journal of Physical Chemistry B*, vol. 106, no. 37, pp. 9463–9483, 2002.
- [9] B. K. Jena and C. R. Raj, "Seedless, surfactantless room temperature synthesis of single crystalline fluorescent gold nanoflowers with pronounced SERS and electrocatalytic activity," *Chemistry of Materials*, vol. 20, no. 11, pp. 3546–3548, 2008.
- [10] C. Burda, X. Chen, R. Narayanan, and M. A. El-Sayed, "Chemistry and properties of nanocrystals of different shapes," *Chemical Reviews*, vol. 105, no. 4, pp. 1025–1102, 2005.
- [11] L. Y. Chen, Y. S. Yu, T. Fujita, and M. W. Chen, "Nanoporous copper with tunable nanoporosity for SERS applications," *Advanced Functional Materials*, vol. 19, no. 8, pp. 1221–1226, 2009.
- [12] J. Fu, Z. Cao, and L. Yobas, "Localized oblique-angle deposition: Ag nanorods on microstructured surfaces and their SERS characteristics," *Nanotechnology*, vol. 22, no. 50, Article ID 505302, 2011.
- [13] X. Hou, X. Zhang, S. Chen et al., "Facile synthesis of SERS active Ag nanoparticles in the presence of tri-n-octylphosphine sulfide," *Applied Surface Science*, vol. 257, no. 11, pp. 4935–4940, 2011.
- [14] J. Yu, T. Fujita, A. Inoue, T. Sakurai, and M. Chen, "Electrochemical synthesis of palladium nanostructures with controllable morphology," *Nanotechnology*, vol. 21, no. 8, Article ID 085601, 2010.
- [15] S. J. Lee, A. R. Morrill, and M. Moskovits, "Hot spots in silver nanowire bundles for surface-enhanced Raman spectroscopy,"

Research Article

Influence of Annealing Temperature on the Magnetic Properties of Rapidly Quenched $(\text{Nd,Pr})_2\text{-(Fe,Co,Ga,Ti,C)}_{14}\text{B}/\alpha\text{-Fe}$ Nanocomposite Ribbons

Rahim Sabbaghizadeh,¹ Mansor Hashim,² Reza Gholamipour,³
Ghazaleh Bahmanrokh,¹ and Mohd Shamsul Ezzad Shafie¹

¹ Advanced Material and Nanotechnology Laboratory, Institute of Advanced Technology (ITMA), Universiti Putra Malaysia, UPM Serdang 43400, Selangor, Malaysia

² Physics Department, Faculty of Science, Universiti Putra Malaysia, Serdang 43400, Selangor, Malaysia

³ Advanced Materials and Renewal Energy Department, Iran Research Organization for Science and Technology (IROST), Tehran, Iran

Correspondence should be addressed to Rahim Sabbaghizadeh; r.h.sabba@gmail.com

Received 26 September 2013; Accepted 8 November 2013

Academic Editor: Luís Cunha

Copyright © 2013 Rahim Sabbaghizadeh et al. This is an open access article distributed under the Creative Commons Attribution License, which permits unrestricted use, distribution, and reproduction in any medium, provided the original work is properly cited.

The effects of different heat treatment temperatures on the structure and magnetic properties of Nd-Fe-B nanocomposite permanent magnetic alloys with nominal composition of $\text{Nd}_{9.4}\text{Pr}_{0.6}\text{Fe}_{74.5}\text{Co}_6\text{B}_6\text{Ga}_{0.5}\text{Ti}_{1.5}\text{C}_{1.5}$ have been investigated. The most practical method to produce nanostructured metallic materials is rapid solidification. Melt spinning with constant wheel speed of $V = 40$ m/s was employed to produce ribbons. As-spun ribbons were examined by using differential scanning calorimetry (DSC) and X-ray diffractometer (XRD) with $\text{Cu-K}\alpha$ radiation. The ribbons were annealed at different temperatures in order to extract the best magnetic properties. The XRD and electron microscopy technique results confirm that grains are in the size of less than 50 nm. In addition, optimum magnetic properties were obtained at 700°C annealed temperature.

1. Introduction

Recently, considerable attention has been focused on the magnetic properties of nanostructured Nd-Fe-B magnet alloy, which has been prepared by the recrystallization of either melt-spun or mechanically alloyed materials, because of their technological properties and unusual scientific behavior [1–6]. Neodymium-iron-boron nanocomposite magnets consist of a soft magnetic phase ($\alpha\text{-Fe}$ or Fe_3b) and a hard magnetic phase ($\text{Nd}_2\text{Fe}_{14}\text{B}$). In these materials the soft magnetic phase has higher inherent magnetization, and the hard magnetic phase has a higher anisotropy constant and higher remanence; therefore, higher energy product will be achieved in comparison with single phase material because of exchange coupling between the magnetically soft and hard phases. In addition, a smaller amount of rare earth

elements are required [7, 8]. The nanocomposite produced by crystallization of amorphous phase into a mixture of hard and soft phases mainly $\text{Nd}_2\text{Fe}_{14}\text{B}/\alpha\text{-Fe}$. Usually $\alpha\text{-Fe}$ tends to grow during annealing and precipitates sooner than $\text{Nd}_2\text{Fe}_{14}\text{B}$. It is plainly visible that a uniform distribution of fine grains is essential for obtaining effective exchange coupling [9]. Fischer et al. proposed that an optimum microstructure consists of small soft magnetic grains with sizes of about 10 nm and hard magnetic grains with a mean grain diameter of about 20 nm [3]. In order to achieve a significant enhancement of remanence polarisation (J_r) and to preserve a high intrinsic coercivity in isotropic nanocrystalline $\text{Nd}_2\text{Fe}_{14}\text{B}$ -based magnets, a mean grain size of less than 20 nm is required [10]. Furthermore, it was found that the size and volume fraction of $\alpha\text{-Fe}$ and $\text{Nd}_2\text{Fe}_{14}\text{B}$ can be manipulated by thermal processing and by elemental substitution,

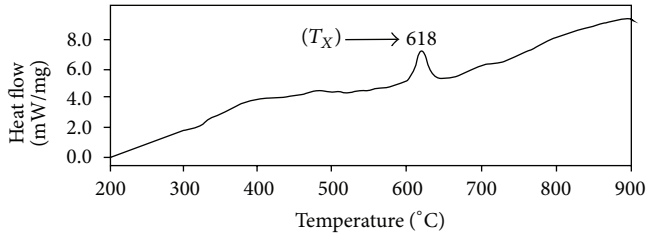


FIGURE 1: DSC scans of $\text{Nd}_{9.4}\text{Pr}_{0.6}\text{Fe}_{74.5}\text{Co}_6\text{B}_6\text{Ga}_{0.5}\text{Ti}_{1.5}\text{C}_{1.5}$.

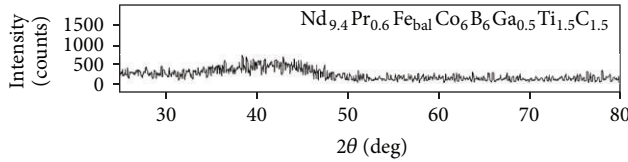


FIGURE 2: X-ray diffraction patterns of as-spun ribbon.

leading to the increase of the magnetic properties, for example, Br and $(\text{BH})_{\text{max}}$ of the fully processed materials [6]. In recent years various investigations have been carried out in order to increase magnetic properties by changing the heat treatment parameters. In this research effect of heat treatment on the structure and magnetic properties of melt-spun $\text{Nd}_{9.4}\text{Pr}_{0.6}\text{Fe}_{74.5}\text{Co}_6\text{B}_6\text{Ga}_{0.5}\text{Ti}_{1.5}\text{C}_{1.5}$ has been investigated.

2. Experimental Procedure

An alloy with the nominal composition of $\text{Nd}_{9.4}\text{Pr}_{0.6}\text{Fe}_{74.5}\text{Co}_6\text{B}_6\text{Ga}_{0.5}\text{Ti}_{1.5}\text{C}_{1.5}$ was prepared by the vacuum arc melting (VAR) method under purified Ar atmosphere. The ingot was produced by this method remelted for four times in order to get the homogeneity. The melt spinning method was used to produce amorphous ribbons in the nanometer scale by a constant wheel speed of $v = 40$ m/s. The chamber Ar pressure was 930 mbar and the ejection pressure was 0.3 bar, and the orifice diameter of quartz tube was 0.5 mm. The as-spun ribbon was sealed in a quartz tube under 4.5×10^{-4} mbar vacuum, after that annealed at four different temperatures (600°C, 650°C, 700°C, and 750°C) for 10 minutes, and then cooled in water. The structure of the ribbons was preliminarily examined using X-ray diffraction (XRD) with monochromatic $\text{Cu-K}\alpha$ radiation before and after annealing. Crystallization evolution and determination of crystallization temperature of the as-cast sample were monitored using differential scanning calorimetry (DSC) on SDT 2960 TA instruments in an Ar atmosphere. Demagnetization curves were measured by using a vibrating sample magnetometer (VSM) after magnetizing the ribbons with a pulsed magnetic field of at least 1.5 T.

3. Results and Discussion

Figure 1 shows the DSC traces for crystallization of $\text{Nd}_{9.4}\text{Pr}_{0.6}\text{Fe}_{74.5}\text{Co}_6\text{B}_6\text{Ga}_{0.5}\text{Ti}_{1.5}\text{C}_{1.5}$ alloy. It is noticeable

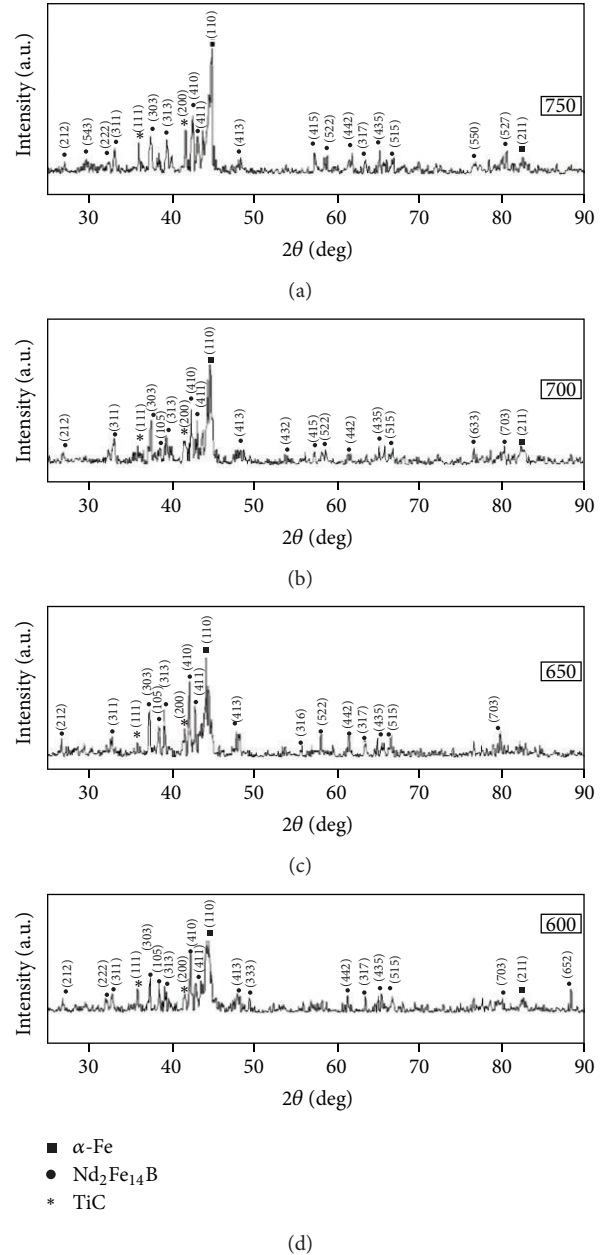


FIGURE 3: XRD patterns of $\text{Nd}_{9.4}\text{Pr}_{0.6}\text{Fe}_{74.5}\text{Co}_6\text{B}_6\text{Ga}_{0.5}\text{Ti}_{1.5}\text{C}_{1.5}$ ribbon after thermal treatment at different temperature for 10 minutes.

that there is only one exothermic peak which means that the prior precipitation of α -Fe was inhibited and crystallization of both α -Fe and $\text{Nd}_2\text{Fe}_{14}\text{B}$ occurs simultaneously. Powder X-ray diffraction patterns of as-quenched $\text{Nd}_{9.4}\text{Pr}_{0.6}\text{Fe}_{74.5}\text{Co}_6\text{B}_6\text{Ga}_{0.5}\text{Ti}_{1.5}\text{C}_{1.5}$ ribbons are shown in Figure 2. The XRD scans of the as-spun ribbons can be used to qualitatively estimate the amount of glass formation [6]. As it was mentioned before the wheel speed is constant and because of the straight relation between cooling rate and wheel speed it can be concluded that the cooling rate in our experiment is constant so the formation of amorphous structures is due to change of critical cooling rate necessary

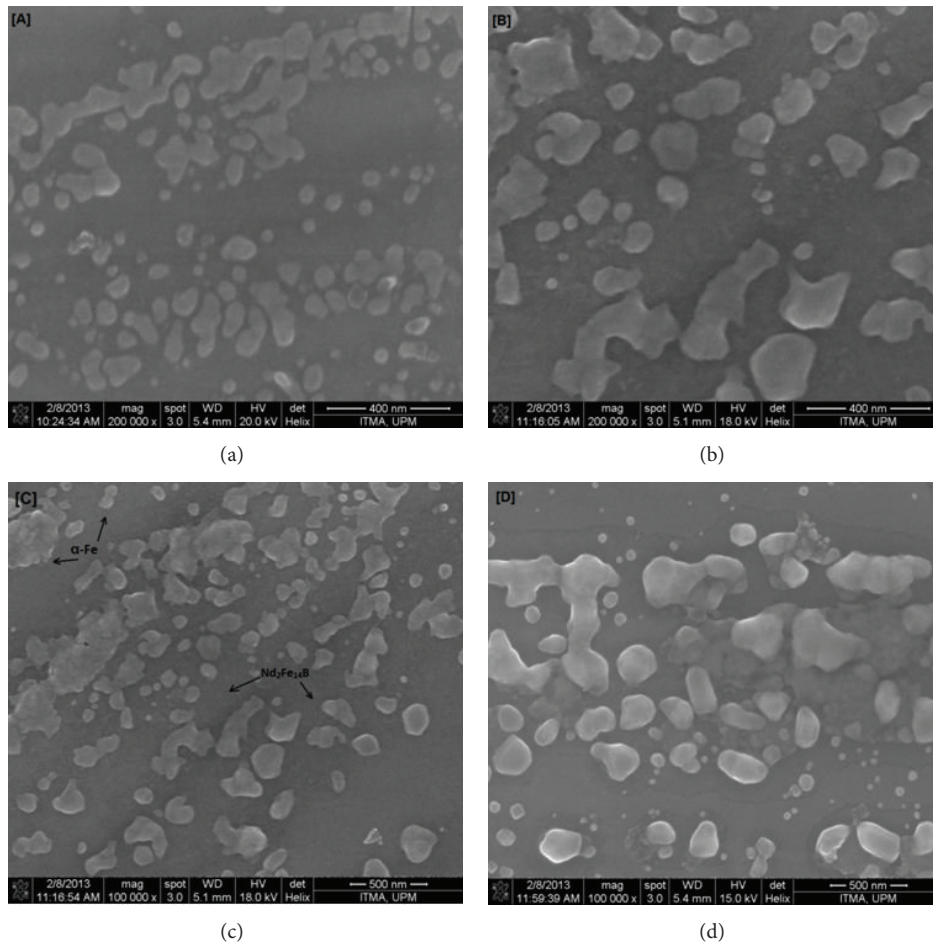


FIGURE 4: FESEM morphologies of $Nd_{9.4}Pr_{0.6}Fe_{74.5}Co_6B_6Ga_{0.5}Ti_{1.5}C_{1.5}$ at (a) 600°C, (b) 650°C, (c) 700°C, and (d) 750°C annealed ribbons for 10 minutes.

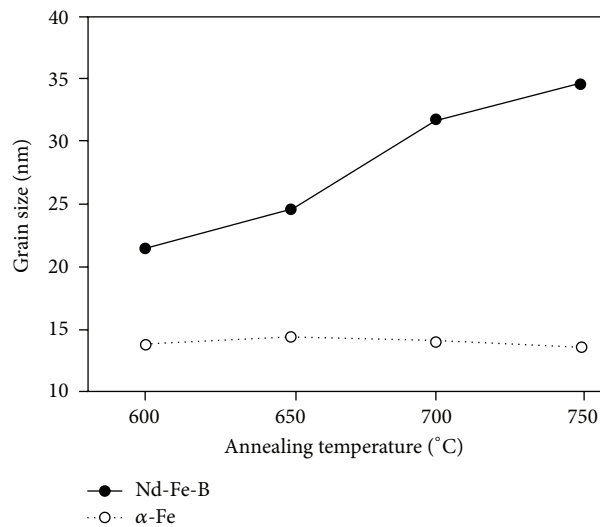


FIGURE 5: Grain sizes of $Nd_{9.4}Pr_{0.6}Fe_{74.5}Co_6B_6Ga_{0.5}Ti_{1.5}C_{1.5}$ annealed ribbon at different annealing temperature for 10 minutes.

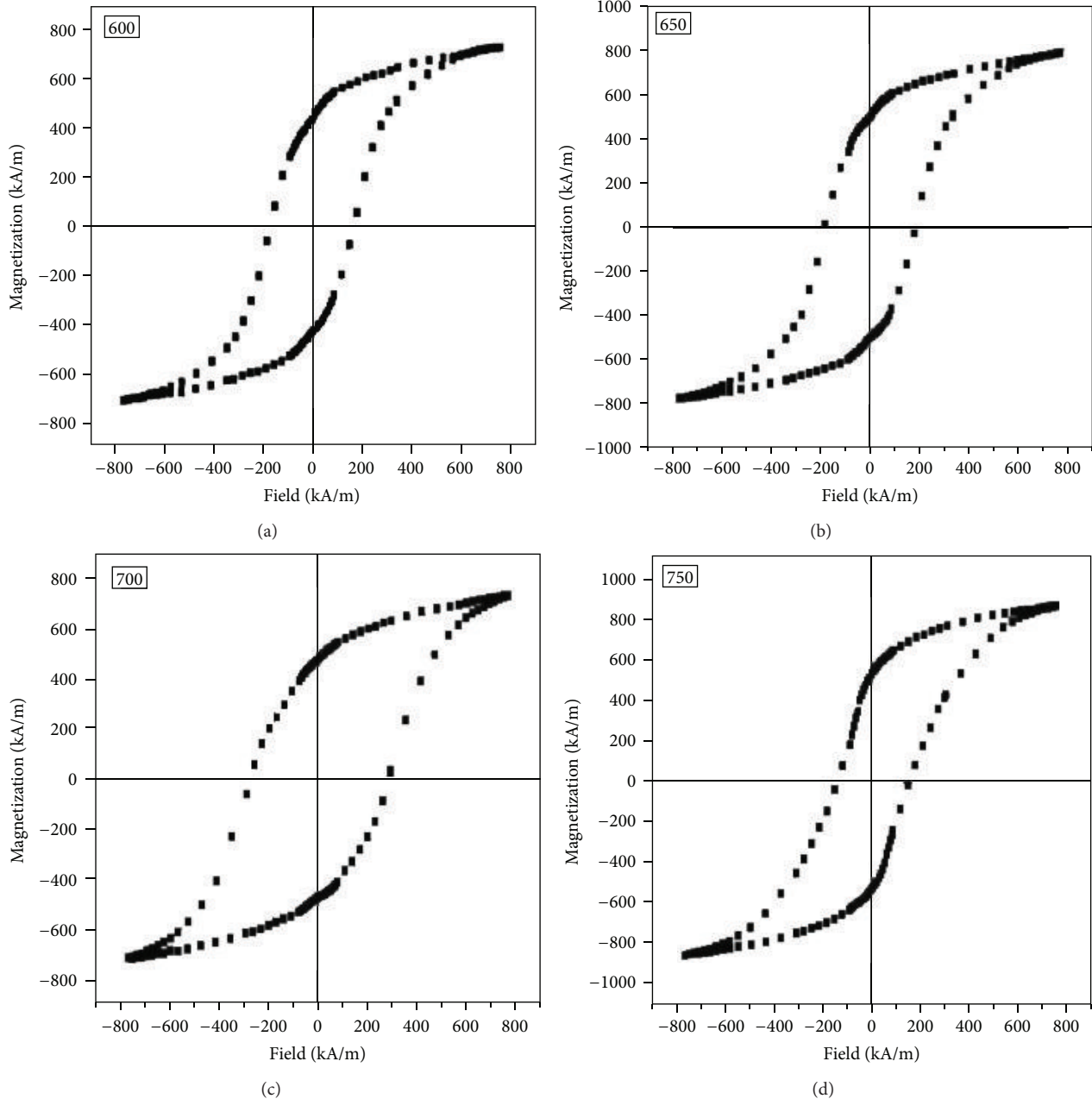


FIGURE 6: Hysteresis loops of $\text{Nd}_{9.4}\text{Pr}_{0.6}\text{Fe}_{74.5}\text{Co}_6\text{B}_6\text{Ga}_{0.5}\text{Ti}_{1.5}\text{C}_{1.5}$ annealed ribbon at different annealing temperature for 10 minutes.

to form an amorphous structure from the melt. The XRD pattern of ribbons after a thermal treatment from 600°C to 750°C is shown in Figure 3. It can be seen that the annealed samples consist of a hard magnetic $\text{Nd}_2\text{Fe}_{14}\text{B}$ phase and soft magnetic $\alpha\text{-Fe}$ phase and TiC phase have precipitated as well as the hard and soft magnetic phases. It was found that the amounts of soft and hard phases are increased with increasing temperature, suggesting that the enhancement of crystallinity was due to the heat treatment. Figure 4 shows the surface microstructure of annealed samples. As can be seen, the darker parts of the micrographs are $\text{Nd}_2\text{Fe}_{14}\text{B}$ and the lighter parts are related to $\alpha\text{-Fe}$ phase. Obviously, the micrographs

indicate that grain growth is occurring. The average grain size of a sintered body was measured over 200 grains by the linear intercept method. The results are shown in Figure 5; the $\alpha\text{-Fe}$ grains have not been changed significantly during annealing, except the slight increase and decrease, which are related to the experimental errors with size of ± 2 nanometer. Thus, heat treatment has not any effect on grain growth of the soft magnetic phase; on the other hand the Nd-Fe-B grain size increases with the increase of the heat treatment temperature. Magnetic properties of annealed ribbons were measured by alternate gradient force magnetometer (AGFM) with maximum applied field of 1.5 Tesla. The hysteresis

TABLE 1: Magnetic properties of annealed ribbon at different annealing temperature for 10 minutes.

Composition	Annealing temperature (K)	J_r/J_s	Hc (KA m ⁻¹)	(BH _{max}) (KJ/m ³)
Nd _{9.4} Pr _{0.6} Fe _{74.5} Co ₆ B ₆ Ga _{0.5} Ti _{1.5} C _{1.5}	600	0.58	202	36.70
	650	0.61	233	48.15
	700	0.64	245	60.48
	750	0.57	177	28.50

loop results are illustrated in Figure 6, the calculated data are summarized in Table 1, and Figure 5 demonstrates the dependence of magnetic properties on the temperature of annealing. As can be seen magnetic properties of the composition differ by changing the annealing temperature; for Nd_{9.4}Pr_{0.6}Fe_{74.5}Co₆B₆Ga_{0.5}Ti_{1.5}C_{1.5} annealed ribbons the best magnetic properties achieve at 700°C. Generally, the grain growth which occurs at the higher temperatures leads to deterioration in the magnetic properties [11]; hence, heat treatment at 750°C leads to inferior properties than those for 700°C annealing temperature. Furthermore, the J_r/J_s values are close to one another due to soft phase's grain size similarity [12]. The maximum energy product (BH_{max}), which is sensitive to exchange coupling and grain size, was enhanced with anneals temperature increases until 700°C due to more suitable exchange coupling at higher temperatures [13]. But after 700°C decreases because of hard phase extra grain growth, the maximum energy product (BH_{max}) of the nanocomposite magnets depends sensitively on the form of nanostructure, for example, phases present, crystallite size, and defects present [14]. However, this is not the whole story since, in comparing the ribbons with the same composition, the 700°C annealed ribbon has improved maximum energy product (BH_{max}), due to more uniform grain size distribution and higher quality crystalline Nd₂Fe₁₄B grains. The coercivity of the ribbons increased to 700°C, and then it decreased due to optimum exchange coupling at 700°C, leading the best coercivity at this temperature.

4. Conclusion

The relationship between annealing temperature, microstructure and magnetic properties of Nd_{9.4}Pr_{0.6}Fe_{74.5}Co₆B₆Ga_{0.5}Ti_{1.5}C_{1.5} nanocomposite alloys was interpreted by XRD, DSC, and FESEM analysis. It has been generally found that the crystallization behaviour of amorphous Nd_{9.4}Pr_{0.6}Fe_{74.5}Co₆B₆Ga_{0.5}Ti_{1.5}C_{1.5} alloy strongly depends on the heat treatment temperature. Additionally, it has been found that increase of annealing temperature leads to grow of Nd-Fe-B grains but does not have any effect on α -Fe grain size. It is plainly visible that magnetic properties increase significantly with heating rate up to 700°C and then will decrease. The best magnetic properties were obtained at 700°C annealing temperature.

Acknowledgment

The authors would like to thank Ms N. Shourchek for valuable assistance in this work.

References

- [1] G. C. Hadjipanayis and R. W. Siegel, Eds., *Nanophase Materials, Synthesis-Properties-Applications*, vol. 260 of NATO ASI Series, Kluwer Academic Press, Dordrecht, The Netherlands, 1993.
- [2] G. Herzer, "Amorphous and nanocrystalline soft magnets," in *Magnetic Hysteresis in Novel Magnetic Materials*, G. C. Hadjipanayis, Ed., vol. 338 of NATO ASI Series, pp. 711–730, 1996.
- [3] R. Fischer, T. Schrefl, H. Kronmüller, and J. Fidler, "Grain-size dependence of remanence and coercive field of isotropic nanocrystalline composite permanent magnets," *Journal of Magnetism and Magnetic Materials*, vol. 153, no. 1-2, pp. 35–49, 1996.
- [4] G. Bate, "Magnetic recording materials," *Journal of Magnetism and Magnetic Materials*, vol. 100, no. 1–3, pp. 413–424, 1991.
- [5] D. Lambeth, "Present status and future magnetic data storage," in *Magnetic Hysteresis in Novel Magnetic Materials*, G. C. Hadjipanayis, Ed., vol. 338 of NATO ASI Series, pp. 767–780, 1996.
- [6] G. C. Hadjipanayis, "Nanophase hard magnets," *Journal of Magnetism and Magnetic Materials*, vol. 200, no. 1–3, pp. 373–391, 1999.
- [7] Y. Q. Wu, H. Yamamoto, and K. Hono, "Microstructural investigation on the influence of V in α -Fe/Nd₂Fe₁₄B nanocomposite magnet," *Scripta Materialia*, vol. 44, no. 10, pp. 2399–2404, 2001.
- [8] M. W. Chen, A. Sakai, X. M. Wang, A. Inoue, and T. Sakurai, "Distribution of Nb and Co in an α -Fe/Nd₂Fe₁₄B-type nanocomposite," *Journal of Applied Physics*, vol. 88, no. 11, pp. 6928–6930, 2000.
- [9] E. F. Kneller and R. Hawig, "The exchange-spring magnet: a new material principle for permanent magnets," *IEEE Transactions on Magnetics*, vol. 27, no. 4, pp. 3588–3560, 1991.
- [10] T. Schrefl, J. Fidler, and H. Kronmüller, "Remanence and coercivity in isotropic nanocrystalline permanent magnets," *Physical Review B*, vol. 49, no. 9, p. 6100, 1994.
- [11] J. Jakubowicz and M. Jurczyk, "Magnetic properties of nanocomposite Nd₂(Fe,Co,M)₁₄B/ α -Fe-bonded magnets," *Journal of Alloys and Compounds*, vol. 269, no. 1-2, pp. 284–287, 1998.
- [12] R. Sabbaghizadeh and M. Hashim, "Effects of heat treatment on the magnetic properties of melt-spun Nd₆Pr₁Fe₇₆B₁₂Ti₄C₁Co₃ nanocomposite ribbons," *Electronic Materials Letters*, vol. 9, no. 1, pp. 115–118, 2013.
- [13] R. Sabbaghizadeh, M. Hashim, and S. Moraddeh, "Dependence of microstructure and magnetic properties of (Nd,Pr)-(Fe,Ti,C)-B melt-spun ribbon on quenching wheel speed," *Electronic Materials Letters*, vol. 9, no. 3, pp. 337–340, 2013.
- [14] E. Burzo, "Permanent magnets based on R-Fe-B and R-Fe-C alloys," *Reports on Progress in Physics*, vol. 61, no. 9, p. 1099, 1998.